

Coherence, Hydrodynamics and Superfluidity of a Strongly Interacting Fermi Gas

DISSERTATION

by

Leonid A. Sidorenkov

submitted to the Faculty of Mathematics, Computer
Science and Physics of the University of Innsbruck

in partial fulfillment of the requirements
for the degree of Doctor of Philosophy (PhD)

advisor:

Univ.Prof. Dr. Rudolf Grimm,
Institute of Experimental Physics, University of Innsbruck,
Institute for Quantum Optics and Quantum Information
of the Austrian Academy of Sciences

Innsbruck, June 2013

Summary

One of the challenging problems in modern physics is to understand the many-body systems composed of strongly-interacting fermions, like neutron stars, quark-gluon plasma, and high critical temperature superconductors. The main difficulties are that strong interactions require non-perturbative theoretical treatment, while the fermionic nature of particles creates the famous sign problem in numerical calculations. From experimental side, such systems have been either hardly accessible, or too complicated until recently, when the new fermionic systems were realized in ultracold atomic gases. With unprecedented possibilities to control interactions and external confinement, these newly-crafted systems became excellent models for testing and understanding strongly-interacting fermions. This work presents a number of experiments on the ultracold degenerate gas of fermionic ^6Li atoms, confined in a harmonic trap, with interparticle interactions enhanced via Feshbach resonance.

We first study the coherence properties of the many-body wavefunction. We create two Bose-Einstein condensates of weakly bound Feshbach molecules composed of two fermions, and make these condensates interfere. In case of relatively weak interparticle interactions a high-contrast interference pattern shows the de Broglie wavelength of molecules. As the interaction strength is increased, the enhanced collisions remove the particles from the condensate wavefunction and the interference pattern gradually loses contrast. For even stronger interaction the condensates do not penetrate each other and collide hydrodynamically.

We then turn our attention to study the hydrodynamics of a unitary Fermi gas, a system realized on top of the Feshbach resonance where the interactions are strongest possible. We selectively excite the higher-nodal collective oscillation modes in the trapped cloud, detect their time evolution and apply a sensitive procedure to extract the density profile, frequency and damping rate of these modes. Mode profiles and frequencies show a strong dependence on temperature, which allows to distinguish between superfluid and normal hydrodynamics and test the equation of state at finite temperature at the first time in collective-modes-type experiment. Our results are in excellent agreement with theoretical predictions based on Landau's two-fluid theory, adopted to our experimental configuration of elongated trap.

Finally, we study the phenomenon of 'second sound' in a unitary Fermi gas. By applying our previously developed two-fluid 1D-hydrodynamic model to the case of second sound excitation, we show that this special temperature wave is accompanied by a significant density perturbation, differently from the situation in superfluid helium. We then create a local temperature excitation and record its propagation along the cloud. The observed propagation pattern is fully consistent with expected second-sound behavior. We measure the speed of second sound and obtain thereby a superfluid fraction in the system - the quantity of fundamental importance for strongly-interacting superfluids.

Zusammenfassung

Eines der schwierigsten Probleme in der modernen Physik besteht im Verständnis von Vielteilchensystemen aus stark wechselwirkenden Fermionen, wie Neutronensterne, dem Quark-Gluon-Plasma und Hochtemperatursupraleiter. Starke Wechselwirkungen erfordern eine nicht-perturbative theoretische Beschreibung, während die fermionische Natur der Teilchen das sogenannte Vorzeichenproblem in numerischen Berechnungen erzeugt. Für Experimente waren solche Systeme über lange Zeit entweder unzugänglich oder zu komplex, bis vor kurzem fermionische Systeme in ultrakalten atomaren Gasen völlig neue Zugänge eröffnet haben. Mit den neuen Möglichkeiten, die Wechselwirkung zwischen den Teilchen und den externen Einschluß zu kontrollieren, sind diese neuartigen Systeme als hervorragende Modelle zur fundamentalen Untersuchung von stark wechselwirkenden Fermionen geeignet. Die vorliegende Doktorarbeit stellt eine Reihe von Experimenten an einem ultrakalten entarteten Gas von fermionischen ^6Li -Atomen vor, welches in einem harmonischen Fallenpotential eingeschlossen ist. Die interatomaren Wechselwirkungen werden über eine magnetisch induzierte Feshbach-Resonanz realisiert, wodurch das Regime von starken Wechselwirkungen zugänglich wird.

Zuerst untersuchen wir die Kohärenzeigenschaften der Vielteilchen-Wellenfunktion. Wir erzeugen zwei Bose-Einstein-Kondensate von schwach gebundenen Feshbach-Molekülen, die aus zwei Fermionen zusammengesetzt sind, und beobachten die Interferenz, wenn diese Kondensate aufeinander treffen und räumlich überlappen. Bei relativ schwachen Wechselwirkungen tritt ein kontrastreiches Interferenzmuster auf, welches die de-Broglie-Wellenlänge der Moleküle widerspiegelt. Wenn die Stärke der Wechselwirkung erhöht wird, führen Stöße zu zunehmenden Verlusten von Teilchen aus der Kondensat-Wellenfunktion und das Interferenzmuster verliert allmählich den Kontrast. Für noch stärkere Wechselwirkungen können die Kondensate nicht mehr räumlich überlappen und zeigen hydrodynamisches Kollisionsverhalten.

Wir konzentrieren uns danach auf das hydrodynamische Verhalten eines ‘unitären Fermigas’, d.h. ein Fermigas mit den stärkstmöglichen Wechselwirkungen, wie sie genau im Zentrum der Feshbach-Resonanz realisiert sind. Dafür regen wir höhere kollektive Schwingungsmoden der gefangenen Atomwolke an und beobachten ihre zeitliche Entwicklung. Mit der Hilfe eines empfindlichen Detektionsverfahrens bestimmen wir die Dichteprofile, die Eigenfrequenzen und die Dämpfungskonstanten dieser Schwingungsmoden. Die Modenprofile und Frequenzen zeigen eine starke Abhängigkeit von der Temperatur, die zwischen normaler und suprafluider Hydrodynamik unterscheidet lässt und es erstmals erlaubt, die Zustandsgleichung bei endlichen Temperaturen durch kollektive Schwingungsmoden zu testen. Unsere experimentellen Ergebnisse zeigen sehr gute Übereinstimmung mit theoretischen Voraussagen, die auf Landaus Zwei-Fluid-Theorie beruhen und für unsere experimentelle Konfigura-

tion einer stark elongierten Falle adaptiert wurden.

Schließlich untersuchen wir das Phänomen des ‘Zweiten Schalls’ in einem unitärem Fermigas. Im Rahmen des hydrodynamischen Zwei-Fluid-Modells zeigen wir, dass in unserem Fall im Unterschied zur Situation im suprafluiden Helium die Temperaturwelle des Zweiten Schalls von einer erheblichen Dichtestörung begleitet wird. Im Experiment erzeugen wir eine lokale Temperaturanregung und detektieren ihre Ausbreitung entlang der elongierten Atomwolke. Das beobachtete Muster der Ausbreitung steht in vollem Einklang mit dem für Zweiten Schall erwarteten Verhalten. Wir messen die Geschwindigkeit des Zweiten Schalls und bestimmen dadurch den suprafluiden Anteil im System als Größe, die von fundamentaler Bedeutung für stark wechselwirkende Supraflüssigkeiten ist.

Contents

Summary	iii
Zusammenfassung	iv
1 Introduction	1
1.1 Many-body physics and ultracold atoms	1
1.2 Ultracold Fermi gas with tunable interactions	2
1.2.1 Cooling and trapping	2
1.2.2 Tuning the interactions	5
1.3 BEC-BCS crossover	9
1.3.1 Phase diagram	9
1.3.2 Experimental methods	12
1.3.3 Extensions of the crossover physics	17
1.4 Outlook	18
1.4.1 Strongly interacting fermions	19
1.4.2 Open questions in BEC-BCS crossover	19
1.4.3 Second sound prospects	20
1.5 Overview	22
2 Publication: Observation of interference between two molecular Bose-Einstein condensates	25
2.1 Introduction	25
2.2 Experimental procedures	26
2.2.1 Preparation of the molecular Bose-Einstein condensate	26
2.2.2 Condensate splitting	27
2.2.3 Expansion in the magnetic field	29
2.2.4 Detection and analysis of interference fringes	30
2.3 Experimental results	31
2.3.1 Fringe period	31
2.3.2 Dependence of interference visibility on condensate fraction	32
2.3.3 Dependence of interference visibility on interaction strength	34
2.4 Conclusion and outlook	36

3	Publication: Higher-nodal collective modes in a resonantly interacting Fermi gas	39
3.1	Introduction	40
3.2	Theoretical predictions	41
3.3	Experimental procedures	42
3.3.1	Sample preparation	42
3.3.2	Thermometry	43
3.3.3	Exciting and observing higher-nodal collective modes	44
3.3.4	Analyzing the eigenmodes: Extracting mode profiles, frequencies, and damping rates	46
3.3.5	Checking for systematic errors	47
3.4	Experimental results	49
3.5	Conclusions and Outlook	52
3.6	Appendix: Temperature determination	53
3.6.1	Imperfections of absorption imaging	53
3.6.2	Wing-fitting method	54
3.6.3	Potential-energy method	55
4	Publication: Collective Modes in a Unitary Fermi Gas across the Superfluid Phase Transition	57
5	Publication: Second sound and the superfluid fraction in a resonantly interacting Fermi gas	65
5.1	Main results	66
5.2	Methods	73
5.3	Supplementary material	74
5.3.1	Excitation scheme for second sound	74
5.3.2	Determining local T/T_F^{1D}	74
5.3.3	Coupling between the density variation and the temperature variation in second sound	75
5.3.4	Measurement uncertainties	77
5.3.5	Available theoretical models for the superfluid fraction n_s/n	80
	Acknowledgments	95

Chapter 1

Introduction

1.1 Many-body physics and ultracold atoms

In the beginning of 20th century, after liquification of He and discovery of superconductivity in metals by H. Kamerlingh Onnes, a new exciting chapter of many-body physics has been opened. Since that time and for many decades the studies of superconductivity and superfluidity were performed on the available solid state systems [DG66] on one hand, and on the only known quantum liquids: liquid helium II (^4He below 2.17K), and liquid ^3He [Kha65] on the other hand. However, despite a huge fundamental interest in both superconductivity and superfluidity, the superconductors were superior from the point of view of possible applications. The ability to create extraordinarily-high magnetic fields, and the interest in questions like ‘superconductivity at room temperature’ have triggered a rapid technological progress in materials fabrication and search of new superconducting materials different from metals and alloys. Such materials have been found [Bed88] among the room-temperature insulators(!) and they are widely known as high critical temperature superconductors (HTS), with a critical temperatures of about 130 Kelvin.

At the same time, this technological breakthrough created one of the biggest puzzles for many-body physicists. Theoretical models, which have successfully described superconductivity in metals [DG66, Tin75], could hardly give reasonable results for HTSs! All the first attempts were to modify BCS theory for metallic superconductors in rather phenomenological manner, until it was realized that the HTSs are much more complicated: the interactions between the electrons are not weak anymore, and the many-body system is essentially strongly correlated. A full theoretical description of this solid-state system involves a non-trivial Hubbard-like Hamiltonian (effectively in two dimensions). Different approximations and subsequent numerical solutions were employed to solve the problem, but none of them was able to capture all the necessary physics. Nowadays, as to our knowledge, there are at least 15 theories attempted to explain the physics of HTSs, but still no microscopic model analogous to BCS-scenario for conventional superconductors, is available [Leg06, Car02].

To understand this challenging problem, and many other related problems is, generally speaking, one of the motivations of the work presented in this thesis. Moreover, also the systems with completely different characteristic energy scales, like neutron stars and quark-gluon plasma are sharing similar superfluidity-related physics with HTSs, being all composed

of strongly interacting fermions. If one has a simple system in the lab, which captures a major part of the necessary physical attributes of HTSs, one is able to address the related questions experimentally. In this sense the experiments with solid state systems depend a lot on progress in materials fabrication, which is a significant restriction on research. In the field of ultracold atoms, we use a different approach to create a strongly interacting fermionic system which is essentially free of these limitations.

Rapid progress from the first revolutionary ideas of laser cooling [Let77, CT98, Phi98, Chu98] to establishing the well-understood methods of ‘preparing’ a degenerate atomic samples has opened fantastic opportunities for exploring many-body physics with ultracold atoms. The power and great potential of a new field were soon demonstrated by creation of the Bose-Einstein condensate (BEC) and deeply degenerate atomic Fermi gas. After the first very important proof-of-principle experiments, universality of the cooling mechanisms and further development of lasers allowed to bring more and more new species into the ultracold regime. The cooling methods were considered then more as a tool and the question of ‘how to cool it?’ became less important than ‘why to cool it?’ This moment has completed, in our opinion, a paradigmatic evolution of approach to study many-body systems. Instead of trying to find a new interesting system in nature, or using chemistry to modify an already existent system (like in solid state), one aims at ‘constructing’ the specific new system from ‘building blocks’ of a proper type in order to address some particular class of physical problems. In the following section we will introduce one of such a many-body systems, which has been created in the ultracold world and turned an excellent playground to explore the rich physics of a strongly interacting Fermi matter.

1.2 Ultracold Fermi gas with tunable interactions

In this section we introduce an ultracold gas of fermionic ${}^6\text{Li}$ atoms in a balanced mixture of two Zeeman states, cooled to the temperatures about $0.1T_F$ ¹, which corresponds to a degenerate regime where fermionic statistics of the atoms plays a crucial role. We also discuss here the main idea of tunability of the interparticle interactions and the cornerstone concept of Feshbach resonance in this context.

1.2.1 Cooling and trapping

Different fermionic species have been already brought to degeneracy in the field of ultracold atoms. As to our knowledge, they include ${}^{40}\text{K}$ [DeM99, Roa02], ${}^6\text{Li}$ [Tru01, Sch01, Had02, Gra02, Sil05], ${}^3\text{He}^*$ [McN06], ${}^{173}\text{Yb}$ [Fuk07a], ${}^{171}\text{Yb}$ [Fuk07b], ${}^{87}\text{Sr}$ [DeS10, Tey10], ${}^{161}\text{Dy}$ [Lu12]. In our experiment we prepare a degenerate cloud of ${}^6\text{Li}$ atoms [Joc03b, Joc04] in all-optical way, based on the standard cooling techniques [Met99]. We start by loading the magneto-optical trap (MOT) from the Zeeman-slowed atomic beam. After cooling in

¹Fermi temperature T_F is a characteristic temperature scale of an ideal Fermi gas, defined by Fermi energy $E_F = k_B T_F = (3\pi^2)^{2/3} \frac{\hbar^2}{2m} n^{2/3}$. Fermi energy is the value of chemical potential of an ideal Fermi gas at zero temperature [Lan80a]. Fermi wavevector k_F is defined by $\frac{\hbar^2 k_F^2}{2m} = E_F$. Note that $k_F \propto n^{1/3}$, which gives a characteristic interparticle distance.

the MOT we reach the temperatures of about $160\mu\text{K}$, which is slightly above the Doppler cooling limit for D_2 line of ${}^6\text{Li}$. We then compress the MOT and transfer the atoms into a resonator-enhanced optical dipole trap ('reservoir trap') [Mos01, Gri00]. The phase-space volume of this trap is well-matched the phase-space volume of the compressed MOT, thereby allowing to reach the transfer efficiencies as high as 20%. During the transfer we switch off the cooling light slightly after repumping light (Fig. 1.1a), which leads to optical pumping into the lower hyperfine state. After the transfer we switch on an additional tightly-focused dipole trap, that overlaps with the center of reservoir trap. In order to have a sufficient collision rate for a further evaporative cooling, we tune the interparticle interactions to a desired value by means of Feshbach resonance [Chi10]. We adiabatically ramp the bias magnetic field from zero to a chosen finite value around the broad s-wave Feshbach resonance at 832 Gauss [O'H02a, Bar05b, Zür13]². During this ramp, the Zeeman-degenerate $F=1/2$ state splits into two lower Zeeman states (denoted for convenience $|1\rangle$ and $|2\rangle$), and sometimes referred to as 'spin up' and 'spin down') in Paschen-Back regime, which have equal population (Fig. 1.1b). The presence of two spin states allows for s-wave scattering, which is forbidden by the wavefunction symmetry in case of spin-polarized sample. This circumstance has an important consequence for evaporation procedure. Since at low temperatures scattering with all the higher partial waves is strongly suppressed by the centrifugal barrier [Lan77] and only the s-wave scattering survives, the spin-polarized Fermi gas is almost non-interacting (ideal) and needs an additional 'coolant' specie to be cooled down sympathetically [Tru01, Roa02]. The evaporation procedure for us is then straightforward: we consequently lower the depth of reservoir trap to zero, and the depth of the tightly-focused dipole trap to some finite value where we reach a sufficient quantum degeneracy. After the necessary temperature is reached, we slightly increase the depth of the tight dipole trap ('recompress' the trap) and keep it at some constant level. This last step is essential to prevent a plain evaporation in the trap during the measurement sequence. Our experience shows that already for the trap depth of five times the chemical potential of the gas the plain evaporation is negligibly small. After this preparation procedure we normally have a 50/50 mixture of atoms in two spin states, with about 150,000 atoms per spin state. The resulting trap is well approximated by a harmonic trap configuration with the typical trapping frequencies $\omega_z = 2\pi \times 22\text{ Hz}$ and $\omega_x = \omega_y \equiv \omega_r = 2\pi \times (500 - 900)\text{ Hz}$. The difference in trapping frequencies is due to the fact that weak axial confinement is formed by a slight inhomogeneity of the bias magnetic field and the tight radial confinement is given by the optical dipole force. Therefore we have an atomic sample, which is highly elongated in axial (z) direction (cigar-shaped cloud in Fig. 1.1c). The temperature of the trapped atomic cloud is typically $0.1T_F^{\text{trap}}$ ³.

²The position of this resonance was earlier measured [Bar05b] to be at 834.1(1.5) Gauss. The recent measurement [Zür13] with a better precision and an accurate account for confinement-induced shifts, gives a result of 832.18(8) Gauss. This small difference, however, does not affect much the results of the previous experiments which have relied on the old value. In the next chapters we will still use the old calibration, while in the present chapter we already rely on the new calibration.

³As the density of the trapped sample is inhomogeneous, the local value of T_F is changing throughout the trap. The local normalized temperature of the cloud T/T_F in this case takes the values from about 0.05 in the trap center to infinity at the border, where density vanishes. In order to conveniently characterize a trapped Fermi gas, one introduces a trap-related Fermi temperature as $k_B T_F^{\text{trap}} = \hbar(3N \omega_r^2 \omega_z)^{1/3}$, where N is the total atom number in the trap.

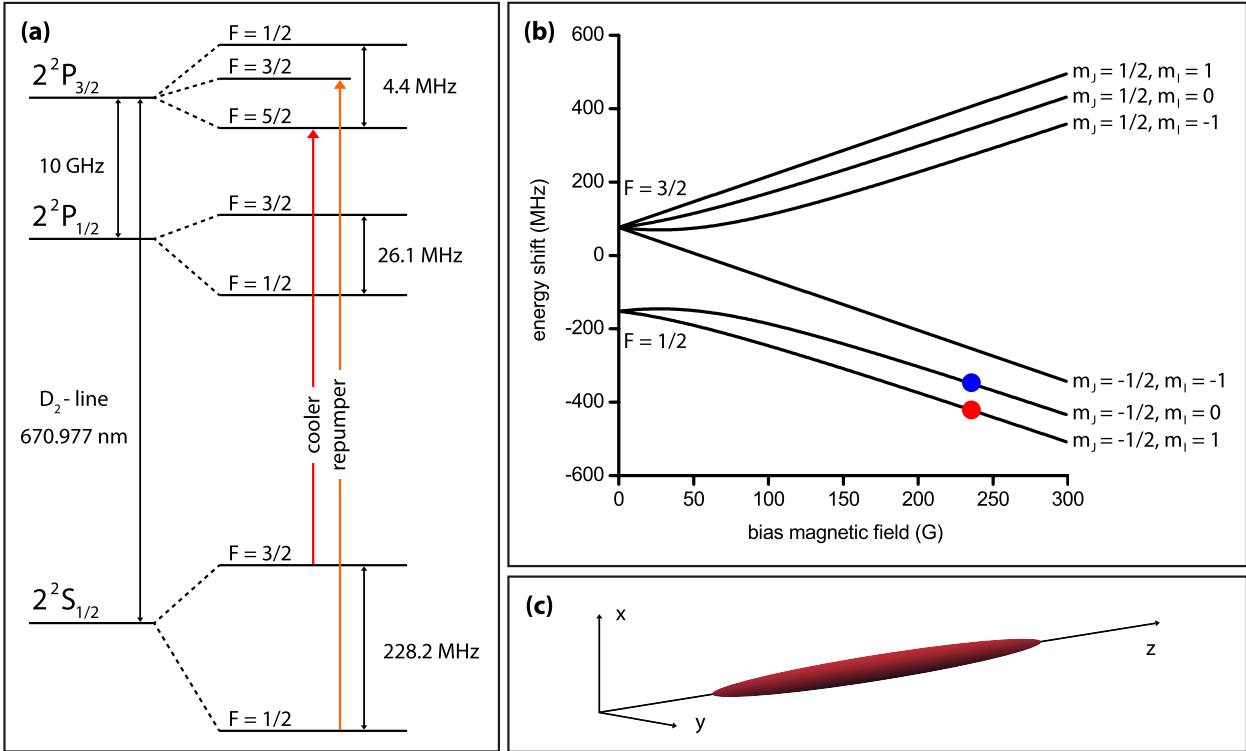


Figure 1.1: Cooling and trapping of the ${}^6\text{Li}$ atom. (a) The energy level scheme of ${}^6\text{Li}$ atom. The transitions used for laser cooling are indicated. (b) Zeemann splitting in the ground state. Full circles represent the equally populated states $|1\rangle$ (lowest) and $|2\rangle$ (first lowest). (c) Typical shape of the trapped cloud, with axes notation.

At the end of preparation procedure before starting the measurement sequence it is normally convenient to have a sample in a thermodynamic equilibrium state, well isolated from environment ⁴. In our case the environment is vacuum which prevents any heat exchange or work being performed on the system and preserves its internal energy. However, as the system is finite, the boundary conditions and hence the volume are defined by the trapping potential, which must be ideally constant over time unless we change it in a controlled way. In reality the stability of trapping potential is restricted by the power and position fluctuations of the trapping laser beam (for optical confinement), or by the fluctuations of magnetic field (for magnetic confinement). In our hybrid trap the most contribution seems to come from the optical dipole trap stability. The fluctuations of power and position of the laser beam increase the internal energy of the sample [Sav97, Geh98, Gar00] via parametric excitation [Lan93], which eventually results in the heating. The evaluation of heating rate in this process is a nontrivial problem, as it requires the knowledge of specific heat for a

⁴In the case when the system is purposely driven into a particular non-equilibrium state, as, for example, by rapidly changing the internal states of the initially non-interacting atoms such that the final states become strongly interacting ('quenched' system), our discussion concerns only initial state. We also do not discuss here a very special case of the engineered dissipation, where the controlled interaction with a thermal bath is actually a part of preparation procedure [Bar13].

particular trapping configuration [Bul05]. The typical measured heating rates in our experiment are of about 0.01-0.02 T_F^{trap} per second at the temperatures of $0.1T_F^{\text{trap}}$, which gives on the timescales of the actual measurements (about 50-200 ms) the increase of the temperature only by a few percent. We can be therefore confident that the temperature and other thermodynamic quantities which we measure at some time moment during the experiment, are well defined for the whole experimental sequence and the state of the system is a very good approximation to global equilibrium one.

1.2.2 Tuning the interactions

In view of particular importance of interatomic interactions in our system, we briefly summarize here the main results of scattering theory in the limit of low energies. For the problem of two particles interacting via some attractive potential $U(\vec{r}_1 - \vec{r}_2)$, the motion of center of mass and relative motion can be separated. As a consequence, the problem of two interacting particles reduces to a scattering of a single particle having reduced mass μ and energy $E = \frac{\hbar^2 \vec{k}^2}{2\mu}$ in a central-symmetric potential $U(r)$ ⁵. After the separation of angular and radial variables one arrives at the textbook equation for the radial part of wavefunction [Lan77]:

$$\frac{1}{r^2} \frac{d}{dr} \left(r^2 \frac{dR_{kl}}{dr} \right) + \left(k^2 - \frac{l(l+1)}{r^2} - \frac{2\mu}{\hbar^2} U(r) \right) R_{kl} = 0, \quad (1.1)$$

or alternatively for the function $\chi_{kl} = rR_{kl}$:

$$\frac{d^2}{dr^2} \chi_{kl} + \left(k^2 - \frac{l(l+1)}{r^2} - \frac{2\mu}{\hbar^2} U(r) \right) \chi_{kl} = 0. \quad (1.2)$$

By comparing the well-known asymptotic solution for R_{kl} at large distances with the expansion in l -series of the simple ansatz $\psi_k \approx e^{ikz} + f(\theta) \frac{e^{ikr}}{r}$ for the scattering wavefunction one finds the quantum-mechanical expressions for scattering amplitude $f(\theta)$:

$$f(\theta) = \sum_{l=0}^{\infty} (2l+1) f_l P_l(\cos \theta), \quad (1.3)$$

where $P_l(\cos \theta)$ are Legendre polynomials, and f_l are partial scattering amplitudes given by

$$f_l = \frac{1}{k \cot \delta_l - ik}, \quad (1.4)$$

with the scattering phases δ_l containing the information about the actual scattering potential. The total scattering crosssection is then obtained as

$$\sigma = 2\pi \int_0^\pi |f(\theta)|^2 \sin \theta \, d\theta = \frac{4\pi}{k^2} \sum_{l=0}^{\infty} (2l+1) \sin^2 \delta_l. \quad (1.5)$$

⁵We assume here the interaction potential to be isotropic, i.e., without angular dependence, which means $U(\vec{r}_1 - \vec{r}_2) = U(\vec{r}) = U(r)$. This is well satisfied for alkali and earth-alkali atoms. The relative wavevector \vec{k} is defined as $\vec{k} = \frac{\vec{p}_1 - \vec{p}_2}{\hbar}$.

Therefore, in order to calculate the full crosssection for some arbitrary value of the energy k^2 one needs to know all the partial-wave contributions. The situation is however dramatically simplified for the scattering in the limit of very low energies⁶. Here, the scattering phases δ_l depend on the energy as $\propto k^{2l}$ [Lan77]. All the contributions from partial waves with $l \geq 1$ become negligibly small, and in the limit of $k \rightarrow 0$ the scattering is completely defined by a single parameter - the s-wave ($l = 0$) scattering length a :

$$\lim_{k \rightarrow 0} f_0 = -a \quad (1.6)$$

The s-wave scattering phase is then expressed as $\delta_0 = -ka$. We note that to properly account for the energy dependence of scattering one has to calculate the correction to the scattering phase by Taylor expansion of $k \cot \delta_0$ in Eq. 1.4 as $k \cot \delta_0 = -\frac{1}{a} + \frac{1}{2}k^2 r_e + \dots \equiv -\frac{1}{a(k)}$, where r_e is so-called effective range of the potential (see, for instance, [Köh06]). For the purposes of further explanation, we can safely neglect this small correction.

To understand the main properties of the s-wave scattering length a and the origin of scattering resonances it is enough to consider a spherical square well model potential (Fig. 1.2a) [Gio08, Wal08]. In such a system the resonance in scattering as a function of potential depth is expected to occur whenever the potential is able to support one more bound state. From the mathematical point of view, one solves the equation for the radial wavefunction $\chi(r)$ (Eq. 1.2) in the full range $0 < r < \infty$ for $E = \frac{\hbar^2 k^2}{2\mu} > 0$ continuum scattering states and takes the limit of $k \rightarrow +0$. Analogously, one finds a bound-state solution with $E = -\frac{\hbar^2 \kappa^2}{2\mu} < 0$ and takes the limit of $\kappa \rightarrow -0$. Then, these solutions have to be connected at the point $E = 0$. By doing so, one obtains the scattering resonances in the form of Eq. 1.7 and the universal⁷ bound state energy (Eq. 1.8).

$$a = r_0 \left(1 - \frac{\tan(\kappa_0 r_0)}{\kappa_0 r_0} \right), \quad (1.7)$$

where κ_0 is defined via depth of the well $U_0 = \frac{\hbar^2 \kappa_0^2}{2\mu}$,

$$E_b = \frac{\hbar^2}{2\mu a^2}. \quad (1.8)$$

From the physical point of view, the scattering resonance occurs exactly when the energy of the bound state coincides with the scattering energy of the ‘free particle’. For a real atomic system, it is not easy to fine-tune the depth of the interaction potential (especially *in situ*) in order to bring its bound state very close to threshold. However, if we consider the

⁶The ‘low energies’ in this case are defined by condition $kr_0 \ll 1$. In other words, the de Broglie wavelength λ_{dB} of the particle becomes much larger than the range of potential. This is normally the case in ultracold gases if the particles interact via short-range Van der Waals potentials $U(r) = -\frac{C_6}{r^6}$. For Li atoms, $r_0 \cong r_{VDW} \approx 30a_0$ and $\lambda_{dB} \approx 1.35 \cdot 10^4 a_0$ at $1\mu\text{K}$, where a_0 is Bohr radius. The limit of $k \rightarrow 0$ is frequently a good approximation to describe low-energy scattering physics.

⁷The radial wavefunction of these near-threshold ‘halo dimer’ bound state is well approximated as $R(r) \cong \frac{1}{\sqrt{2\pi a}} \frac{e^{-r/a}}{r}$. The average separation between the atoms is then $a/2$ [Köh06], which means that practically all the wavefunction is outside the range of potential. The fine details of potential are thus irrelevant for the scattering, or, in other words, the scattering is *universal*. This holds as long as $a \gg r_0$.

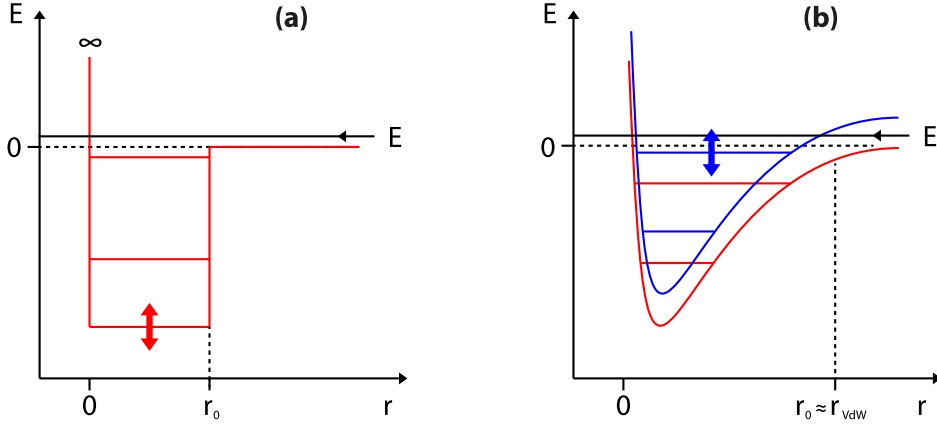


Figure 1.2: Scattering resonance. (a) Scattering resonance in the radial square well model potential. When the potential depth is tuned, the bound state energies E_b shift and can reach zero energy threshold. The scattering energy of free atoms $E = \frac{\hbar^2 k^2}{2\mu}$ is just above threshold. The scattering resonance occurs in the limit of $E, E_b \rightarrow 0$ (see text). (b) Scattering resonance in Fano-Feshbach scenario. Atoms are prepared in the open (red) channel, which defines the background scattering length a_{bg} just as it would be for the ‘square well’ case when the bound state is far from threshold. The scattering resonance occurs when the energy of the bound state in the closed channel (blue) is tuned to coincide with the energy of the free atoms in the open channel (red).

atoms having in addition to motional some internal degree of freedom (for instance, spin) the bound state can, in principle, belong to a different internal state. In the case when this second state has some finite coupling to the original state (in which the scattering atoms are prepared), and these states can be tuned with respect to each other, the scattering resonance can be easily realized. This is exactly the idea behind the concept of Feshbach resonance⁸ (Fig. 1.2b). In terms of a coupled-channel model of Feshbach resonance [Chi10] the second state is normally called a ‘closed channel’ and the initial state is called an ‘open channel’. The external bias magnetic field plays a role of tuning parameter as the channels have different magnetic moments. The s-wave scattering length as a function of magnetic field B then takes a form of $a(B) = a_{bg} \left(1 - \frac{\Delta_B}{B - B_0}\right)$, where a_{bg} is a background scattering length defined only by the properties of potential in the open channel; Δ_B and B_0 are respectively the width and position of the resonance. In Fig. 1.3 we present one of the most ‘famous’ Feshbach resonances in ultracold atoms, which occurs in a mixture of states $|1\rangle$ and $|2\rangle$ of ${}^6\text{Li}$. This is the Feshbach resonance which we use in our experiment for tuning the interactions. It has the width $\Delta_B \cong 300\text{G}$ which makes the tuning precise (da/dB is very small as compared to many other resonances) and robust in terms of possible magnetic field fluctuations.

Now we discuss the physical meaning of what happens when the scattering length a is tuned by means of Feshbach resonance. The effective mean-field interaction energy is

⁸Feshbach resonance is sometimes also referred to as Fano-Feshbach resonance, see original papers by corresponding authors [Fan61, Fes58, Fes62]. The first observations of Feshbach resonances in ultracold atoms were reported in Refs. [Ino98, Cou98]. A broader historic overview can be found in in [Chi10].

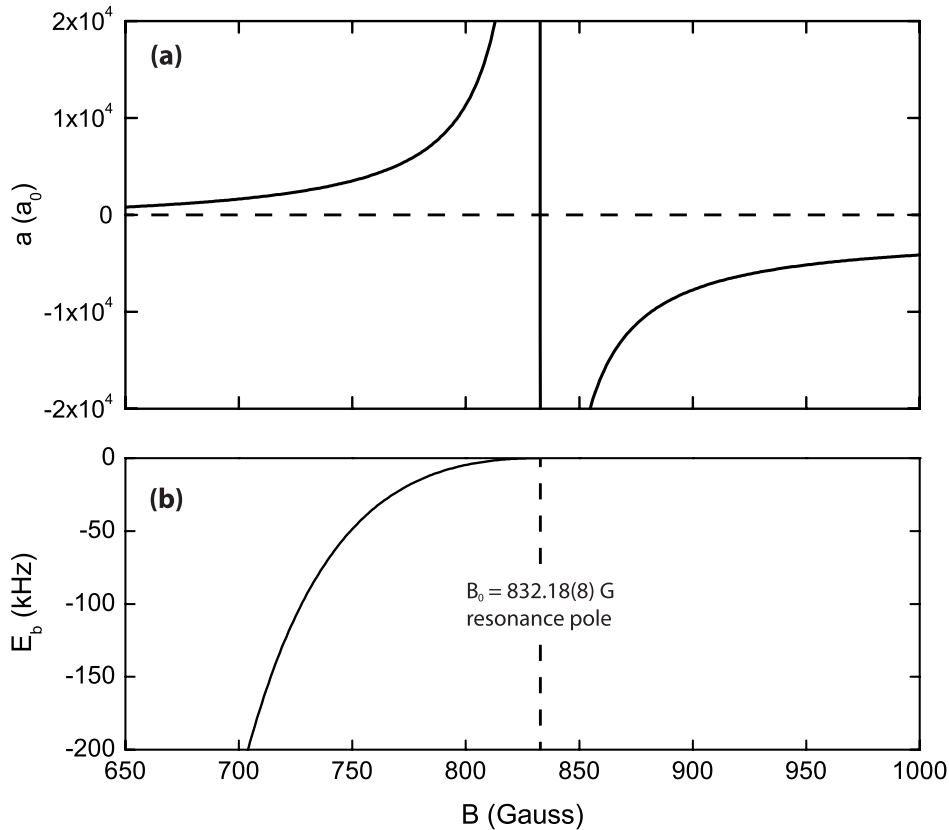


Figure 1.3: Feshbach resonance at 832 Gauss in $|1\rangle - |2\rangle$ mixture of ${}^6\text{Li}$ atoms. (a) The s-wave scattering length a as a function of bias magnetic field (data taken from [Zür13]). (b) The energy of the universal bound state, showing expected parabolic behavior around the pole of the resonance and connects adiabatically to the bound state of the closed channel only at the magnetic field value around 540 Gauss (not shown).

conveniently parametrized as a function of scattering length as $E_{int} = \frac{4\pi\hbar^2 a}{m} n$, where m is the mass of the atom and n is the atomic density (see, for instance, [Wal08]). Therefore the sign of a defines whether the interaction is repulsive or attractive⁹. When the scattering length a is further increased towards $\pm\infty$ we enter the strongly interacting regime¹⁰, where the mean field approach breaks down and the correct treatment of interactions becomes a challenging theoretical problem. But surprisingly enough when the scattering length is tuned further to be exactly at the resonance pole ($a = \pm\infty$), the situation is again simplified. In this limiting case a diverges¹¹ and is not anymore a relevant lengthscale in the problem, while all the physics is to be determined by the remaining λ_{dB} and $n^{1/3}$ lengthscales, respectively

⁹This was clearly demonstrated in early experiments on Bose-Einstein condensates. The condensate was stable on the ‘repulsive side’ of the Feshbach resonance, while the collapse was observed on the ‘attractive side’ when the number of atoms exceeded the critical value [Don01].

¹⁰This is formally defined as $|a| n^{1/3} \geq 1$, i.e., the scattering length is larger than the interparticle spacing.

¹¹This limit is known as ‘unitary limit’ in quantum mechanics. Despite the divergence in the scattering length, the crosssection is still finite and limited by the energy of colliding particles $\sigma = \frac{4\pi}{k^2}$. All the thermodynamic quantities also change smoothly as the interactions are tuned across the limit.

associated with temperature and density. This lengthscales argument, lies in the heart of so-called ‘universal hypothesis’ [Ho04]. From the thermodynamical point of view, even though the interactions are strongest allowed by quantum mechanics, they do not enter explicitly into any thermodynamic quantity and eventually just lead to ‘rescaling’ of the corresponding ideal gas quantities. The physics in this regime is independent on the details of interaction potential (as discussed above) and hence on the type of the interacting particles. Unitary gas can be in principle realized for both bosons and fermions. However, the unitary Bose gas is unstable against molecule-molecule and molecule-atom collisions [Xu03, Web03, Rem12]. In the fermionic mixture of two spin state, the three-body decay is strongly suppressed by Pauli principle (see [Pet04] and references therein). This makes our system well suitable for studying the many-body physics in the strongly interacting regime and, in particular, in the unitary limit.

1.3 BEC-BCS crossover

In this section we discuss the rich physics of the so-called ‘BEC-BCS crossover’ which takes place in the Fermi gas as the interparticle interactions are tuned across the Feshbach resonance. The purpose here is not to give a detailed review of strongly interacting Fermi gases, but rather to provide a necessary minimum to understand the physics of the system and our motivation for experiments presented in the following chapters. After introducing the phase diagram, we overview the experimental methods used so far to study the properties of the Fermi gas in BEC-BCS crossover and the main achievements these methods have lead to. In this general context, we consider the advantages and limitations of the methods used in our experiment. Finally, we discuss a number of ‘extensions’ to this model BEC-BCS crossover system, which allow to address new physics.

1.3.1 Phase diagram

Here we introduce step by step the phase diagram (Fig. 1.4) of the system described in the previous section, namely a degenerate Fermi gas in a balanced mixture of two spin states with resonantly enhanced interactions, confined in a harmonic trap. Phases are shown as a function of reduced temperature T/T_F^{trap} and interaction strength which is conveniently parametrized by dimensionless interaction parameter $1/k_F a$. The Fermi wavevector k_F is related here to the temperature T_F^{trap} , and the region of $-1 < 1/k_F a < 1$ represents therefore an effectively strongly interacting regime for the trapped Fermi gas. Two well-understood limits on the interaction axis are $1/k_F a \rightarrow \pm\infty$. They correspond to the small repulsive and small attractive effective mean-field interaction. On the positive side of Feshbach resonance the molecular bound state exists. Therefore, a pair of fermions with opposite spins can form a molecule and, if the temperature is low enough, these composite molecules condense. This is the BEC-limit (left side on the phase diagram). On the opposite side of the Feshbach resonance, there is no bound state and the pairing is essentially many-body effect occurring via BCS-scenario, analogously to the pairing between electrons in metallic superconductor. This is a BCS-limit (right side on the phase diagram). The easiest way to connect these two

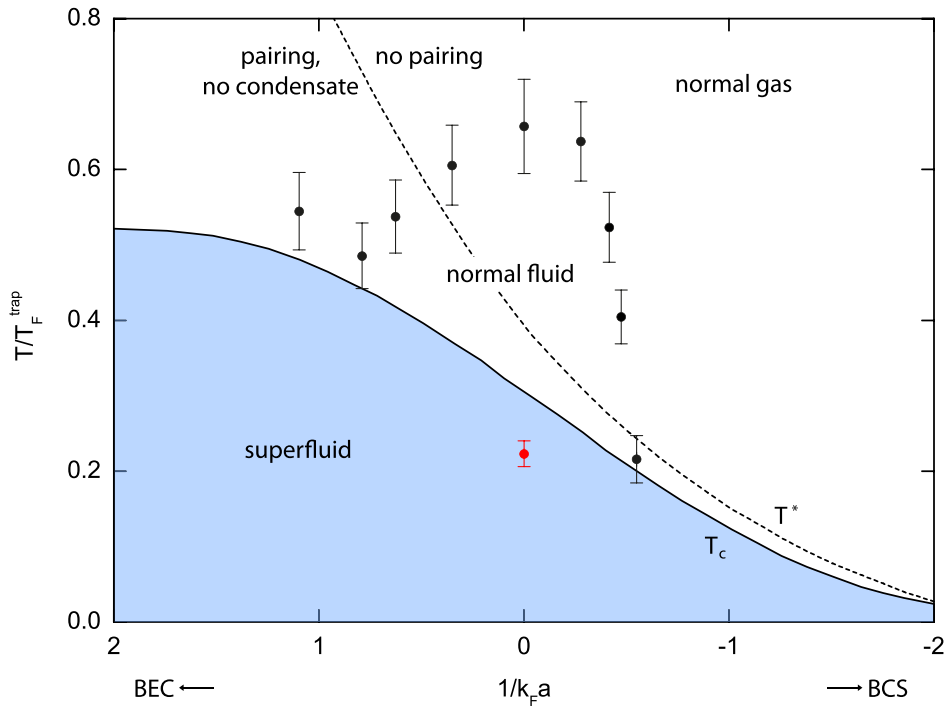


Figure 1.4: Phase diagram of the BEC-BCS crossover. The solid black and dashed black lines respectively represent the calculated critical temperature for superfluidity (T_c) and the pair-breaking temperature (T^*) for an experimentally relevant case of harmonic trapping, as reproduced from the Ref. [Per04]. The red solid data point is the measured critical temperature at unitarity [Ku12]. The black solid data points indicate the smooth transition from a collisionally hydrodynamic regime (normal fluid) into a collisionless one (normal gas), as measured in [Wri07] (see text).

limits would be at zero temperature [Leg80], where the many-body system is always in the ground state, namely a superfluid. Superfluidity at zero temperature is not surprising as the required bosonic statistics of the particles is well fulfilled by molecules on the BEC side and by Cooper pairs¹² on the BCS side. The ‘internal structure’ of the many-body wavefunction is however very different. As we tune the interaction across the resonance, the system still remains in the ground state, but the wavefunction adjusts itself accordingly and smoothly evolves from one limit to another manifesting thereby a *crossover* from BEC to BCS type of superfluid¹³. The pairing exists therefore in the whole crossover region, but its nature does not permit anymore a simple interpretation: it includes both features of the molecular pairing (in space) and Cooper pairing (in momentum space) in some complicated manner.

¹²The statistics of Cooper pairs is nearly bosonic [DG66].

¹³In the early literature the BEC and BCS limits are sometimes respectively called the limit of ‘strong’ and ‘weak’ coupling, which might be somehow confusing. The word ‘coupling’, in our understanding, refers here to the binding energy of the pair or, equivalently, to the size of the pair. In the BCS limit, the binding energy is exponentially small compared to Fermi energy and the size of the Cooper pair exceeds greatly the mean interparticle distance, while in the BEC limit the binding energy is given by the energy of molecular state and the size of the molecule is smaller than the interparticle distance.

If we consider now to increase the temperature, more and more excitations above the ground state are created and at some point the system undergoes a second order phase transition into a normal state. As we can see, this happens already at very low temperatures on the BCS side. For this matter the knowledge on the critical temperature for superfluidity (T_c line in Fig. 1.4) is essential to understand the crossover regime at finite temperatures¹⁴. The crossover theory is now rigorously generalized and includes the region of finite temperatures [Noz85, Per04]. A question of pairing could be also addressed in the finite-temperature region. In Fig. 1.4 we show the ‘critical temperature’ for pairing (T^* line) which is always above the critical temperature for superfluidity T_c . The region between two curves, where there are already preformed pairs but no superfluidity, is still not well understood. This region is called ‘pseudogap regime’ [Che05, Tsu10] in analogy to the corresponding region in HTSs.

Now, as the two limits are connected in the whole diagram, we note that the most of crossover evolution happens in the region of strong interactions [Noz85] and ‘zoom’ into this region. Considerable efforts have been already made to understand the strongly interacting Fermi system [Ing08, Gio08], still the theoretical description remains a challenging problem due to its non-perturbative nature. Here we discuss a few important consequences imposed by the strong interactions, which will be the focus of the research presented in the next chapters.

In the strongly interacting regime the phenomenon of superfluidity has to be clearly distinguished from the pair condensation (see, for example, [Fuk07c]) even at the lowest temperatures (zero temperature in theory). In a very weakly interacting BEC, the density of the condensate (occupation of the $k = 0$ state) is almost equal to the superfluid density [Pit03], while for a strongly interacting BEC the condensate density is expected to be depleted [Lan80b]. This was also demonstrated in the experiments on superfluid helium, where the condensate fraction was determined precisely [Gly00]. In Chapter 2, we realize a truly strongly interacting molecular BEC and experimentally address the question of condensation.

Strength of the interactions also affects the collective response properties of the system, namely whether its dynamic behavior is more like the one of a fluid (hydrodynamic) or of a gas (collisionless). While the superfluid is always hydrodynamic, the transition region in normal state is indicated by the black filled data points in Fig. 1.4. The criterion is however quantitative: one compares the collision rate ν and the characteristic motional timescale, which is given by trapping frequency ω . If $\nu \gg \omega$, then the local equilibrium is easily established, which is a characteristic of liquid. If the opposite limit $\nu \ll \omega$ holds, then the atoms practically ‘don’t see’ each other and the system is similar to an ideal gas. With these definition the transition boundary is rather smooth in reality and depends on the value of trapping frequencies¹⁵. In Fig. 1.4 we define the hydrodynamic region with respect to the fast radial degree of freedom (see Fig. 1.1c), with a typical trap frequency $\omega_r \approx 1$ kHz. In

¹⁴The dependence of the critical temperature T_c on interaction is *qualitatively* different for a case of homogeneous system [Per04].

¹⁵Using a very elongated trap with an aspect ratio $\omega_r/\omega_z \cong 100$ it is possible to reach a hydrodynamic behavior along the z-axis, while being collisionless in radial direction. This might be of considerable advantage, when the attainable interaction strength is restricted [Mep09a].

Chapters 3 and 4, we approach the superfluid-to-normal hydrodynamic transition, which was practically indistinguishable before in related experiments, with a new sensitive method.

The unitary limit of interactions ($1/k_F a = 0$ in Fig. 1.4) needs a special treatment. As we have mentioned earlier, the universality hypothesis significantly simplifies the description of the system [Hau07, Hau08, Hu07] which leads to the maximum ‘overlap’ between the theory and experiment in strongly interacting regime to be reached at unitarity. One of the recent achievement was to precisely measure the equation of state and the critical temperature for superfluidity [Ku12]. In Chapter 5, we measure at the first time the superfluid density in the resonantly interacting Fermi gas as a function of temperature - a quantity of fundamental importance. The particular ‘magic’ of the superfluid density, in our opinion, is that it is indeed the quantity which bridges the microscopic and macroscopic worlds in our many-body system. Microscopic relation is established via the spectrum of the elementary excitations, which affects the superfluid density in the integral sense [Lan80a]. The relation to the macroscopic world is due to the fact that superfluid density directly affects the thermodynamics and hydrodynamics of the many-body system.

1.3.2 Experimental methods

We classify now the research in the BEC-BCS crossover from methodological point of view using a very general and simple scheme represented in Fig. 1.5. The main goal of research is to understand the properties of many-body system, which we formally depicted as $|\Psi_{many-body}\rangle$. To study these properties, one prepares the system in initial state $|i\rangle$, which corresponds to some point on the phase diagram (Fig. 1.4), and wants to measure on it. There are two possibilities from here: either to immediately perform the measurement on the initial state, or to *deterministically* change the initial state into final state $|f\rangle$ and measure on the final state as it might be easier for some reason. Deterministic change is crucial to precisely recover afterwards the properties of initial state from the final-state measurement. One can then apply different methods to study either of two states. We classify them as ‘direct’, which means practically doing nothing to a system and go directly to data acquisition, and ‘indirect’ which implies some experimental procedures before the data acquisition. Although this separation might look a bit strange, we find it to well reflect the actual situation and helpful to avoid semantic confusion. Data acquisition means normally the imaging of the cloud. The measured quantity is always the density as a function of position and time $n(\vec{r}, t)$ or, more precisely, its integral along the imaging direction. From these data, depending on imaging techniques and parameters, one is able to recover the important quantities (like, for example, equilibrium density $n(\vec{r})$ or momentum $n(\vec{p})$ distributions in the trapped cloud, total number of atoms N or its time dependence $N(t)$), and conclude on the properties of the many-body state.

For example, in a hypothetical experiment one prepares a weakly interacting Fermi gas in the BCS limit, performs an absorption time-of-flight imaging, reconstructs the initial in-trap momentum distribution function and derives from it the temperature of the gas. This would be a direct temperature measurement of a weakly-attractive Fermi gas. In another hypothetical experiment, one prepares a resonantly-interacting Fermi gas, adiabatically ramps the magnetic field towards the BCS side where the first experiment was performed, applies

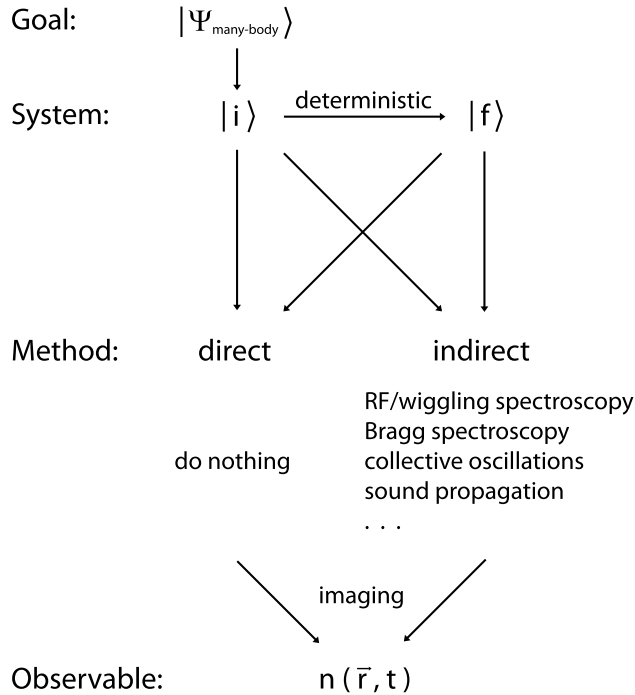


Figure 1.5: Scheme for classification of research. Arrows indicate possible routes for preparation of the system, applying the experimental procedures and data acquisition.

the Bragg spectroscopy method and from the measured density distribution calculates the temperature of weakly interacting Fermi gas, and then recovers the temperature of the initial resonantly-interacting state. This would be an indirect temperature measurement of a resonantly-interacting Fermi gas. So classified experiments, in our opinion, allow for a better vision of advantages and limitations of every approach as well as a clear separation of methods from the the system to which they are applied.

We first discuss direct methods for both initial and final state. Surprisingly, just by observing the profile of the trapped cloud one can already obtain a lot of information. By counting the number of atoms or molecules (which can be separated from atoms by Stern-Gerlach technique) in the trap as a function of time one measures the losses, which are directly related to collisional processes. This was helpful to approximately locate Feshbach resonances [O’H02b] and estimate their parameters. The controlled magnetic field ramps (into a final state) allowed for association/dissociation of weakly-bound Feshbach molecules, providing more information about the resonance position and width [Sch05]. The creation of the first BEC of paired-fermion molecules [Joc03b] was proven by measuring the total number of molecules to be about twice larger than the one expected for a thermal Bose gas in the trap. Later the characteristic bimodal density profile was clearly demonstrated as a final proof of condensation [Zwi03]. On the other side of the Feshbach resonance and towards the unitarity, the measured cloud profile showed a remarkable deviation from an ideal Fermi gas, manifesting thereby a first observation of strongly interacting degenerate Fermi gas [O’H02a]. The change of the cloud profile was then demonstrated to be continuous and reversible as one ramps the magnetic field through the crossover region [Bar04b], supporting

the idea of a smooth evolution.

Based on understanding of the atomic profiles on the BEC side, it has become possible to show a condensate of pairs to exist in the strongly interacting regime [Reg04, Zwi04] by ‘projecting’ the corresponding many-body wavefunction onto a relatively well-known molecular BEC wavefunction by means of fast magnetic field ramp. Completely analogous to the quantum-mechanical textbook state projection, this procedure shows the condensate fraction in the final state (BEC) which must be the one present in initial state. Technical limitations of experiments, however, don’t allow for a perfect projection and there seems to be some ‘evolution’ admixture still present during the ramp. The errors are relatively difficult to quantify and, in our opinion, some independent measurements are needed to validate (or refute) this projection procedure ¹⁶.

The phenomenon of superfluidity was unambiguously demonstrated by creation of vortices in a rotating Fermi gas (final state) [Zwi05], in analogy to earlier experiments on atomic BECs. Later, the predicted signature of superfluid-to-normal transition was revealed in the trapped cloud’s density profile [Zwi06a]. In our opinion, this was the first experiment, where the presence of the trap turned out a rather great advantage than just something unavoidable. Very recent experiments have directly demonstrated the key property of superfluid state, namely a frictionless flow (the drop of resistance to zero) in the resonantly interacting Fermi gas, with a carefully engineered confinement potential [Sta12].

The studies of thermodynamics in the strongly interacting state was particularly fruitful in the unitarity-limited case. Of considerable importance in this sense was the measurement of specific heat capacity [Kin05b] and formulation of the virial theorem for a trapped gas [Tho05], which gave a direct access to the energy of the system and favored the first measurements of the equation of state (EOS) at unitarity [Luo07, Hor10]. These measurements relied on thermometry performed in a final state, after an expectedly adiabatic ramp of magnetic field. The adiabaticity of the ramp, however, was not satisfied very well, giving rise to relatively large errors in temperature calibration and in the whole measured EOS. Recent measurements on the EOS were performed with a significantly better thermometry [Nas10, Nav10], or even without a need to measure the temperature [Ku12]. These experiments have used directly a specific property of harmonic trapping potential [Ho10] ¹⁷ and developed very elegant approaches to measure the EOS. The experiment of MIT group [Ku12] was able to measure the Bertsch parameter ξ and the critical temperature T_c of a unitary Fermi gas with an impressive precision.

Now we discuss the indirect methods, which were applied so far to study the BEC-BCS crossover. Several spectroscopic methods were used to understand the actual ‘structure’ of the many-body wavefunction and the origins of pairing.

RF spectroscopy [Mar88] tool was first applied to fermions [Reg03a, Gup03] to measure

¹⁶Recently, we extended the idea of interference experiments [Cas97] from weakly-interacting atomic to strongly interacting molecular condensates (Chapter 2). We found that strong interactions tend to smear out the interference pattern and prevent the interpenetration of two clouds thereby prohibiting the study in the most interesting regime around unitarity. As a conclusion, there could be made no direct comparison between our experiment and the above-mentioned ones.

¹⁷In our opinion, this is a very rare case when the usefulness of theoretical work for experiments can be hardly overestimated.

the mean-field interaction shifts and map the scattering length as a function of magnetic field near Feshbach resonance. Later, the binding energy of the universal dimer was used to precisely characterize Feshbach resonance [Reg03b, Bar05b]. The presence of pairing was observed in the whole strongly interacting regime [Chi04] as the gap in RF-spectra (‘pairing gap’, Δ). The pairing gap was shown to have a meaning of molecular binding energy on the BEC side of the resonance. Further experiments extended the pairing gap measurement to be tomographic in the trap [Shi07], and presented the measurement of the pair size [Sch08] with an experimental scheme that minimized the final-state-induced shifts. The ‘wiggling’ method based on the rf-modulation of the bias magnetic field [Gre05] was used for similar experiments, and demonstrated some advantages over the conventional rf spectroscopy.

The photo emission spectroscopy showed a possibility to resolve momentum in the rf-spectra and allowed for measurement of quasiparticle dispersion curve [Ste08, Gae10, Che09].

The optical molecular spectroscopy distinguished between free atoms and paired atoms on both sides of the Feshbach resonance [Par05], measuring hereby a closed-channel contribution into the universal bound state on molecular side. This experiment also referred to the superfluid order parameter (‘superfluid gap’, which is also denoted Δ and strictly speaking coincides with a pairing gap only in the BCS limit), however, the role played by the non-condensed pairs was not clear from measurements.

Bragg spectroscopy proved itself a powerful tool to investigate the pairing-related phenomena in BEC-BCS crossover [Vee08]. The distinction between pairs and atoms is done here by mass difference rather than by energy shifts like in rf spectroscopy. A large transferred momentum of the order of k_F allowed for sensitive study of the two-body correlations (at the corresponding distances of the order of $1/k_F$) via measuring the dynamic structure factor [Pin66, Com06], even in the strongly interacting regime. Further studies established a connection between pair correlations and the universal contact [Kuh11, Tan08a, Tan08c, Tan08b]. A method in some sense similar to the Bragg spectroscopy - a drag by moving lattice (implemented for bosons earlier: [DS05]) - was used to measure the critical velocity for superfluidity in the whole crossover [Mil07].

We will discuss now in some more details the methods employed in experiments presented in the last three chapters, namely the method of collective oscillations and the sound propagation.

The method of collective oscillations has been first used for atomic BECs [Pit03], and later applied to strongly interacting Fermi gases [Gio08]. It is based on a simple consideration that if we mechanically perturb a whole bulk of the fluid or gas about its equilibrium state, we excite a collective motion of the whole system in which the dynamics would be defined by the equilibrium properties. The crucial property of these collective oscillations is that they are normally long-lived. One is able to observe many oscillation periods and hereby define the relevant oscillation frequency and damping constant with a high precision. The simplest modes (sloshing modes) are useful to accurately characterize the trap (by measuring trapping frequencies), which is now the standard technique. Collective oscillation which affect the density of the cloud (compression modes) are sensitive to the EOS of a system. The experiments on compression modes accessed the superfluid EOS in the whole crossover [Bar04a, Kin04a]. Later measurements on radial compression mode provided crossover EOS with a much better precision, and facilitated a direct comparison to the zero-temperature predictions [Hei04].

The small beyond-mean-field correction, known as LHY correction [Lee57], was revealed for the BEC equation of state. The above-mentioned experiments also showed the signatures of transition from hydrodynamic to collisionless regime, which were studied later in more detail with surface modes [Alt07c, Wri07]. Our recent experiments on collective modes approached the EOS of the unitary Fermi gas along the temperature axis, and proved being sensitive to the interaction effects across the superfluid phase transition (Chapters 3 and 4). An interesting way to measure via collective modes the critical temperature for superfluidity was presented by study of radial quadrupole mode in a rotating gas (final state) [Rie11].

In contrast to the method of collective oscillations, the experiments on propagation of the density perturbation (sound wave) did not show a great potential for precision tests of the EOS. Clearly, the speed of sound depends on the thermodynamics of the trapped gas. The density pulse being normally excited in the center of the cigar-shaped cloud, propagates towards the boundary and eventually disappears. The quantity extracted is the speed of sound, which does not have that high accuracy as the collective mode frequency (better than 1%). Therefore, the earlier measurements on the sound propagation were more of a proof-of-principle type [Jos07] and followed the similar measurements done with atomic BECs [And97a], still demonstrating a very good agreement with an expectation from EOS results [Cap06]. One difficulty of the experiment of this type is the following. On one hand, to relatively well define the position of a propagating pulse, one needs a good signal-to-noise ratio, i.e., the deeper (higher) is the well (hill) - the better. On the other hand, the stronger is the propagating excitation, the less accurately it can be considered as a perturbation. More quantitatively, when the depth of the well becomes of the order of chemical potential in the center of the trap, this is not a perturbation anymore and the necessary corrections needed to be introduced into calculations, if not the whole concept to be changed. In this case, a compromise has to be found and the technical limitations like the quality of the imaging system matter a lot. Moreover, for the case of a deep well, one faces nonlinearities and soliton physics [Yef13]. A considerably large attention the sound-propagation experiments gained because of numerous theoretical paper on possible propagation of second sound waves in strongly interacting Fermi gases [Hei06, Tay09, Hu10, Ber10] and the experiments related to the second sound in BECs [SK98, Mep09b, Mep09a]. The formulation of Landau's two-fluid hydrodynamics turned out to be exactly applicable to the strongly interacting Fermi gases, in the broad region of phase diagram (Fig. 1.4) below the critical temperature where both normal and superfluid components exist and are strongly hydrodynamic. Our system therefore was proposed as an ideal system in the field of ultracold atoms to observe the second sound waves. While the second sound in BECs is simply a Bogoliubov sound (a density wave propagating in a condensate) [Gri97], the strongly interacting nature of our system suggested similarities with superfluid helium and a 'classical' concept of second sound as an entropy (or temperature wave). Surprisingly enough, new calculations showed that the second sound wave in our system has also a finite variation in the density. We then made an effort of inventing a very simple procedure to create a local temperature excitation (essential for coupling to the second sound ansatz [Kha65], but not to the first sound one) and observed the resulting propagation of second sound. We hope that our experiments presented in the Chapter 5, might stimulate further development of the sound propagation method.

We would like to note, that the last three methods, the Bragg spectroscopy, collective oscillations and sound propagation, have one thing in common: they all probe the density response properties of the many-body system. Therefore, they could be all treated and understood [Hu10] within a very general and well established response theory [Lan80b, Pin66]. The question is only about the type, or maybe better - regime of the excitation which we purposely choose. Can we connect these three methods and understand everything in terms of Bragg spectroscopy, for example? In Bragg spectroscopy, the excitation is done to the whole cloud and is essentially delocalized in space, but localized in momentum and energy. In the sound propagation experiment, one uses a perturbation which is pretty much localized in space that would correspond to a wavepacket in momentum space. The total energy transfer in this case becomes an integral quantity over the momenta of the wavepacket. The collective oscillation represents a limiting case of a sound propagation of a very narrow momentum wavepacket, which corresponds to the oscillation of the whole *trapped* system in real space. This is the effect of the boundary conditions imposed by the trapping potential, which ‘narrows down’ the momentum width of a sound excitation. This is analogous to the laser linewidth narrowing by cavity, with a difference that reflection happens not at the mirrors in the ends of a cavity, but in the whole harmonic trap as its walls gradually rise. Only the certain waves survive after this distributed reflection to form a collective mode in a given trap geometry. From this intuitive arguments we see that perhaps the collective oscillations can be approached from Bragg spectroscopy perspective. This is why it makes sense to discuss the low-frequency impact, generated by collective modes, in the dynamic structure factor and density response function which can be revealed in Bragg spectroscopy experiment [Hu10, Tay07]. For the local density perturbation, propagating through the cloud, the interpretation in terms of Bragg spectroscopy would be problematic. As to our knowledge, there were no experiments demonstrating the collective-modes impact by Bragg spectroscopy and the latter is still ideologically detached from the other two methods used in our experiment.

1.3.3 Extensions of the crossover physics

Here we list the ‘extensions’ of strongly interacting fermions beyond our model BEC-BCS crossover system based on a balanced two-spin mixture of a single specie. These extensions are realized via tuning additional parameters, such as balance between population of two spin states or the total number of atoms, creating a mixture of fermions of more than two spin states or of a different species (mass imbalance), and exploring the different geometries. As these topics are outside of the scope of the present thesis, we restrict ourselves to just sketching the directions and providing the links to relevant papers or reviews.

1) *Spin and mass imbalance.* Realization of spin and mass-imbalanced Fermi mixtures opened the new possibilities for research on superfluidity and for creation of new phases of fermionic matter. The comprehensive review of the imbalanced Fermi gases is given in [Che10, Rad10].

2) *More spin states.* Creation of a mixture of fermions in three different spin states allowed to study universal 3-body physics (Efimov physics), which was a subject of extensive research with ultracold bosons [Fer11]. The first experiments in the universal few-body domain with

fermions were reported [Ott08] in the 3-state mixture of spin states of ${}^6\text{Li}$ (three lower energy states in Fig. 1.1b).

3) *Few-particle physics.* Deterministic preparation of a few-particle system along with single-particle-sensitivity detection procedures allowed to probe the fundamental properties of fermions [Ser11]. The advantage of the few-particle system is obviously its simplicity: the results of experiments can be directly compared to numerical simulations and sometimes to exact theoretical solutions.

4) *Lower dimensions and optical lattices.* Different geometrical configurations were created by means of additional confinement potentials. Specially engineered optical dipole trapping potentials (tightly focused, crossed, phase masked) and the optical lattices provided a rich toolbox for controlling the dimensionality of a system, from 3D to 0D, allowing the realization of many interesting phases and study of quantum phase transitions (for example, the Mott insulator-superfluid transition with bosons) [Blo08]. Optical lattices, combined with single-site resolution imaging technique, have set up an excellent playground to engineer and study all different kinds of Hubbard-like Hamiltonians, even beyond the known solid-state analogs. This opened the way to exciting world of quantum simulations [Blo12], initially performed with bosons and recently also with fermions (see the next section).

5) *Topological states of matter.* Another quantum-simulation-related topic, spin-orbit coupling in ultracold gases [Gal13], deals with recently revived interest in topological states of matter studied earlier in solid state. Study of spin-orbit-coupled Fermi gases and in particular the BEC-BCS crossover in these systems is therefore an interesting perspective.

1.4 Outlook

The physics of BEC-BCS crossover system has been a subject of intense research already for about ten years, which is a considerably long period on the timescales of the field of ultracold atoms. During this ten years, numerous properties of the system were well understood, from both experimental and theoretical side. This knowledge is summarized in comprehensive review articles, and is soon (if not yet) about to become a textbook material. In view of this, it might be natural to put forward a question if the research on BEC-BCS crossover physics, and even broader - strongly interacting Fermi gases, is entering the saturation phase. From experimental point of view, a saturation can easily occur if either the system we explore becomes too complicated or not so suitable to address a certain fundamental problem, or the set of available methods puts a strong limit on the range of accessible problems. Therefore, there are two directions in which one can push the boundaries. First direction assumes the modification of the old system or creation of new systems, still being built of strongly interacting fermions, but with even more control over the internal and motional degrees of freedom. The second direction is connected with improving the old or inventing the new methods to probe the existing many-body system. Here we briefly present our vision of the general tendencies for studying strongly interacting fermionic systems, and focus more on the perspectives of our experiment.

1.4.1 Strongly interacting fermions

With the ongoing experiments performed on the above-mentioned ‘extended’ systems, the general trend, in our opinion, is creation and study of new model system (based on extension no. 4 in the previous section) that offers as high as possible level of control and manipulation and allows to address a different physics, compared to the old BEC-BCS crossover model. The creation process is almost completed by now. A new class of fermionic quantum simulators, similarly to already created bosonic ones, still has a macroscopically large number of atoms to study the many-body physics, while in addition to the available ‘bulk’ operations, realizes a possibility of high-precision operations at the level of a single atom. A model system for these experiments is a Fermi gas with tunable interactions in a two-dimensional optical lattice (for instance, in xy -plane), with an additional confinement into a pancake-like structure along the third direction (z -axis). The crucial element of an experimental setup is a high-resolution objective placed in xy -plane above the 2D-array of atoms, which provides both the single-site resolution imaging and the single-site-addressed operations for any atom in a 2D-array. The full advantage of the optical lattices toolbox is taken to create a variety of possible orderings in the plane. If one switches the optical lattice off, it is possible to study the many-body physics in the bulk, but in a 2D or quasi-2D geometry. An additional degree of freedom (still remains to be better controlled in experiment) is creation of different number of pancakes in z -direction and tuning the coupling between adjacent pancakes.

Of course, the range of physical problems which can be studied with this simulator, is very large. It partially includes the topics studied on the old bulk model like pairing, superfluidity etc., as well as the new topics like spin-orbit coupled Fermi gases (extension no. 5 in previous section). In addition, such a system would be even closer to the high T_c superconductors, where the CuO_2 layers are weakly coupled and most of the interesting physics happens within the layers, i. e., in a 2D-configuration.

1.4.2 Open questions in BEC-BCS crossover

There is still a number of ‘white spots’ on the phase diagram of the BEC-BCS crossover (Fig. 1.4). Here we try to list the most interesting questions from our point of view.

First, the EOS is well known only in the limiting cases, which can be represented by four lines on the phase diagram: at zero temperature along the interaction axis, and at unitarity and in the BEC and BCS limits along the temperature axis. Knowledge of the EOS in the rest of the phase diagram could provide us with precise information on the thermodynamic quantities and allow for testing the relevant theories. However, the corresponding measurements seem to be very complicated.

Second, the phenomenon of superfluidity is not completely understood in strongly interacting regime: the critical temperature for superfluidity and the superfluid fraction were measured only at unitarity, while there is still no theory that would predict both of these fundamental quantities consistently and correctly at the same time.

Third, the phenomenon of superfluidity has not yet been studied far from the unitary limit on the BCS side, as the critical temperature decreases exponentially with decrease of interaction strength (according to BCS theory) and becomes too small to be reached in

current experiments. The progress in cooling methods could enable research in this part of the phase diagram.

Fourth, a question related to the superfluidity - the spectrum of elementary excitations, needs to be understood better. One point which is still unclear is how the two branches of the excitations (bosonic phonon branch, and fermionic single-particle branch) contribute to the normal density. Another interesting question is whether we can understand the similarity of the superfluid fraction of the unitary Fermi gas to the one of superfluid helium in terms of spectra of elementary excitations of these systems.

Fifth, the dissipation effects in both superfluid and normal hydrodynamic regimes have not been studied thoroughly. As the transport coefficients (viscosity and thermal conductivity) are normally neglected in the theoretical treatment of two-fluid hydrodynamics for simplification reasons, the information about the dissipation processes is lost. However, a clear damping of sound waves and collective excitation modes is observed in experiment. The first measurements on viscosity of unitary Fermi gas were recently presented in Refs. [Cao11a, Cao11b], while the thermal conductivity has not been measured yet.

Finally, the pseudogap region of the phase diagram needs to be understood better. A different from harmonic trapping configuration (for example, box-like trapping), might help to broaden the temperature window between T_c and T^* (see Fig. 1.4) and make the study of pseudogap regime at unitarity more convenient.

1.4.3 Second sound prospects

Now we discuss a possible set of experiments connected to the topic of second sound. These experiments address some of the above-mentioned open questions.

Second sound in BEC-BCS crossover

A straightforward extension of the second sound measurements at unitarity would be the measurement of second sound in the whole BEC-BCS crossover. There are already existing theoretical predictions for the speed of second sound, based on calculations using different many-body theories [Hei06]. We believe that it must be possible to measure the absolute values of the second sound speed similarly to how it was done for the unitary Fermi gas, as soon as the second sound wave can be excited. Application of the effective 1D hydrodynamic formalism and extracting the local superfluid fractions, however, can be a nontrivial task for the whole BEC-BCS crossover region. One reason for this is that at any finite scattering length a (away from resonance) the value of interaction parameter $1/k_F a$ depends on position in the trap. To overcome this problem, one would probably need to introduce an effective $1/k_F a$ - average over the radial direction and dependent on z-position only. Even if this description turns out to be adequate, it will still introduce additional errors. Another problem is that the equation of state, required for calculation of all the thermodynamic parameters, is well known only at unitarity. It is therefore not clear how to reliably determine the the global temperature of the gas in the whole strongly interacting region. Study on the BCS side seems to be quite challenging, as the critical temperature for superfluidity becomes exponentially small there. This means that already relatively near to the resonance towards the BCS side, one enters the normal fluid regime where the second sound should not

exist. In the limit of weakly interacting molecular BEC, one might naively expect, that the second sound should behave similarly to the second sound in atomic BECs. If this is true, then it would be of great interest to observe the *conceptual* evolution of second sound from unitarity (an isobaric wave, similar to original concept introduced in superfluid helium) to the BEC limit (a density wave confined to the condensate, Bogoliubov sound). This study, however, can be complicated by the overall decrease of the ‘hydrodynamicity’ of the normal part away from the resonance. Nevertheless, we think, that even a qualitative understanding of propagation of the second sound in the BEC-BCS crossover can be very interesting. In particular it can give a first estimate for the value of superfluid fraction in the crossover, using the already available theoretical models for calculating the necessary thermodynamic quantities.

Second sound collective excitations

In analogy to the first-sound-like collective oscillations (modes) in unitary Fermi gas, one can also consider the second-sound collective modes in different trap geometries [Tay08, Hu10, Hou13b]. Using an effective 1D hydrodynamic approach, it is possible to calculate the mode profiles and frequencies of the second-sound axial collective modes [Hou13b] for an experimentally relevant situation of highly-elongated harmonically trapped cloud, similarly to what is shown in Chapter 4. However, it is unclear how to excite these modes in experiment. While for the first-sound modes one can drive the given mode at a resonant frequency with a carefully adjusted density perturbation, engineering a corresponding periodic temperature perturbation seems to be a nontrivial task. A different approach to the excitation of second sound modes might be developed based on the predicted coupling between first-sound and second-sound modes of proper symmetry¹⁸. The origin of coupling might be intuitively understood from the fact that second sound has a finite and relatively large response in the density, especially for the temperatures close to T_c . The drawback of this procedure is the following: resulting second sound mode is still expected to be weak, compared to the first-sound mode, while the damping of the second sound is estimated to be stronger than that of the first sound. This means that one would always need to detect a weak second-sound perturbation on top of the strong first-sound one. In this situation, a sensitive detection becomes possible only if the noise introduced by data post-processing is smaller than the actual noise in the data. Therefore an experiment on second sound modes, in our opinion, requires a high-precision measurements and very good stability of experimental setup. The results, however, can be very rewarding. A precise measurement of second-sound mode frequencies and damping rates could provide a way more accurate information on superfluid fraction as compared to available now.

Second sound in imbalanced unitary Fermi gas

A simple modification to an existing system would be to introduce a spin imbalance between two components. The EOS of an imbalanced Fermi gas at unitarity was measured by Paris group [Nav10], therefore all the necessary thermodynamic functions can be calculated with sufficient precision. In this case, a similar experimental procedures as in Chapter 5 can be applied to excite and detect the second sound. It would be of a considerable interest to

¹⁸From private communication with Y.-H. Hou, L. Pitaevskii and S. Stringari.

directly compare the propagation patterns of second sound for balanced and imbalanced case. As the spin polarization in case of a slight imbalance has a distinct three-phase distribution in the trap [Che10], with a fully balanced part around the center, finite imbalance in the intermediate region, and fully polarized outer shell, one would expect to see a completely identical propagation in the central region, while a clear deviation appearing at the first phase border. It is really puzzling, how the second sound will propagate in the region with finite imbalance: whether it will show strong dissipation and how will its behavior depend on spin polarization. Such an experiment can be a valuable contribution to quantitative understanding of superfluidity in the imbalanced Fermi gas.

Second sound as a tool

What we discuss here is not a proposal for any particular experiment, but rather a consideration which we found useful to formulate, supported with one example case. We now shift the emphasis from the study of the properties of second sound (which certainly need to be understood better) and consider second sound more as a tool to *locally* probe our system, based on what we already know. Indeed, the measurement of a local speed of the second sound gives an immediate access to 1D superfluid density, which is a local quantity on the lengthscale set by longitudinal trapping. We ask ourselves: could the z-profile of the superfluid fraction provide, supported with an effective 1D hydrodynamic formulation, the information about global quantities? Especially, this opportunity might be of interest in regimes, where the thermodynamic quantities cannot be extracted reliably for any reason. As an example, we consider here a hypothetical unitary Fermi gas at a very low temperature of the order of $0.01 T_F$. In this regime, the thermally-affected wings of the cloud are so small, that fitting the cloud's profile with a profile known from the EOS might be not sensitive enough to give an accurate result for the global temperature T . The z-dependence of superfluid fraction, or equivalently, the propagation pattern of the second sound perturbation, in this case might provide more information. A possible way to measure would be to ramp the magnetic field slightly to the BCS side, but far enough to get a considerable drop of critical temperature and observe a clear change in the sound propagation pattern as compared to $T = 0.1T_F$ case. The critical temperature T_c on the BCS side can be then taken from Ref. [Per04] for some effective radially-averaged value of $1/k_F a$, at z-position where the second sound disappears. This critical temperature will be then equal to the global temperature T . The question of how good the description in terms of effective $1/k_F a$ is, should be addressed in experiments on second sound in the BEC-BCS crossover, as we discussed above.

1.5 Overview

This thesis includes four articles, contained in the following four chapters. Contribution of the author of the present thesis to the article is indicated by a footnote at the first page of each chapter. In the present thesis we do not provide a detailed description of an experimental setup, which can be found in the previous diploma [Hen03, Rie04, Koh07] and PhD theses from our group [Joc04, Bar05a, Alt07a]. The most recent updates to experimental setup are briefly summarized in [SG11]. Here we give a short overview of the topics, covered by this thesis.

Chapter 2, *Observation of interference between two molecular Bose-Einstein condensates*: we observe interference between two Bose-Einstein condensates of weakly bound Feshbach molecules. An interference pattern clearly demonstrates the de Broglie wavelength of molecules. As the interaction strength increases, elastic collisions destroy interference pattern by removing the particles from the condensate wavefunction. For even stronger interaction the condensates do not anymore penetrate each other as they collide hydrodynamically.

Chapter 3, *Higher-nodal collective modes in a resonantly interacting Fermi gas*: we develop experimental techniques to study higher-nodal longitudinal collective oscillations in a highly elongated, harmonically trapped unitary Fermi gas. We employ a resonant local excitation scheme to selectively drive a given collective mode. The detected time evolution of the axial density profile is sensitively analyzed to extract the mode profile, frequency and damping rate of the modes. The results for temperature dependence of the mode parameters across the superfluid phase transition show an excellent agreement with theoretical predictions based on Landau's two-fluid theory and available experimental knowledge of the equation of state.

Chapter 4, *Collective Modes in a Unitary Fermi Gas across the Superfluid Phase Transition*: we investigate both experimentally and theoretically the temperature dependence of the collective oscillations of first sound nature in a highly elongated harmonically trapped Fermi gas at unitarity, around the critical temperature for superfluidity. We focus on precision measurement of hydrodynamic frequencies of these higher-nodal excitations, which show a pronounced temperature dependence as contrasted to any collective mode studied before. Experimental results agree very well with theoretical predictions based on Landau's two-fluid approach. Moreover, our results provide an independent confirmation of the recently measured equation of state [Ku12].

Chapter 5, *Second sound and the superfluid fraction in a resonantly interacting Fermi gas*: we report on the first observation of second sound propagating in a superfluid Fermi gas. The speed of second sound is extracted, based on the effective 1D formulation of the Landau's two-fluid hydrodynamics. Using the universal thermodynamic relations for resonantly interacting Fermi gas, we reconstruct the temperature dependence of the superfluid fraction, a previously inaccessible quantity that will provide a benchmark for theories of strongly interacting quantum gases.

Chapter 2

Publication: Observation of interference between two molecular Bose-Einstein condensates[†]

New J. Phys. **13**, 065027 (2011)

C. Kohstall^{1,2}, S. Riedl^{1,2}, E. R. Sánchez Guajardo^{1,2}, L. A. Sidorenkov^{1,2}, J. Hecker Denschlag¹, and R. Grimm^{1,2}

¹*Institut für Experimentalphysik und Zentrum für Quantenphysik, Universität Innsbruck, 6020 Innsbruck, Austria*

²*Institut für Quantenoptik und Quanteninformation, Österreichische Akademie der Wissenschaften, 6020 Innsbruck, Austria*

We have observed interference between two Bose-Einstein condensates of weakly bound Feshbach molecules of fermionic ^6Li atoms. Two condensates are prepared in a double-well trap and, after release from this trap, overlap in expansion. We detect a clear interference pattern that unambiguously demonstrates the de Broglie wavelength of molecules. We verify that only the condensate fraction shows interference. For increasing interaction strength, the pattern vanishes because elastic collisions during overlap remove particles from the condensate wave function. For strong interaction the condensates do not penetrate each other as they collide hydrodynamically.

2.1 Introduction

Interference manifests the wave nature of matter. The concept of matter waves was proposed by de Broglie in 1923 [Bro23] and now represents a cornerstone of quantum physics. Already in the 1920's, experiments demonstrated the diffraction of electrons [Dav27] and of atoms and

[†]The author of the present thesis contributed to the data analysis.

molecules [Est30]. These early achievements led to the field of atom optics and interferometry [Ada94, Bon04, Cro09].

With the realization of Bose-Einstein condensates (BECs) [And95, Dav95, Bra95], sources of macroscopically coherent matter waves became available. The interference between two BECs was first observed by Andrews et al. [And97b]. This landmark experiment evidenced interference between two independent sources and revealed the relative phase between them [Cas97]. Since then, interference measurements have developed into an indispensable tool for research on BEC. Applications include detection of the phase of a condensate in expansion [Sim00], investigation of a condensate with vortices [Ino01], and studies of quasi-condensates [Had06] or Luttinger liquids [Hof07] in reduced dimensions. Another fundamental line of research in matter-wave optics is to explore the transition from the quantum to the classical world by detecting the wave nature of progressively larger particles, like clusters [Sch94], C_{60} [Arn99], and other giant molecules [Ger11].

The creation of molecular Bose-Einstein condensates (mBECs) of paired fermionic atoms [Joc03b, Gre03, Zwi03] provides us with macroscopically coherent molecular matter waves. In this article, we present the interference of two such mBECs and demonstrate interference as a tool to investigate condensates of atom pairs. This work extends the interference of condensates towards larger, composite particles.

In a Young-type interference experiment, we release two mBECs from a double-well trap and, after the condensates have overlapped, we observe an interference pattern by absorption imaging. In Sec. 2.2, we describe the experimental procedures in detail. In Sec. 2.3, we present our main experimental results, demonstrating the *molecular* de Broglie wavelength and the dependence of the interference contrast on temperature and interaction strength. Increasing the interaction strength reduces the visibility because of increasing elastic scattering losses depleting the coherent matter wave. Section 2.4 gives an outlook to possible extensions and applications of interference of pair condensates.

2.2 Experimental procedures

2.2.1 Preparation of the molecular Bose-Einstein condensate

We create a molecular Bose-Einstein condensate (mBEC), starting from an atomic Fermi gas consisting of an equal mixture of ${}^6\text{Li}$ in the lowest two spin states. The preparation follows the procedures described in our previous work [Joc03b, Bar04b, Alt07b, Rie08].

The atoms are trapped in the potential of a focused, far red-detuned laser beam with a beam waist of $45\ \mu\text{m}$, derived from a 25 W, 1030 nm single-mode laser source, as illustrated in Fig. 2.1. We choose the coordinate system such that the laser beam propagates along the z -axis and gravity acts in $-y$ -direction. A magnetic bias field B can be applied along the y -axis. A broad Feshbach resonance centered at $B = 834\ \text{G}$ [Bar05b] facilitates precise tuning of the atomic s -wave scattering length a . Below resonance, a weakly bound molecular state exists [Joc03a]. Molecules in this state represent halo dimers, since their wave function extends far into the classically forbidden range [Fer08]. Their size is given by a and their binding energy is $\hbar^2/(ma^2)$, where m denotes the atomic mass and \hbar is Planck's constant h divided by 2π . The intermolecular scattering length is $a_M = 0.6a$ [Pet05b].

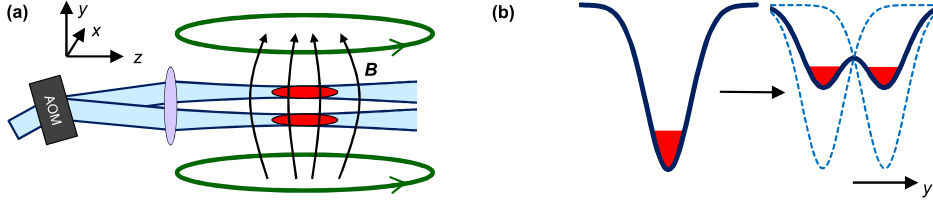


Figure 2.1: Illustration of the trapping and splitting of the mBEC in the presence of a magnetic field B . An acousto-optical modulator (AOM) toggles the laser beam between two positions, which creates an effective double-well potential for trapping two mBECs. (a) Along the x - and y -directions, the optical potential is dominant; along the z -axis the magnetic potential is dominant. (b) The potential shape of the optical dipole trap is Gaussian. The double-well potential is generated from the superposition of two Gaussian potentials.

To create the mBEC we perform evaporative cooling by reducing the laser beam power at a constant magnetic field $B = 764$ G. During evaporation, the halo dimers are created through three-body collisions [Joc03b] and eventually they form a mBEC [Ing08]. After evaporation, we increase the trap depth, thereby compressing the condensate, to avoid spilling particles in all further steps of the experimental sequence. The beam power is adiabatically increased by a factor of about 10 to 45 mW. The trap center can be closely approximated by a harmonic potential. The oscillation frequencies of the molecules, which are the same as the ones of free atoms, are $(\omega_x, \omega_y, \omega_z) = 2\pi \times (250, 250, 20.6 \times \sqrt{B/700 \text{ G}})$ Hz. The axial confinement essentially results from the curvature of the magnetic field. We obtain a cigar-shaped cloud containing $N = 1.8 \times 10^5$ molecules. The condensate fraction exceeds 90% [Joc03b].

Most of our measurements are carried out in the regime of weak interaction between the molecules. We ramp the magnetic field adiabatically down to 700 G in 200 ms, thereby decreasing the scattering length to about $a_M = 1000 a_0$; at lower fields the molecules become unstable [Pet05a, Cub03, Joc03a] and limit the lifetime of the mBEC. At 700 G, the chemical potential of the mBEC is $k_B \times 200$ nK, with k_B denoting the Boltzmann constant, and the binding energy of the molecules is $k_B \times 8 \mu\text{K}$. In view of the crossover from BEC to a Bardeen-Cooper-Schrieffer (BCS) type regime [Gio08, Ing08], one can also express the interaction conditions in terms of the commonly used dimensionless parameter $1/(k_F a)$, where k_F is the Fermi wave number of a non-interacting Fermi gas with $(\hbar k_F)^2/(2m) = E_F$, where $E_F = \hbar(6N\omega_x\omega_y\omega_z)^{1/3}$ is the Fermi energy. For the condition of our mBEC at 700 G we obtain $1/(k_F a) = 3$. Strongly interacting conditions are realized for $1/(k_F a) < 1$, which can be achieved at fields closer to resonance.

2.2.2 Condensate splitting

The mBEC is split into two equal parts along the y -axis. We transform the Gaussian shaped optical dipole potential into a double-well potential, as illustrated in Fig. 2.1(b). This is accomplished by using time-averaged potentials. An acousto-optical deflection sys-

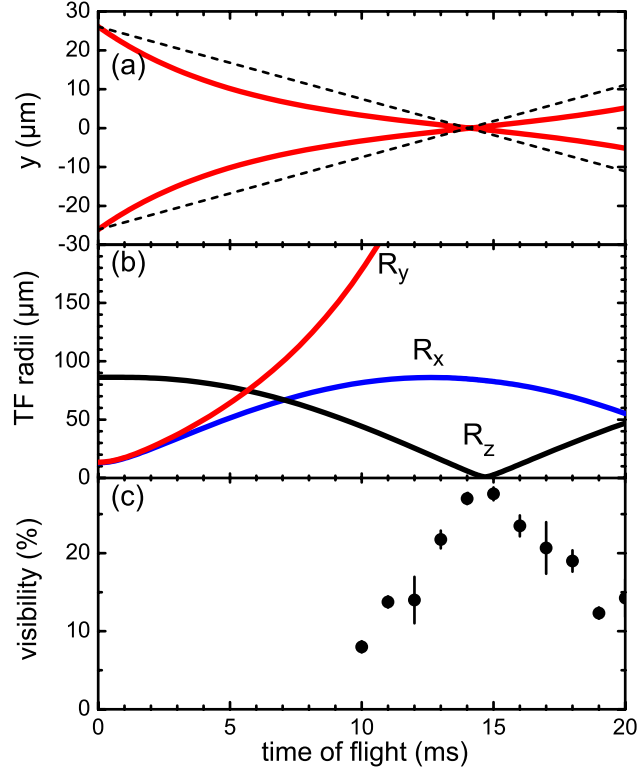


Figure 2.2: Expansion dynamics of the condensates in the magnetic saddle potential. (a) The solid lines are the calculated center-of-mass motion of the condensates, taking into account an initial kick towards each other, see text. The trajectories intersect after $t_{\text{TOF}} = 14$ ms. For comparison, the dashed lines represent the trajectories of particles in free expansion intersecting at the same point. (b) The calculated Thomas-Fermi radii of the condensates show the expansion along the x - and y -axis and the compression along the z -axis. The initially cigar-shaped mBEC evolves into a flat disc. (c) The measured visibility of the fringe pattern shows a clear peak, which coincides with the minimum in R_z . The bars indicate the statistical uncertainties derived from 10 individual measurements.

tem modulates the trapping beam position so fast that the atoms do not follow and feel the time-averaged beam intensity as their motional potential [Alt07c, Shi04]. The modulation frequency is 200 kHz and the trapping beam is toggled between two positions, the distance of which is increased from 0 to $68 \mu\text{m}$ within 50 ms. The distance between the minima of the resulting double well is somewhat smaller because the two Gaussian potentials still overlap. The measured distance between the centers of the two condensates is $s = 56 \mu\text{m}$ and the measured oscillation frequencies in each well are $(\omega_x, \omega_y, \omega_z) = 2\pi \times (164, 146, 20.6 \times \sqrt{B/700 \text{ G}}) \text{ Hz}$. The chemical potential of both condensates is $k_B \times 100 \text{ nK}$ and the interaction parameter is $1/(k_F a) = 4$. The barrier height is $k_B \times 160 \text{ nK}$, which leads to a fully negligible tunneling rate. The number ratio between the two condensates after splitting is sensitive to imperfections of the optical potential. To control equal number splitting, we fine-tune the magnetic gradient field that is applied to compensate for the effect of gravity.

2.2.3 Expansion in the magnetic field

The specific expansion dynamics of the released mBECs in our setup is the key to making interference clearly observable, and the understanding of the expansion is essential for the interpretation of our results. We identify two effects, which result from the curvature of the magnetic field, that are favorable for the observation of interference.

The coils generating the magnetic offset field in our set-up are not in Helmholtz configuration, which leads to second-order terms in $B(x, y, z)$. The resulting magnetic potential is a saddle potential, where the molecules are trapped along the x - and z -directions, but they are anti-trapped along the y -axis, the symmetry axis of the field. The oscillation frequencies are $(\omega_x, \omega_y, \omega_z) = 2\pi \times (20.5, i \times 29, 20.5) \times \sqrt{B/700} \text{ GHz}$, where the imaginary frequency denotes the anti-trap along the y -axis.

We model the expansion by adopting the scaling approach as applied in Refs. [Men02, Alt07c]. Figure 2.2(b) shows the predicted evolution of the Thomas-Fermi (TF) radii R_x , R_y and R_z , which we also verify experimentally. At the beginning, the expansion is driven by the pressure gradient in the cloud, which leads to a fast acceleration in the radial direction. This expansion is then further accelerated along y and decelerated along x because of the magnetic saddle potential. Along the z -axis, the long axis of the trapped cloud, the trap remains basically unchanged when the cloud is released from the optical potential. As the mean field pressure of the expanding cloud decreases, the magnetic confinement leads to a spatial compression of the cloud. We find that after $t_{\text{TOF}} \approx 14 \text{ ms}$ the parameter R_z has a minimum because of this compression effect.

For high interference contrast, large overlap of the two clouds at the time of detection is essential. To achieve this, the condensates are kicked towards each other by switching on the original single-well trap, typically for 0.1 ms right after release from the double well. The solid lines in Fig. 2.2(a) show the calculated center-of-mass motion of the clouds after the initial kick to assure large overlap at $t_{\text{TOF}} \approx 14 \text{ ms}$.

The interference pattern is determined by the relative velocity between the two condensates. The relative velocity v_{rel} at $y = 0$ and $t_{\text{TOF}} = 14 \text{ ms}$ can be directly deduced from the slopes of the solid lines in Fig. 2.2(a). This velocity is substantially smaller than it would be in free expansion without magnetic potential, where particles meeting at $y = 0$ and $t_{\text{TOF}} = 14 \text{ ms}$ would follow the dashed trajectories in Fig. 2.2(a). This deceleration of v_{rel} can be readily visualized by the condensates climbing up the potential hill resulting from the anti-trap in y -direction. This anti-trap also accelerates the expansion in y -direction, see R_y in Fig. 2.2(b). Remarkably, since the velocity field in each of the clouds stays linear, v_{rel} is independent of the position. More rigorously, we calculate v_{rel} using the scaling approach and taking into account the center-of-mass motion of the clouds.

Thus expansion dynamics brings about two favorable effects: First, the spatial compression along the z -axis facilitates clear detection of interference fringes by absorption imaging. Second, the decreased relative velocity leads to an increased fringe period. This means that the anti-trap acts as a magnifying glass for the interference fringes.

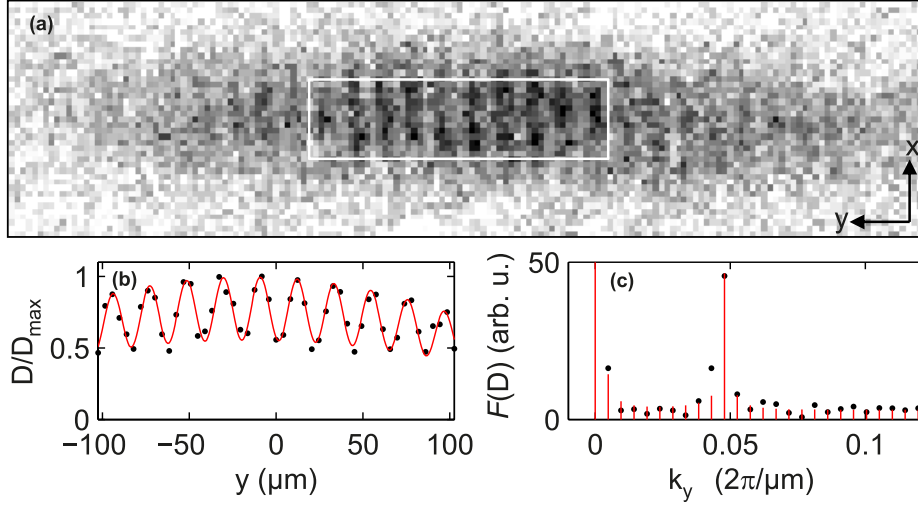


Figure 2.3: Interference image and analysis. (a) The column density along the z -axis after $t_{\text{TOF}} = 14\text{ms}$ shows the interference pattern. The field-of-view is $660\ \mu\text{m} \times 170\ \mu\text{m}$. The inner box indicates the region used for analysis. (b) The column density integrated along x gives the density distribution D along y (dots). The solid curve is the result of the fit in Fourier space, see text. (c) The density distribution is Fourier transformed (dots) and fitted (bars).

2.2.4 Detection and analysis of interference fringes

We detect the clouds by absorption imaging. Figure 2.3(a) shows a typical image of interference after 14 ms time of flight. The imaging beam propagates along the z -axis. It is overlapped with the trapping beam using dichroic mirrors. The imaging light pulse is on for $10\ \mu\text{s}$ and its intensity is about the saturation intensity of ${}^6\text{Li}$ atoms. We state-selectively image the atoms in the second-to-lowest Zeeman state. Already the first photon scattering event is likely to dissociate the weakly bound molecule [Bar04b], followed by about 10 more photons scattered by the free atom.

From the absorption images, we determine the visibility and fringe period of the interference pattern. The column density is integrated along the x -direction over the region depicted in Fig. 2.3(a)¹ resulting in a one-dimensional density distribution D , shown in Fig. 2.3(b). The density distribution contains various kinds of noise (e.g. photon or atom shot noise, or camera readout noise), which may be misinterpreted as interference signal. Therefore we analyze the density distribution in Fourier space by considering the Fourier transformed density distribution $\mathcal{F}(D)$, see Fig. 2.3(c). Here all those types of noise are approximately white and show up as a constant offset, whereas, the signal of interference is monochromatic and shows up as a peak. This gives the possibility to subtract the average contribution of noise from the signal. We determine the visibility and fringe period by the custom fit

¹The size of the region was chosen to produce the optimal signal to noise.

function in Fourier space

$$f = \sqrt{|\mathcal{F}((a + b y + c y^2) \times (1 + v \sin(2\pi/d y + \phi)))|^2 + n^2}, \quad (2.1)$$

yielding the fringe period d , the visibility v , and the relative phase ϕ . The term $a + b y + c y^2$ account for the somewhat non-uniform density distribution. The white noise n is the offset in Fourier space. Since the phase between the signal and the noise is random, the corresponding contributions are added quadratically. The discrimination of the noise via this fitting routine is crucial when the visibility is low.

The largest observed visibility is about 30%. We find that this upper limit can be essentially attributed to the finite resolution of our imaging system. We determine the modulation transfer function of the imaging system and it gives about $30 \pm 10\%$ visibility for structures with period $d = 20 \mu\text{m}$. Also other sources can contribute to a reduction of visibility, like a blurring because of a limited depth of focus or a tilt of the planes of constructive and destructive interference. The planes are in general somewhat tilted with respect to the line of sight, thereby obscuring the fringe pattern on the image. But these effects are suppressed by the spatial compression along the imaging axis caused by the magnetic saddle potential. This can be seen by comparing the compression of R_z in Fig. 2.2(b) to the detected visibility in Fig. 2.2(c). The minimum of R_z after $t_{\text{TOF}} = 14 \text{ ms}$ coincides with the peak in visibility. The peak value of almost 30% agrees with the resolution limit of the imaging system. All following measurements are performed when the clouds are compressed to about $1 \mu\text{m}$ along the imaging axis; in this case, only the limited resolution is relevant. The spatial compression is an alternative to the slicing imaging technique used in Ref. [And97b] and brings along the advantage that all particles are imaged.

2.3 Experimental results

The observed interference pattern is the standing wave formed by two macroscopically occupied matter waves, the two molecular BECs. Here we present our main experimental results. In Sec. 2.3.1, we investigate the fringe period, which evidences that the interfering particles are molecules. In Sec. 2.3.2, we study the visibility when heating the cloud to above the critical temperature for condensation to show that the interference is established by the condensate fraction. In Sec. 2.3.3, we explore the dependence of the visibility on the interaction strength and find that non-forward scattering processes depopulate the momentum component of the matter wave that is responsible for the interference pattern.

2.3.1 Fringe period

The fringe period is an central observable in interference experiments. Figure 2.4 shows the measured fringe period at $B = 700 \text{ G}$ as a function of time of flight. The de Broglie relation yields the fringe period

$$d = \frac{h}{M v_{\text{rel}}}, \quad (2.2)$$

which is determined by the mass M of the interfering particles and by the relative velocity v_{rel} of the two condensates. In our experiment, we calculate v_{rel} from the expansion and

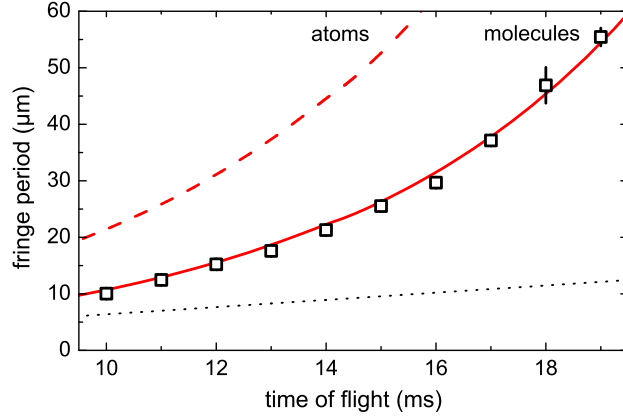


Figure 2.4: Fringe period as a function of time of flight. The symbols are the measured periods with bars, mostly smaller than the symbol size, indicating the statistical uncertainties resulting from 10 individual measurements at a given time of flight. The solid line is the calculated period for molecules and the dashed line for atoms. For free expansion without the magnetic saddle potential, the fringe period of molecules would be much smaller (dotted line).

center-of-mass motion of the condensates in the magnetic field curvature, as discussed in Sec. 2.2.3. The result is in contrast to the simple relation $v_{\text{rel}} = s/t_{\text{TOF}}$ that holds for the free expansion usually considered in experiments of this type. The solid line in Fig. 2.4 displays the calculated fringe period d for molecules, where we set $M = 2m$. All input parameters for this calculation are determined independently. Their combined uncertainties result in typical uncertainty of 3% for the fringe period, with the main contribution stemming from the uncertainty in the cloud separation. The data are in remarkable agreement with the calculation. For comparison, we also plot the fringe period for interfering atoms ($M = m$), which is clearly incompatible with the data.

The dotted line in Fig. 2.4 displays the fringe period that would result for freely expanding mBECs without the magnetic saddle potential. Comparing this curve to the much larger fringe period that we observe, highlights the effect of the magnetic field curvature to magnify the fringe period, as discussed in Sec. 2.2.3. The same magnification effect was reported in Ref. [Zaw10].

Note that the fringe period can be increased by interaction-induced slowing down of the two overlapping condensates [Sim00]. The mean-field of one condensate represents a potential hill for the other condensate, which slows down when climbing this hill. Under our experimental conditions at 700 G, the effect is found to be negligible. For stronger interaction, we see indications of this effect in agreement with a corresponding model calculations.

2.3.2 Dependence of interference visibility on condensate fraction

To demonstrate that the interference results only from the condensed molecules and not from the thermal fraction, we perform a controlled heating experiment and show the loss

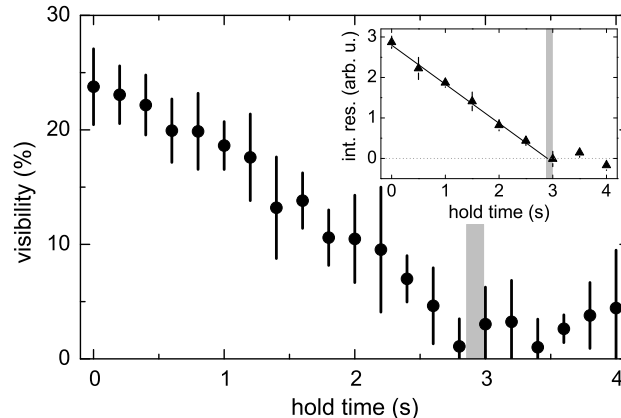


Figure 2.5: Visibility of interference for increasing temperature. The main figure shows the measured mean visibility with bars indicating the standard deviation resulting from 11 measurements. Here, we plot the standard deviation and not the statistical uncertainty to better illustrate the range of measured values. During the hold time in the trap, the temperature increases from low temperature to above T_c . The hold time after which T_c is reached is indicated by the grey bar. The inset shows the integrated residuals of a Gaussian fit, see text. A linear fit to the first six points facilitates a simple extrapolation to zero, which marks the vanishing of the condensate fraction.

of visibility with vanishing condensate fraction. Starting from an almost pure condensate [Joc03b], we hold the gas in the recompressed optical dipole trap for a variable hold time before splitting. Intensity fluctuations and pointing instabilities of the laser beam as well as inelastic collisions between the molecules [Pet05a] heat the gas and lead to a monotonous temperature increase [Sav97, Wri07]. To demonstrate that the interference results from the condensate, it is sufficient to determine the hold time at which the critical temperature for condensation T_c is reached. Therefore, we fit a Gaussian profile to the density distribution of the cloud, which is recorded after expansion for $t_{\text{TOF}} = 5$ ms from the single-well trap. We find that the integrated residual of the fit gives a good measure whether the cloud shape deviates from a thermal one. The inset in Fig. 2.5 shows that the integrated residual goes to zero after a hold time slightly below 3 s, which locates the phase transition.

The visibility data in Fig. 2.5 are recorded at $B = 700$ G after $t_{\text{TOF}} = 14$ ms². The visibility decreases as the temperature increases and vanishes for a hold time that coincides with the hold time when T_c is reached. The observed decrease of visibility is continuous because we image the full column density including the growing thermal fraction, which does not clearly separate from the condensate in expansion at 700 G. Above T_c , the density distribution does no more show any fringes. Still, the fitting routine produces finite mean values because it can output only positive values. But if the measured visibility is not larger than the standard deviation, its distinction from zero is not significant. The vanishing visibility above the critical temperature confirms that, as expected, the interference is established by

²We verify on images after $t_{\text{TOF}} = 0.4$ ms that the clouds are still separated in the double-well potential despite the higher thermal energies.

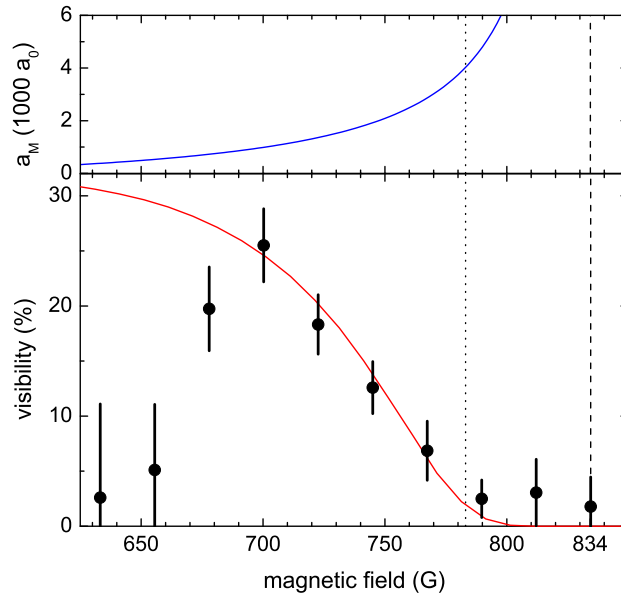


Figure 2.6: Visibility of interference from weak to strong interaction. The upper panel shows how the molecular scattering length a_M increases towards the Feshbach resonance at 834 G, marked by the dashed line. The onset of the strongly interacting regime is marked by the dotted line. In the lower panel, the dots represent the mean visibility with bars indicating the standard deviation resulting from 20 individual measurements. The solid line is the predicted visibility from the simple calculation modeling the non-forward scattering events.

the condensate fraction.

Further intriguing evidence that the interference is caused by the condensate is the observation of interference between independent ultracold clouds. An independent production rules out that the interference can be caused by self interference of particles [Mil05]. To investigate interference between independent clouds, we split them already at a temperature far above the critical temperature to a large distance of $180 \mu\text{m}$ and then create two mBECs independently. Shortly before release, we reduce the distance to obtain the identical geometry as in all the other measurements and proceed as usual. We observe the same kind of interference pattern with a visibility of about 15%. The lower visibility can be explained by a less efficient evaporation and less control over the equal number preparation in the double well.

2.3.3 Dependence of interference visibility on interaction strength

In a further set of measurements, we investigate how the fringe visibility depends on the interaction strength. Therefore we perform the interference experiment for different magnetic field values, thereby changing the molecular scattering length a_M according to the upper

panel of Fig. 2.6³. The observed visibility as a function of the magnetic field is shown in the lower panel in Fig. 2.6. The highest visibility is found at about 700 G. For lower fields, the visibility is decreased, which we attribute to inelastic decay. The inelastic collisions of molecules lead to heating of the gas and loss of particles. The heating reduces the condensate fraction, which decreases the visibility as observed in the previous section. The loss also reduces the signal on the images. This leads to a higher statistical uncertainty in the determination of the visibility, showing up in the larger standard deviations below 700 G.

Towards larger interaction strength, our data show a pronounced decrease of visibility, and the visibility vanishes at about 780 G. This coincides with the onset of strong interaction in the trap, where $1/k_F a \approx 1$. We find that the main effect causing the decrease is elastic non-forward scattering. It is known from experimental and theoretical work on colliding condensates [Chi00, Ban00] that elastic non-forward scattering of particles removes them from the condensate wave function. In contrast to the forward scattering accounted for within the usual mean-field approach, this non-forward scattering transfers particles into momentum states of random direction, which therefore do no more contribute to the observed interference pattern. Non-forward scattering is a particle-like excitation, which requires v_{rel} to exceed the speed of sound v_s . The process is suppressed for smaller v_{rel} [Chi00, Ban01]. To estimate the decrease of visibility through this process, we perform a simple model calculation. The velocity dependence of non-forward scattering is included by the following approximation: no suppression for $v_{\text{rel}} \geq v_s$ and full suppression otherwise. We calculate the mean number of non-forward scattering events N_e for a representative molecule with molecules of the other condensate until the moment of detection. This representative molecule travels along the center-of-mass path of the condensate; see Fig. 2.2(a). We take the bosonically enhanced, unitarity limited scattering cross section $\sigma = 8\pi a_M^2 / (1 + (ka_M)^2)$, with $k = mv_{\text{rel}}/\hbar$. From N_e , we derive the probability for a molecule to still be part of the condensate. This probability is e^{-N_e} and directly corresponds to the expected visibility, which we fit to the data, excluding the three data points below 700 G. We obtain the solid line in Fig. 2.6. The only fit parameter is a normalization factor, which allows us to account for the reduced detected visibility because of the limited imaging resolution. The fit yields a factor of 0.32, which is consistent with the imaging resolution discussed in Sec. 2.2.4. We find that our simple model for non-forward scattering can very well explain the decrease of visibility towards high interaction strength.

There are also other effects that decrease the visibility for increasing interaction strength, but they turn out to be minor for our experimental conditions: Strong interaction lead to a depletion of the condensate [Dal99]. Only the condensate contributes to the interference pattern and not the depleted fraction. The depleted fraction amounts to about 10% at 780 G. As we expect the reduction of visibility to be proportional to the depletion, the reduction is negligible (at 780 G from 2.6% to 2.3%). Another effect reducing the visibility is the collisional dissociation of molecules during overlap. However, this effect can only occur above 800 G, where the collision energy exceeds the binding energy.

To directly demonstrate the effect of non-forward scattering, we study the collision of two condensates when their relative velocity v_{rel} is much faster than the their expansion velocity.

³We verify on images after $t_{\text{TOF}} = 0.4$ ms that the clouds are still separated in the double-well potential despite the higher chemical potential at higher interaction strength.

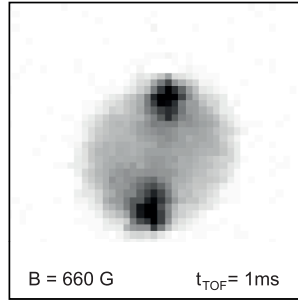


Figure 2.7: Absorption image 1 ms after the collision of two BECs. A spherical shell of scattered particles clearly separates from the two BECs. The field of view is $180 \times 180 \mu\text{m}$.

This allows us to observe the non-forward scattered particles in an s -wave shell [Bug04], well separated from the condensates, see Figure 2.7. This separation was not present in the interference experiments reported before because v_{rel} was similar to the expansion velocity. We apply our simple model to calculate the fraction of non-forward scattered particles and find good agreement, confirming our model in an independent and direct way.

Close to the Feshbach resonance, we enter a regime where the number of collisions becomes large. This leads to hydrodynamic behavior also above T_c [O’H02a, Wri07]. The time of flight series in Fig. 2.8, taken on resonance, shows that the clouds do not penetrate each other in this regime. Instead, the flow of the particles is redirected into the the x - z -plane leading to the observed high column density in the center. Unlike at low magnetic fields, the clouds do not superimpose. This directly excludes interference of two independent condensates in the strongly interacting regime. The scenario is similar to the one in Ref. [Jos11] and may be described by the analysis therein.

The hindered overlap could be overcome by a magnetic field ramp to weak interaction after release and before overlapping, as done for the detection of vortices in Ref. [Zwi05]. Like the observation of vortices, the observation of interference would evidence the coherence of the strongly interacting superfluids.

In further measurements, performed above the Feshbach resonance towards the BCS regime, we did not observe interference. To discuss possible reasons for the absence of interference fringes, let us first consider the effect of non-forward scattering on the visibility. As on the BEC side, this effect may hinder overlap and interference for $1/k_F a < -1$, i.e. below 910 G. However, we also have to consider that the pairs on the BCS side may not persist in expansion [Sch07], unlike on resonance or on the BEC side. For the lowest achievable temperature in our experiment and at 910 G, the pairs would be already unstable after a very short expansion time according to Ref. [Sch07].

2.4 Conclusion and outlook

In conclusion, we have observed the interference between two molecular BECs. The interference pattern visualizes the standing matter wave of the weakly bound Feshbach molecules

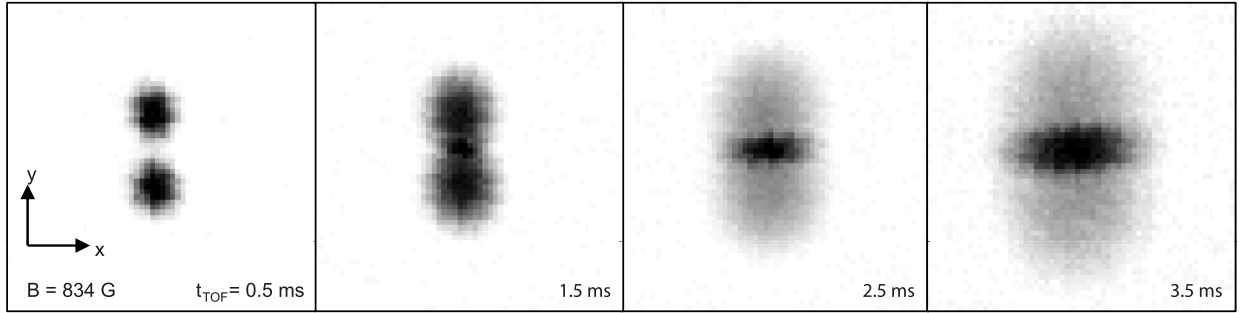


Figure 2.8: The hindered overlap on resonance. The series shows the first few milliseconds of expansion. The two clouds do not penetrate each other, but splash according to hydrodynamics. The field of view is $180 \times 180 \mu\text{m}$.

and shows coherence over the spatial extension of the cloud. The contrast of interference vanishes above the critical temperature of condensation, demonstrating that the interference is established by the condensed molecules only. We find that non-forward elastic scattering processes can lead to a depletion of the condensate wave function while the clouds overlap. This effect increases towards higher interaction strength and prevents us from observing interference in the strongly interacting regime. On resonance we observe that the two clouds do not overlap but rather collide and deform as a result of deep hydrodynamic behavior.

Interference between condensates of paired fermionic atoms can serve as a powerful tool to investigate many exciting aspects of those systems. A future application will be given, for example, if p -wave condensates become available. Here, interference is predicted to reveal the vector nature of the order parameter [Zha07]. A conceptually interesting regime will be entered when the size of the pairs becomes comparable to the fringe period. Then the detected distribution of atoms may not reveal the interference pattern of the pair distribution. Besides investigating condensates of paired fermions themselves, the system could be used to study the fundamental processes of interference. The wide tunability of the interaction strength could be used to assist self-interference [Ced07] or to investigate to which extent interaction build up the observable relative phase [Xio06].

Suppressing the effect of non-forward scattering during overlap could extend the range of applications of condensate interference. Such a suppression may be achieved by reducing the interaction strength before overlap using fast magnetic field ramping techniques [Gre03, Zwi05]. This technique would allow for investigating the interference in the regime of strong interaction or even on the BCS side of the resonance, where the interference of Cooper-type pairs is an intriguing question in itself.

Acknowledgments

We thank Christopher Gaul for stimulating discussions. We acknowledge support by the Austrian Science Fund (FWF) within SFB 15 (project part 21) and SFB 40 (project part 4).

Chapter 3

Publication: Higher-nodal collective modes in a resonantly interacting Fermi gas[†]

accepted for publication in PRA (2013)

Edmundo R. Sánchez Guajardo, Meng Khoon Tey, Leonid A. Sidorenkov,
and Rudolf Grimm

*Institut für Quantenoptik und Quanteninformation (IQOQI), Österreichische Akademie der Wissenschaften
and Institut für Experimentalphysik, Universität Innsbruck, 6020 Innsbruck, Austria*

We report on experimental investigations of longitudinal collective oscillations in a highly elongated, harmonically trapped two-component Fermi gas with resonantly tuned s -wave interactions (‘unitary Fermi gas’). We focus on higher-nodal axial modes, which in contrast to the elementary modes have received little attention so far. We show how these modes can be efficiently excited using a resonant local excitation scheme and sensitively analyzed by a Fourier transformation of the detected time evolution of the axial density profile. We study the temperature dependence of the mode frequencies across the superfluid phase transition. The behavior is qualitatively different from the elementary modes, where the mode frequencies are independent of the temperature as long as the gas stays in the hydrodynamic regime. Our results are compared to theoretical predictions based on Landau’s two-fluid theory and available experimental knowledge of the equation of state. The comparison shows excellent agreement and thus both represents a sensitive test for the validity of the theoretical approach and provides an independent test of the equation of state. The present results obtained on modes of first-sound character represent benchmarks for the observation of second-sound propagation and corresponding oscillation modes.

[†]The author of the present thesis performed the measurements and data analysis, together with E.R.S.G. and M.K.T., under the supervision of R.G.

3.1 Introduction

In ultracold quantum gases, measurements on collective oscillations are well established as powerful tools to study the many-body properties of the system [Pit03, Pet02]. Experiments on collective modes reveal the dynamics in the different regimes of superfluid, collisionally hydrodynamic, and collisionless behavior. The eigenfrequencies can be determined very accurately, which allows to extract valuable information on the equation of state (EOS), with great sensitivity to subtle interaction effects in the strongly interacting regime.

In ultracold Fermi gases [Ing08, Gio08, Blo08], collective modes have been widely applied to study the crossover from Bose-Einstein condensation (BEC) to a Bardeen-Cooper-Schrieffer (BCS) type superfluid. A situation of particular interest is the two-component Fermi gas with resonant interactions, with an s -wave scattering length tuned to infinity by means of a Feshbach resonance [Chi10]. This special case, which lies right in the center of the BEC-BCS crossover, has attracted a great deal of interest, mainly attributed to its universal properties. The resonantly interacting Fermi gas is characterized by strong interaction effects in the EOS [Kin05b, Hor10, Nas10, Ku12] and reveals a unique universal thermodynamic behavior [Ho04].

So far, experiments on collective modes in harmonically trapped Fermi gases have been restricted to a few elementary modes. The most simple modes, sloshing modes, do not provide any information on the properties of the quantum gas, and their main application is thus to accurately determine the trap frequencies. Surface modes are insensitive to the EOS, but they allow to clearly distinguish between hydrodynamic and collisionless behavior [Alt07c, Wri07] and they have been used to detect the angular momentum in a rotating Fermi gas [Rie09, Rie11]. Elementary compression modes of axial [Bar04a, Nas09] and radial [Bar04a, Kin04a, Kin04b, Kin05a, Alt07b, Rie08] character have been very widely studied in the field. Such modes do not only probe the particular collision regime, but they also give access to the compressibility of the gas. However, for a unitary Fermi gas, the eigenfrequencies of the simple compression modes do not show any variation across the superfluid phase transition as the temperature is varied [Kin05a, Rie08]. This can be understood as a consequence of the fact that superfluid and collisional hydrodynamics both lead to the same frequencies. A rigorous proof for this temperature-independence can be given in terms of an exact scaling solution of the hydrodynamic equations of motion [Hou13a]. The situation is strikingly different for higher-nodal modes. Here the frequencies vary across the superfluid phase transition, when the dynamical regime changes from superfluid to collisional hydrodynamics [Tey13, Hou13b]. Such higher-nodal modes therefore represent an interesting addition to the experimental tool-box for probing strongly interacting Fermi gases.

We have recently carried out a series of experiments on higher-nodal axial modes in the geometry of a highly elongated trapping potential. First results on the temperature dependence have already been presented in Ref. [Tey13], and the general theoretical framework is described in Ref. [Hou13b]. In this Article, we briefly summarize the main theoretical predictions (Sec. 3.2), we describe the experimental procedures in more detail (Sec. 3.3), and we present the whole set of our experimental results obtained for two different higher-nodal modes (Sec. 3.4). While we here restrict our attention to modes of first-sound character, we note that the results are important as benchmarks for the observation of second-sound

propagation [Sid13] and in view of future experiments on second-sound modes (Sec. 3.5).

3.2 Theoretical predictions

Higher-nodal collective modes in Fermi gases have been theoretically studied based on Landau's two-fluid equations for an isotropic harmonic trapping geometry [He07, Tay09]. For real experiments, however, the situation of highly elongated harmonic traps is more relevant. In this geometry, the description can be reduced to a set of effectively 1D hydrodynamic equations, which only depend on the axial coordinate z . This simplification leads to a powerful approach to describe sound propagation and collective modes in experimentally realistic situation. The basic approach was introduced in Ref. [Ber10] for a cylindrical trap geometry with tight radial confinement. Reference [Hou13b] presents a generalization to the situation of additional weak axial confinement, which readily describes the commonly used geometry of a highly elongated trap containing a 'cigar-shaped' atomic sample. Here, we summarize the main elements of this theoretical approach and the corresponding predictions for higher-nodal modes of first-sound character.

The two basic assumptions underlying the 1D hydrodynamic approach are thermal equilibrium in the radial direction and a flow field that is independent of the radial position. This corresponds to conditions of sufficient heat conductivity and sufficient shear viscosity, which are readily satisfied for resonantly interacting Fermi gases under common trapping conditions. Applying the local density approximation, one can describe the thermodynamics and the flow properties of the trapped sample using effective 1D quantities, which are derived by integrating over the transverse degrees of freedom, such that a thermodynamic quantity q yields a 1D counterpart $q_1 = 2\pi \int_0^\infty q r dr$.

For a first-sound collective mode with frequency ω , the local flow speed can be expressed as $v(z, t) = v_z(z)e^{-i\omega t}$, where the z -dependent amplitude $v_z(z)$ represents the spatial oscillation of the flow velocity. The hydrodynamic equation that describes $v_z(z)$ takes the form [Hou13b]

$$m(\omega^2 - \omega_z^2)v_z - \frac{7}{5}m\omega_z^2 z \partial_z v_z + \frac{7}{5} \frac{P_1}{n_1} \partial_z^2 v_z = 0. \quad (3.1)$$

Here, ω_z represents the trap frequency along the axial direction, m is the atomic mass, P_1 is the '1D pressure' (having units of force), and n_1 is the linear number density. The equation is valid for small-amplitude oscillations, which can be treated as perturbations by linearizing Landau's equations.

At zero temperature and in the classical limit of high temperature the hydrodynamic equation (4.1) admits analytic solutions of polynomial form $v_z = a_k z^k + a_{k-2} z^{k-2} + \dots$, with integer values of k . At $T = 0$, where $P_1(n_1)/n_1 = (2/7)[\mu_0 - (1/2)m\omega_z^2 z^2]$, with μ_0 being the chemical potential at the center of the trap, the frequency of the k -th mode is given by

$$\omega^2 = \frac{1}{5}(k+1)(k+5)\omega_z^2. \quad (3.2)$$

In the classical limit, where $P_1/n_1 = k_B T$, one finds the different k -dependence

$$\omega^2 = \frac{1}{5}(7k+5)\omega_z^2. \quad (3.3)$$

We point out that Eqs. (4.2) and (4.3) give the same values for $k = 0$ (center of mass oscillation) and $k = 1$ (lowest axial breathing mode). In fact, one can prove that the frequencies of these two lowest modes are temperature independent for the resonantly interacting gas (unitary Fermi gas), corresponding to an exact scaling solution of the two-fluid hydrodynamic equation [Hou13a]. On contrary, the frequencies of the $k \geq 2$ modes vary with temperature.

We now focus on the modes with $k = 2$ and $k = 3$, which are experimentally most relevant. Using a variational approach [Tay08], one can obtain their eigenfrequencies at finite temperatures as

$$\omega_{k=2}^2 = \frac{129t_2 - 25}{5(9t_2 - 5)}\omega_z^2, \quad (3.4)$$

and

$$\omega_{k=3}^2 = \frac{440t_3 - 252}{5(25t_3 - 21)}\omega_z^2. \quad (3.5)$$

In these equations $t_2 = M_0M_4/M_2^2$ and $t_3 = M_2M_6/M_4^2$, where we have introduced the dimensionless moments

$$M_\ell = \int_{-\infty}^{\beta\mu_0} dx (\beta\mu_0 - x)^{(\ell+1)/2} f_n(x). \quad (3.6)$$

Here, the phase-space density $f_n(x)$ is a universal function [Ho04] defined by $f_n(x) = n\lambda_T^3$, where n is the 3D number density and $\lambda_T = h/(2\pi mk_B T)^{1/2}$ is the thermal deBroglie wavelength. The dimensionless parameter $x = \beta\mu$, with $\beta = 1/k_B T$ and μ being the chemical potential, is related uniquely to T/T_F . The universal function $f_n(x)$ can be determined from the recent EOS measurements [Kin05b, Hor10, Nas10, Ku12]. In this work, we make use of the latest results from [Ku12].

One can also show that the velocity fields for the $k = 2$ and $k = 3$ modes take the form

$$v_z^{k=2}(z) \propto \frac{3m\omega_z^2\beta}{2} \frac{M_0(x_0)}{M_2(x_0)} z^2 - 1, \quad (3.7)$$

and

$$v_z^{k=3}(z) \propto \frac{5m\omega_z^2\beta}{6} \frac{M_2(x_0)}{M_4(x_0)} z^3 - z. \quad (3.8)$$

Here, the parameter $x_0 = \beta\mu_0$ is the value of x at the center of the trap. Finally, using the equation of continuity under the 1D formulation $\partial_t n_1 + \partial_z(n_1 v_z) = 0$, one can calculate the shape of the density oscillations for each mode.

3.3 Experimental procedures

3.3.1 Sample preparation

The starting point of our experiment is an ultracold, resonantly interacting Fermi gas in an elongated optical dipole trap. This gas is prepared by evaporating a balanced mixture of fermionic ${}^6\text{Li}$ atoms in their two lowest spin states at a magnetic field of 834 G, very close to

the center of the well-known broad Feshbach resonance [Chi10]¹. The atomic cloud contains typically $N/2 = 1.5 \times 10^5$ atoms per spin state. For the lowest temperatures, the waist of the trapping beam (wavelength 1075 nm) is 31 μm , the trap depth is about 2 μK , and the axial and radial trap frequencies are $\omega_z = 2\pi \times 22.52(2)$ Hz and $\omega_r = 2\pi \times 473(2)$ Hz, respectively. For experiments at higher temperatures, the beam waist is increased to 38 μm , and deeper traps are used (up to 16 μK depth) with trap frequencies of up to $\omega_z = 2\pi \times 23.31(3)$ Hz and $\omega_r = 2\pi \times 1226(6)$ Hz. The corresponding Fermi temperatures $T_F = \hbar(3N\omega_r^2\omega_z)^{1/3}/k_B$ vary between about 0.8 and 1.5 μK .

To achieve the lowest possible temperatures, we perform deep evaporative cooling up to the point where the trapping potential cuts slightly into the Fermi sea, indicated by the onset of spilling losses in the last stage of the evaporation. After that, the gas is adiabatically recompressed by increasing the trapping beam's power to the extent where the trap depth becomes at least twice more than the Fermi energy $k_B T_F$. This recompression step is essential to ensure negligible anharmonicities in the radial confinement. The essentially perfect harmonic confinement along the axial direction is ensured by the magnetic trapping that results from the curvature of the magnetic field used for Feshbach tuning [Joc03b].

We vary the temperature T of the gas by controlled heating, always starting from a deeply cooled cloud ($T/T_F \approx 0.1$). In the low-temperature range ($T \lesssim 0.2 T_F$), we simply introduce a variable hold time of up to 4 s in which residual trap heating slowly increases the cloud's temperature. For the higher-temperature range ($0.2 T_F < T < 0.5 T_F$), we heat the sample using parametric heating, modulating the trap power at about $2\omega_r$, and introducing a sufficient hold time to reach thermal equilibrium between the different degrees of freedom. We note that we use deeper traps for samples with higher T/T_F , because plain evaporation puts a limit on the maximum attainable temperature of the gas.

3.3.2 Thermometry

We determine the temperature T of the gas by analyzing its density distribution in the trap, based on knowledge of the EOS. Under the local density approximation, one can readily show for a harmonic trap that the 1D density profile $n_1(z)$ is given by [Nas10, Ho10]

$$n_1(z) = \frac{2\pi}{m\omega_r^2} \frac{k_B T}{\lambda_T^3} f_p(x_0 - \frac{1}{2}\beta m\omega_z^2 z^2). \quad (3.9)$$

Here, the universal function $f_p(x)$ is related to the universal function $f_n(x)$ introduced in Sec. 3.2 by $f_p(x) = \int_{-\infty}^x f_n(y) dy$, and is therefore also known from a given EOS. The parameter x_0 is the value of x at the center of the trap.

In the ideal case where one is able to obtain an accurate *in-situ* measurement of $n_1(z)$ by imaging the trapped cloud, it is straightforward to retrieve the parameters T and x_0 by fitting $n_1(z)$ using Eq. (3.9). However, in reality we have to deal with imperfections of our absorption imaging scheme. To extract the temperature in an accurate way, we have adopted the methods described in detail in the Appendix.

¹A very recent measurement [Zür13] pinpoints the pole of the resonance to 832.2 G. Our measurements were performed at 834 G, corresponding to the previous state of knowledge on the resonance position [Bar05b]. The difference, however, is less than 1% of the resonance width and therefore has negligible effect on the present measurements.

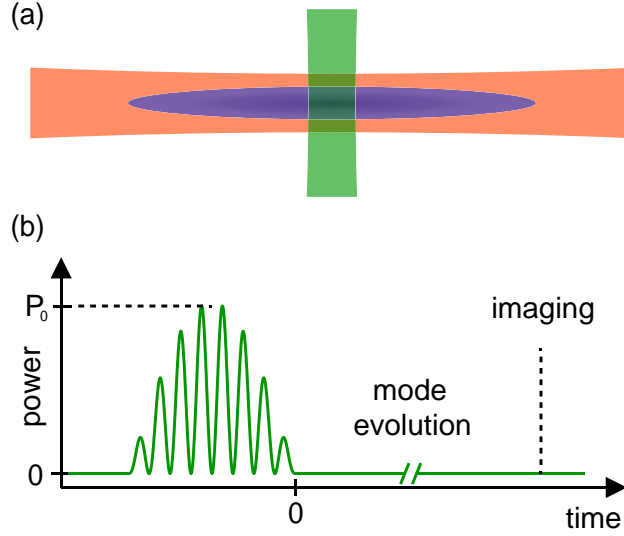


Figure 3.1: (Color online) Experimental scheme to excite higher-nodal first-sound longitudinal modes. In (a), we illustrate the basic geometry of exciting the optically trapped cloud with a weak, power-modulated repulsive laser beam, which perpendicularly intersects the trapping beam. In (b), we show the power modulation of the repulsive beam for the excitation.

3.3.3 Exciting and observing higher-nodal collective modes

We apply a resonant excitation scheme to create a collective oscillation. Figure 3.1(a) illustrates the basic geometry of our scheme, in which a repulsive 532-nm green laser beam perpendicularly intercepts the trapping beam. The laser beam configuration is similar to the classical scheme for the excitation of sound waves in quantum gases [And97a, Jos07]. To excite a mode, we position the green beam near the antinode of the mode and modulate its power at the expected frequency of the mode. The amplitude, duration and shape of the modulation are carefully adjusted in order not to overdrive the excitation while maintaining sufficient signal-to-noise ratio. We adopt an excitation pulse that contains 8 cycles of sinusoidal modulation with a half-cycle sine envelope², see illustration in Fig. 3.1(b). We set the maximum barrier height of the green beam to about $0.01 k_B T_F$. Depending on the order of the mode to be excited, this is realized with beam waists ranging from $30 \mu\text{m}$ to $70 \mu\text{m}$ and values of the maximum power P_0 between $400 \mu\text{W}$ and 3mW . The 8-cycle pulse is chosen such that the resulting total excitation duration is not too long as compared to the damping time of the highest-nodal mode that we can observe. The smooth half-cycle sine envelope reduces the Fourier width and avoids side lobes in the spectrum, thereby suppressing the excitation of unwanted modes. For an efficient excitation of a given mode, we find that the width of the green beam should well match the local mode profile at the selected antinode, while the excitation frequency should be within 1% of the actual mode frequency.

²The power of the green beam is given by $P(t) = P_0 \sin(\omega_m t/16)[1 - \cos(\omega_m t)]$ for $0 < t < 16\pi/\omega_m$, and zero otherwise. The parameter ω_m is the modulation frequency and P_0 represents the peak power.

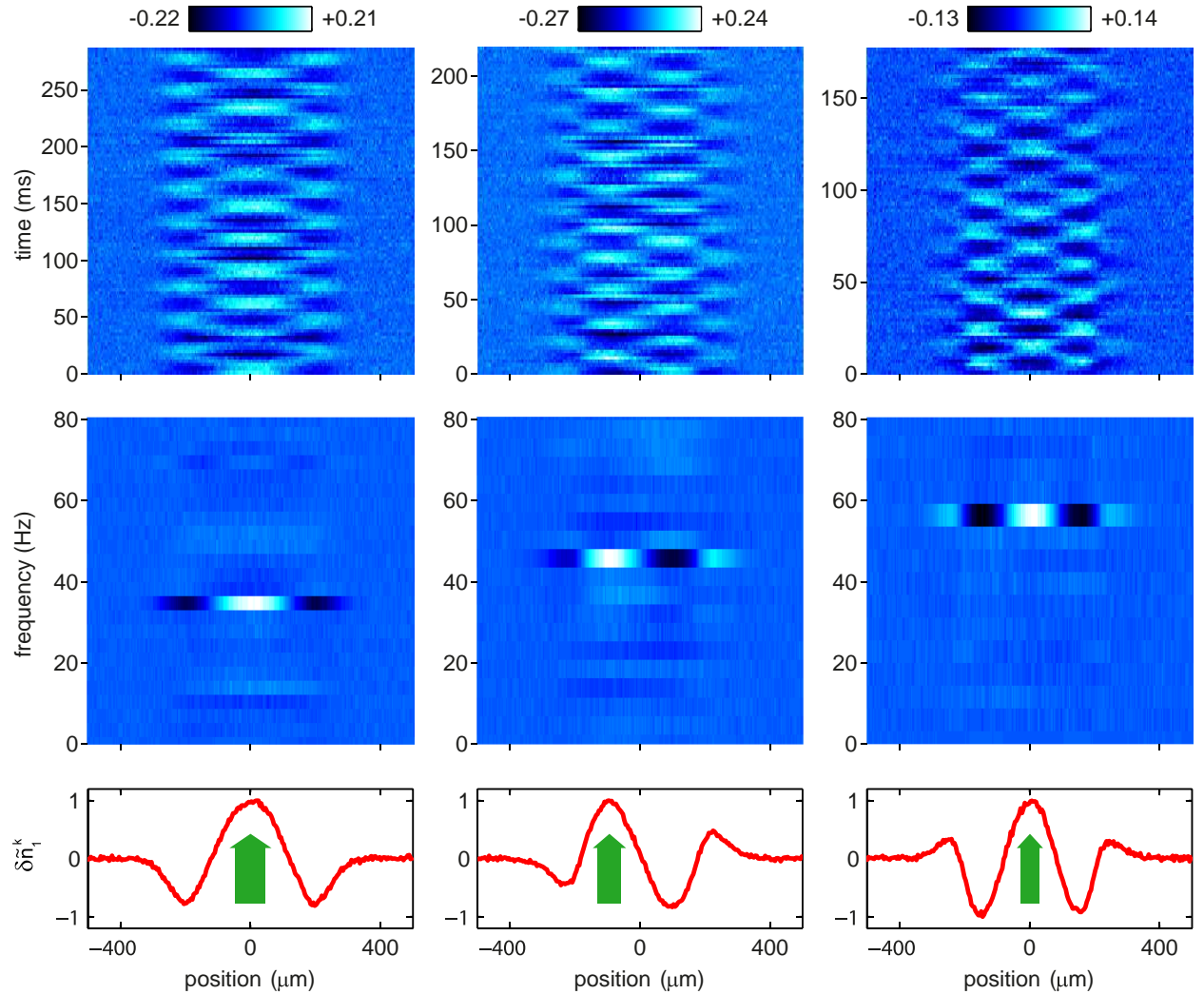


Figure 3.2: (Color online) Observed collective modes in the time domain and in frequency space versus axial position. The three columns refer to the mode orders $k = 1, 2$, and 3 . We show the normalized density variation signals $\delta n_1(z, t)/\bar{n}_1(0)$ (top row), their Fourier transforms $\delta \tilde{n}_1(z, \omega)$ (middle row), and the mode profiles $\delta \tilde{n}_1^k$ (bottom row). The measurements were taken for our coldest samples with $T/T_F \approx 0.1$. The arrows in the bottom panel show the positions of the repulsive excitation beam for each mode. Note that for efficient excitation we adjust the width of the excitation beam to match the local profile at the chosen antinode. While, for $k = 1$ and 3 , the beam is centered and addresses the central antinode, the beam is spatially offset for the $k = 2$ mode.

Once a collective mode is excited, we record the axial density profiles $n_1(z, t)$ of the gas for a variable time delay t after the excitation pulse, where $n_1(z, t)$ is the number density integrated over the transverse degrees of freedom. These profiles are obtained with a probe beam that perpendicularly intercepts the trapping beam, and are taken $600 \mu\text{s}$ after suddenly releasing the atoms from the optical trap³. To enhance the visibility, we subtract a background profile $\bar{n}_1(z)$ obtained from averaging the profiles over all measured delay times. This gives a differential density variation function $\delta n_1(z, t) = n_1(z, t) - \bar{n}_1(z)$, which is finally normalized to the maximum linear density $\bar{n}_1(0)$ at the trap center. In the top panel of Fig. 3.2, we show examples of this signal for the $k = 1, 2,$ and 3 modes for the coldest samples with $T/T_F \approx 0.1$. One can see that the adjacent antinodes always oscillate in opposite directions, similar to standing waves on a guitar string.

3.3.4 Analyzing the eigenmodes: Extracting mode profiles, frequencies, and damping rates

The first step to analyze the observed time-dependent profiles $\delta n_1(z, t)$ is a Fourier transform, yielding a representation of our data in frequency space, $\delta \tilde{n}_1(z, \omega)$ ⁴. For this purpose we employ a fast Fourier transform (FFT) algorithm. Corresponding results are shown in the middle panel of Fig. 3.2, as calculated for each time-dependent oscillation profile in the top panel. The discrete nature in frequency space becomes evident, with very little noise in the background.

It is straightforward to extract the mode profiles $\delta \tilde{n}_1^k(z)$ from the FFT results by setting $\delta \tilde{n}_1^k(z) = \delta \tilde{n}_1(z, \omega_k)$, where ω_k is the eigenfrequency of the k^{th} mode. The corresponding mode profiles for the $k = 1, 2,$ and 3 modes are shown in the bottom panel of Fig. 3.2. Experimentally, we make use of the mode profiles and the frequencies obtained in this way to optimize the beam waist and the modulation frequency in our excitation scheme. We proceed iteratively, which eventually allows for an optimum excitation of a single mode.

To extract the mode frequencies more precisely than it is possible by simply analyzing the peaks in the corresponding Fourier spectrum, we adopt the following algorithm. We project $\delta n_1(z, t)$ onto the mode profile $\delta \tilde{n}_1^k(z)$ to obtain a mode amplitude function $A(t) = \int_{-\infty}^{\infty} \delta n_1(z, t) \delta \tilde{n}_1^k(z) dz$. Then we fit a simple damped harmonic oscillation to $A(t)$ to obtain the frequency and the damping time of the mode. This projection procedure is analogous to the projection of a superposition wavefunction onto one of the orthogonal eigenstates of a quantum system. It greatly enhances the signal-to-noise ratio and results in very low statistical uncertainties for the mode frequencies, with relative uncertainties as low as in the range of a few permille.

In Fig. 3.3, we show examples of $A(t)$ for the $k = 1, 2,$ and 3 modes obtained from

³The images are recorded after a short time of flight of $600 \mu\text{s}$. The small radial expansion avoids very large optical densities and thus allows for a more accurate determination of the atom number. The effect on the one-dimensional (doublyintegrated) axial density profile remains negligibly small, since the hydrodynamic expansion of a cigar-shaped cloud proceeds mostly in the radial direction.

⁴FFT gives a complex spectrum, $\delta n(z, \omega) = \text{Re}[\delta n(z, \omega)] + i \text{Im}[\delta n(z, \omega)]$. By multiplying a suitable phase factor to $\delta n(z, \omega)$, we can transfer all information pertaining to a particular mode into one quadrature, obtaining $\delta \tilde{n}(z, \omega)$.

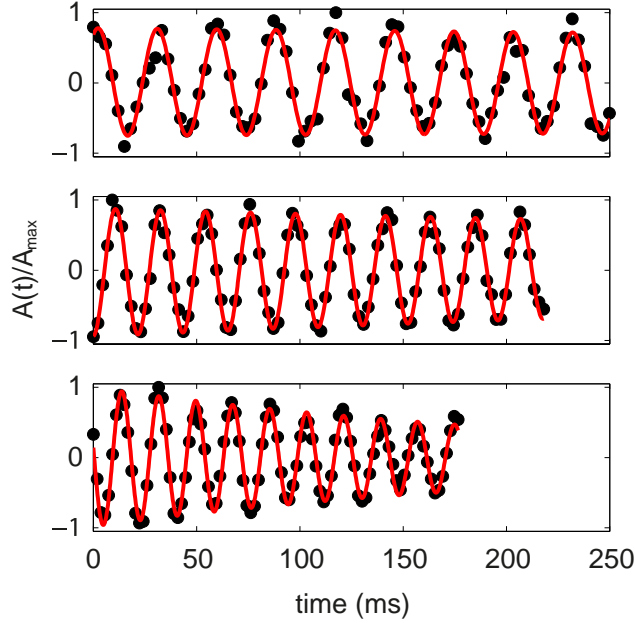


Figure 3.3: (Color online) Evolution of the $k = 1$ (top), $k = 2$ (middle) and $k = 3$ (bottom) mode amplitudes at $T/T_F \approx 0.1$. The black circles represent the experimental data for $A(t)$ normalized to the maximum value A_{\max} of $|A(t)|$. The red solid lines are the fits to the data based on simple damped harmonic oscillations.

samples with $T/T_F \approx 0.1$. For the $k = 1$ compression mode (upper panel), the observed behavior does not show any damping. Even data taken after a much longer delay time of 3 s (not shown) do not reveal any significant damping. In contrast, the higher-nodal modes show clear damping. At the lowest temperatures, the $1/e$ damping time for the $k = 2$ mode (middle panel) is about 1.5 s, and that for the $k = 3$ mode (lower panel) is about 0.3 s.

We finally note that we have not succeeded in observing modes with $k \geq 4$, despite of considerable efforts. We believe that this is due to a fast increase of damping with the mode order, which is clearly indicated by our data for the $k = 1, 2, 3$ modes. Large damping affects both our resonant excitation scheme and the detection of the mode by means of a Fourier transform, which may explain a huge difference between the observed mode with $k = 3$ and the unobserved mode with $k = 4$.

3.3.5 Checking for systematic errors

The real experiment is an approximation to the ideal scenario of a small-amplitude oscillation in a perfectly harmonic trap, as described in the theoretical approach in Sec. 3.2. Here we investigate in how far our data are influenced by anharmonicities of the trapping potential and nonlinear effects arising from the finite amplitude of the mode, and we identify the conditions that ensure a reliable comparison between the measurements and the theoretical predictions.

The axial compression mode ($k = 1$) serves us as a benchmark to rule out a significant effect of anharmonicities. This mode has been studied extensively before [Bar04a, Nas09]

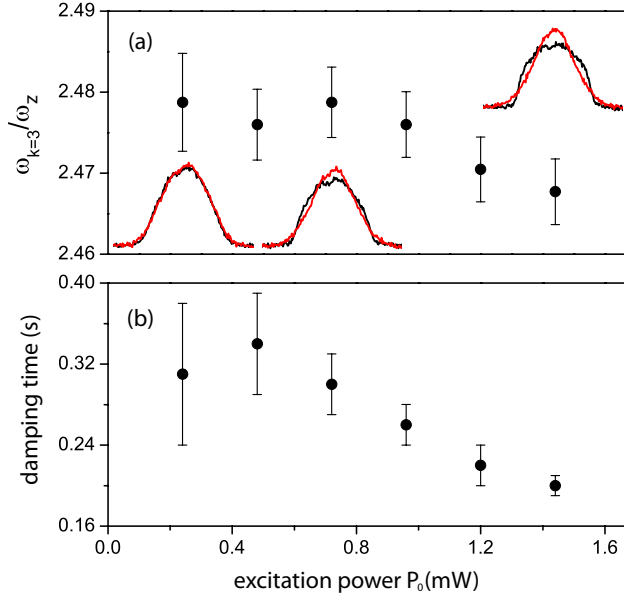


Figure 3.4: (Color online) The normalized oscillation frequency (a) and $1/e$ damping time (b) of the $k = 3$ mode versus the power P_0 of the green excitation beam. The three insets in (a) show the axial density profiles of the atom cloud at the turning points of the mode oscillation for three different excitation powers. The error bars denote the standard errors obtained from fitting $A(t)$.

and, in the unitarity limit, its frequency is temperature independent as long as the gas remains hydrodynamic [Hou13a]. Only for very shallow traps, we observe a $k = 1$ mode frequency that is lower than expected. We find that trap depths of twice the non-interacting Fermi energy are sufficient to observe a frequency very close to the ideal value of $\omega_{k=1} = \sqrt{12/5}\omega_z$ throughout the full temperature range explored in the present work. Deviations from this value remain below 0.3% and no significant temperature dependence is observed.

We checked for a possible nonlinear behavior by deliberately overdriving the collective modes. We measured the frequency and damping time of each collective mode versus the power of the excitation beam. Figure 3.4 shows the results of such a measurement for the $k = 3$ mode for the coldest samples used in our work. The measurements show that the frequency stays constant within the measurement uncertainties up to a power $P_0 \approx 1$ mW. The fact that the spatial profile is already strongly affected (see insets) shows that the mode frequency is rather robust against nonlinearities. The mode damping time exhibits a similarly robust behavior with a slight trend to be affected already at somewhat smaller excitation amplitudes. The excitation power P_0 is always kept small enough to avoid significant effects on the mode frequencies.

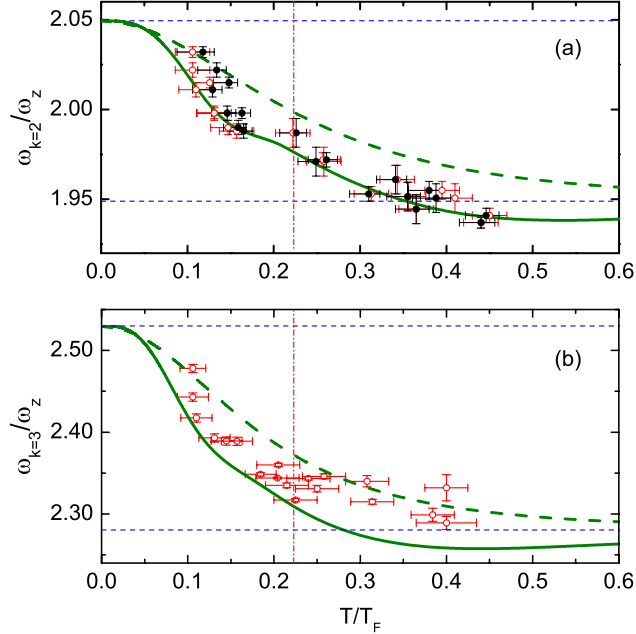


Figure 3.5: (Color online) Comparison between experimental and theoretical first-sound frequencies for (a) the $k = 2$ and (b) the $k = 3$ mode. In (a), the reduced temperature T/T_F is obtained by the two different methods described in the Appendix in Secs. 3.6.2 (open red symbols) and 3.6.3 (filled black symbols). In (b), T/T_F is extracted by only using the first method. The theoretical curves (solid lines) are obtained with Eqs. (3.4) and (3.5) using the EOS of Ref. [Ku12]. For comparison, we also show the mode frequencies (dashed curves) that would result from the same equations but using the EOS of the ideal Fermi gas. In both panels, the upper and lower thin horizontal dashed lines mark the zero- T superfluid limits and the classical hydrodynamic limits whose values are given by Eqs. (4.2) and (4.3), respectively. The dash-dot vertical lines in (a) and (b) indicate the critical temperature $T_c/T_F = 0.223(15)$.

3.4 Experimental results

Here we present our main experimental results and compare them with the predictions of Sec. 3.2. We consider the two modes with $k = 2$ and $k = 3$ and discuss how their eigenfrequencies and the corresponding mode profiles depend on the temperature. We furthermore present data on the temperature-dependent damping of the two modes.

In Fig. 3.5(a) and (b), we show the measured mode frequencies $\omega_{k=2}$ and $\omega_{k=3}$ versus temperature, normalized to the axial trap frequency ω_z . The two limiting cases of a $T = 0$ superfluid and a classical collisionally hydrodynamic gas are indicated by the upper and the lower horizontal dashed lines in both panels, see Eqs. (4.2) and (4.3). The theoretical predictions according to Eqs. (3.4) and (3.5) and the EOS from Ref. [Ku12] are shown by the solid lines. For comparison, the hypothetical frequencies calculated with the EOS of a non-interacting Fermi gas are shown by the dashed lines. For the $k = 2$ mode we have applied both thermometry methods as described in the Appendix, with the open symbols

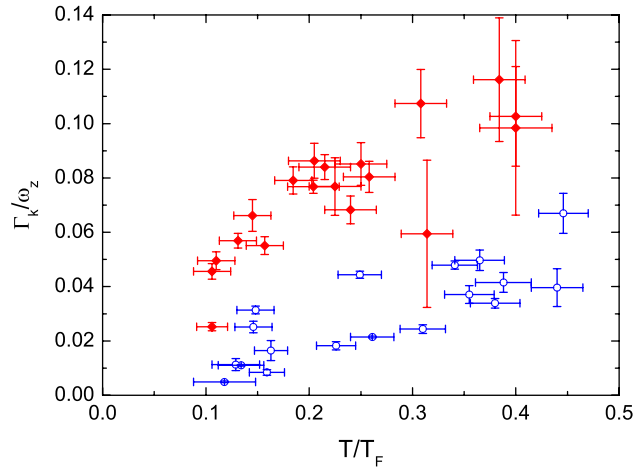


Figure 3.6: (Color online) Measured amplitude damping rates Γ_k of the $k = 2$ (blue open circles) and the $k = 3$ (red filled diamonds) modes versus temperature, normalized to the axial trap frequency ω_z .

representing the results from the wing-fit method (Appendix Sec. 3.6.2) and the filled symbols from the potential-energy method (Appendix Sec. 3.6.3). For the $k = 3$ mode we have applied only the first method.

For the $k = 2$ mode (Fig. 3.5(a)), the measured mode frequencies are in almost perfect agreement with the theoretical predictions based on the EOS from [Ku12]. In comparison, the disagreement with the dependence that would result from the EOS of the ideal Fermi gas highlights the important role of interactions. At the lowest temperature realized in our experiment ($T/T_F \approx 0.1$), the frequency lies close to the $T = 0$ superfluid limit ($\omega_{k=2}/\omega_z = 2.049$), but already shows a significant down-shift amounting to almost 1%. This illustrates the high sensitivity of the mode frequency to finite-temperature effects. At the highest temperatures ($T/T_F \approx 0.45$) our data show a clear trend to go below the asymptotic high-temperature value ($\omega_{k=2}/\omega_z = 1.949$), which corresponds to the classical hydrodynamic case. This nonmonotonic temperature dependence can be understood based on the first-order correction to the EOS resulting from the virial expansion [Liu09] at high temperatures.

For the $k = 3$ mode (Fig. 3.5(b)), the general behavior is very similar to the $k = 2$ mode, with the main difference that the relative frequency change from superfluid to collisional hydrodynamics ($\omega_{k=2}/\omega_z = 2.530$ and 2.280 , respectively) is about two times larger. For temperatures below $0.2 T_F$ we find similarly good agreement as in the $k = 2$ case. However, for higher temperatures there is a significant trend to lie above the predicted frequencies, so that we never observe values below the high-temperature limit. This discrepancy is most likely due to dissipative effects, which manifest themselves in mode damping. Landau's equations used as a basis for describing the collective modes do not contain dissipative terms and can therefore not make any predictions on the damping behavior. We can therefore address the question of damping only from the experimental side.

In Fig. 3.6, we show the normalized damping rates for the amplitudes of the $k = 2$ (blue open circles) and the $k = 3$ (red filled diamonds) modes, measured at various temperatures. The damping rate of the $k = 3$ mode is always several times higher than that of $k = 2$, and

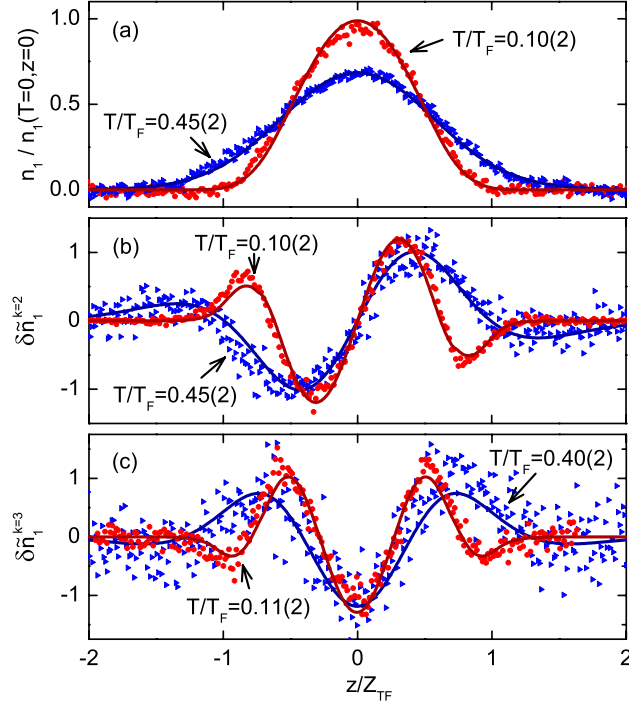


Figure 3.7: (Color online) Comparison of experimental mode profiles (data points) and theoretical predictions (solid lines) for two different temperatures. In (a), we show the cloud profiles obtained with a 2-ms TOF. The solid lines show the density profiles obtained from the EOS [Ku12] with $T/T_F = 0.10$ and 0.45 . In (b), we show the experimental and theoretical $k = 2$ mode profiles at the indicated temperatures. The comparison for the $k = 3$ mode is presented in (c). The z scale is normalized to the Thomas-Fermi radius Z_{TF} of the zero- T interacting gas, which is a factor of $\xi^{1/4} \approx 0.78$ [Ku12] smaller than in the non-interacting case.

it strongly increases as the cloud gets hotter. It is evident that the situation, where we have observed significant deviations in the mode frequencies ($k = 3$ and $T/T_F \gtrsim 0.2$), coincides with the case of highest damping rates (exceeding 10 s^{-1}). It is known that violation of the 1D condition assumed in Sec. 3.2 would result in a damping of the collective oscillation. Therefore, a higher damping rate could naturally be accompanied with a larger deviation from the prediction using the 1D formulation of the Landau's two-fluid model. This supports our interpretation of the observed frequency deviation in terms of dissipative effects.

For an accurate determination of temperature-dependent frequency shifts in our experiment, the $k = 2$ mode turns out to be superior to the $k = 3$ mode. Our results indicate that the advantage of the latter mode to exhibit larger frequency changes is overcompensated by the larger damping, which introduces larger statistical uncertainties (see error bars in Fig. 3.5) and apparently also systematic errors. However, for larger trap aspect ratios than applied in our experiment, the situation may be different and higher modes may provide further interesting information.

In Fig. 4.1(a) and (b), we finally show the observed spatial profiles of the $k = 2$ and $k = 3$ modes, in comparison to the corresponding theoretical predictions. For both modes

we present data sets for the lowest temperature that we could realize ($T/T_F \approx 0.1$) and for the highest temperature explored ($T/T_F \approx 0.45$). In the first case, the situation is deep in the superfluid regime, whereas the second case corresponds to the classical hydrodynamic case. For reference, Fig. 4.1(a) shows the corresponding spatial profiles of the unperturbed cloud, from which we obtained the temperature following the method of Sec. 3.6.3 in the Appendix. The agreement between the experimentally observed mode profiles and the theoretical predictions is remarkable. Within the experimental uncertainties and with the mode amplitude being the only fit parameter, we find a perfect match. This again highlights the validity of the theoretical 1D framework and power of our experimental approach to higher-nodal collective modes.

3.5 Conclusions and Outlook

We have presented an efficient tool-box to excite and detect higher-nodal axial collective modes in a resonantly interacting Fermi gas. Our results (see also [Tey13]) reveal the pronounced temperature dependence below and near the superfluid phase transition, which is theoretically predicted in the framework of a 1D two-fluid hydrodynamic model [Hou13b]. The observed temperature dependence is a unique feature of higher-nodal modes and has not been observed in any other collective mode studied in Fermi gases so far. The excellent agreement of the experimentally observed mode frequencies with the theoretical predictions provides a stringent test for the validity of this 1D approach and provides an independent confirmation of the recently measured EOS [Ku12] of the resonantly interacting Fermi gas.

We have also reported first studies on the mode damping behavior, which show a strong increase of the measured damping rates with the order of the mode investigated. Dedicated experiments on damping could provide valuable information on the viscosity and the thermal conductivity of the strongly interacting Fermi gas, which may provide further insight into fundamental questions related to viscosity [Sch09, Cao11a, Cao11b]. A better understanding of damping would also be important to understand the limitations of the theoretical approach [Hou13b] applied to describe the modes.

Generalizations of our experiments to first-sound collective modes in the BEC-BCS crossover regime [Gio08, Blo08, Chi10] and to spin-polarized Fermi gases [Zwi06b, Par06, Nas09] will be rather straightforward. A very exciting prospect is the extension to second-sound modes [Tay09, Hou13b], where the superfluid and the normal component oscillate in opposite phase. A recent experiment [Sid13] shows the propagation of second-sound pulses along the trap axis, in agreement with a theoretical description based on the same approach that is used in the present work. This observation may, in principle, be interpreted in terms of a superposition of several second-sound modes, but the selective excitation and observation of individual modes of this kind remains an experimental challenge for future experiments.

We would like to acknowledge the strong theoretical support from Yan-Hua Hou, Lev Pitaevskii, and Sandro Stringari. We thank Mark Ku and Martin Zwierlein for fruitful discussions and Florian Schreck for discussion and experimental support. We acknowledge support from the Austrian Science Fund (FWF) within SFB FoQuS (project No. F4004-N16).

3.6 Appendix: Temperature determination

The recorded *in-situ* density profiles $n_1(z)$ are influenced by imperfections in the imaging process. While, under our experimental conditions, the limited resolution and optical aberrations do not play any significant role, we have identified another problem (Sec. 3.6.1) that can considerably affect our thermometry. We here discuss our strategies to circumvent this problem, presenting our two methods (Secs. 3.6.2 and 3.6.3) to extract the temperature from the observed profiles.

3.6.1 Imperfections of absorption imaging

In-situ absorption images and images taken with a short time of flight (TOF) reveal an apparent reduction of the effective absorption cross section, which predominantly occurs in the denser regions of the cloud. To illustrate this effect, we show in Fig. 3.8 how the apparent atom number, i.e. the atom number obtained under the assumption of the full absorption cross section, depends on the TOF after release from the trap for two experimental settings corresponding to a number of $N = 1.2 \times 10^5$ atoms (red diamonds) and 4.8×10^5 atoms (black circles) in the trap. Only after a TOF of 2 ms the apparent atom number reaches a constant maximum value, which corresponds to the true atom number. It is evident that our *in-situ* imaging underestimates the actual atom numbers by about 15% for the data set with $N = 1.2 \times 10^5$, and by about 30% for $N = 4.8 \times 10^5$.

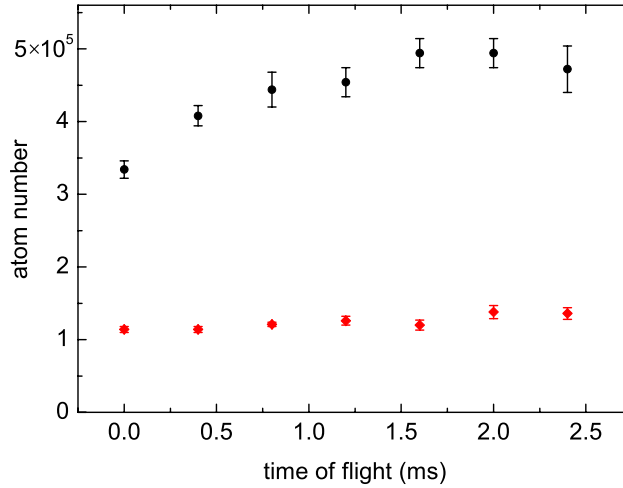


Figure 3.8: (Color online) Apparent atom numbers obtained with different times of flight while keeping other experimental parameters unchanged. The red diamonds and the black circles represent the data sets with $N = 1.2 \times 10^5$ and 4.8×10^5 atoms, respectively.

We do not fully understand the reason for this reduction, which is clearly related to the high density of the cloud, but it is not related to a ‘black out’ effect, in which the imaging light is completely absorbed by a very dense cloud. In our case, the maximum optical density is about one, which can be properly accounted for by the exponential decrease of the transmission with increasing column density. We speculate that the underlying mechanism

is related to multiple scattering of a photon by a few neighboring atoms when the atoms are very closely packed, thereby reducing the effective absorption cross section of the atoms [Cho12]. For our geometry, this effect should be important when the photon's 'mean free path' becomes comparable to the radial size of the cloud, which is indeed the case for our experimental conditions.

By analyzing profiles obtained for different times of flight we found that the imaging problem mainly affects the center of the cloud, where one finds the largest density. Therefore the problem does not only result in smaller apparent atom numbers, but it also distorts the density distribution $n_1(z)$ of the cloud as obtained by *in-situ* absorption imaging. To determine the temperature of the cloud in spite of this problem, we have adopted the two different methods described below. Each method has its own systematic uncertainties. Their accuracies can only be judged *a posteriori* by their mutual agreement and also by their agreement with certain theoretical predictions.

Both methods rely on the accuracy of the total atom number N . We obtain this number through a very careful calibration of the imaging process and the imaging system. For imaging, we typically adopt a 10- μ s-long imaging pulse and keep the probe intensity less than 4% of the saturation intensity. These parameters keep the total number of photon scattering events per atom small, thereby minimizing the photon-recoil-induced Doppler-detuning effect [Hem81, Gri88] on the light ^6Li atoms. We estimate the uncertainty in the resulting atom number to be typically about 10%, in any case below 20%.

3.6.2 Wing-fitting method

In the first method, we obtain the cloud's temperature by fitting Eq. (3.9) to the wings of a 1D density profile taken after a 600 μ s TOF, with N determined independently from a corresponding 2-ms TOF image. The wings, where $n_1(z)$ is relatively small and the total absorption is weak, are essentially free of the image distortion as described above. An example for a typical wing fit is shown in Fig. 3.9. The Figure also illustrates the difference between the true density profile as reconstructed by the wing fit (solid line) and the distorted observed one (data points).

In practice, we adjust the number of data points used for the wing fit until we obtain an atom number very close to the actual value obtained using a sufficiently long TOF. Sometimes, we have to use different numbers of data points in each wing when the profile on the wings is not fully symmetric. This issue is caused mainly by optical aberrations in the imaging system. Nevertheless, we always find the same T/T_F within an uncertainty of 10 to 15% using this procedure for samples prepared by the same experimental sequence. We also do not observe a clear deviation in the so obtained temperature when varying the TOF from 0 to 600 μ s. Our experience shows that the accuracy of T/T_F obtained from this method is not very sensitive to slight distortions in the wing profiles. Instead, it depends more crucially on the correct atom number N .

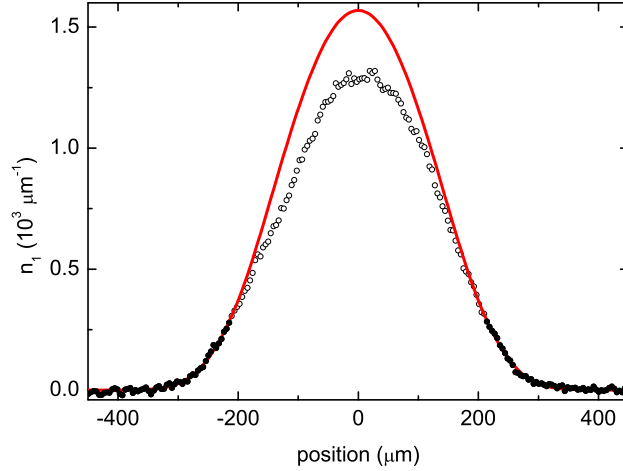


Figure 3.9: (Color online) Typical fit to the wings of the 1D density distribution to determine T/T_F from Eq. (3.9). The filled circles represent the data used for fitting, and the solid line is the full profile according to the fit. The open circles represent the remaining data that were not used in the fit because of the problem to determine the correct linear density in the center of the cloud. Here a TOF of $600 \mu\text{s}$ was applied, the total atom number is $N = 4.2 \times 10^5$, and the temperature is $T/T_F = 0.36$.

3.6.3 Potential-energy method

In the second method, we characterize the temperature in a model-independent way that does not require any *a priori* knowledge of the EOS. Based on the virial theorem [Tho05] we can obtain the total energy E of the harmonically trapped cloud from its potential energy, which can be calculated from the 1D density profile $n_1(z)$ according to $E = 3m\omega_z^2 \int_{-\infty}^{\infty} n_1(z)z^2 dz$. We define a dimensionless parameter E/E_0 , where E is normalized to the energy of a non-interacting, zero-temperature Fermi gas with the same number of atoms, $E_0 = \frac{3}{4}Nk_B T$.

To obtain an accurate value for E/E_0 it is essential to have accurate knowledge of $n_1(z)$. Here we overcome the above-discussed distortion problem by ‘reconstructing’ the correct profile. We measure the density profiles of the cloud for two different times of flight, $600\text{-}\mu\text{s}$ and 2 ms . The corresponding profiles $n_1(z, 600 \mu\text{s})$ and $n_1(z, 2 \text{ ms})$ provide complementary information. While the $600\text{-}\mu\text{s}$ profile provides accurate information on the wings, it underestimates the central part of the cloud. In contrast, the 2-ms profile suffers in the wings from the expansion, but gives accurate information on the central part of the cloud. With an appropriate algorithm to combine this information we can reconstruct the full profile with reasonable accuracy. The reconstructed profile shows approximately the correct atom number and it maintains the wing distribution, which has large weights $\propto z^2$ in the total energy E .

We can now convert E/E_0 into T/T_F using the EOS from Ref. [Ku12]; for a related discussion see Ref. [Cao11b]. Using the universal thermodynamic relations of a resonantly interacting Fermi gas, one can show that E/E_0 is related to the $x_0 = \beta\mu_0$ at the center of

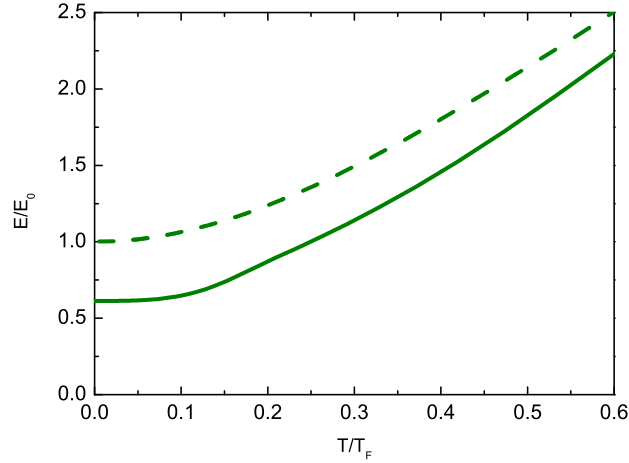


Figure 3.10: (Color online) Relation between E/E_0 and T/T_F for a 3D harmonic trap. The solid and the dashed lines correspond to the results obtained using the EOS from Ref. [Ku12] and the EOS of the non-interacting Fermi gas, respectively.

the trap by

$$\frac{E}{E_0} = \frac{4(2\pi)^{1/2} M_2(x_0)}{3(3\sqrt{2}\pi)^{1/3} M_0^{4/3}(x_0)}, \quad (3.10)$$

while the x_0 is related to T/T_F by

$$\frac{T}{T_F} = \frac{(2\pi)^{1/2}}{[24\sqrt{2}\pi M_0(x_0)]^{1/3}}. \quad (3.11)$$

Figure 3.10 shows the conversion between E/E_0 and T/T_F for a resonantly interacting Fermi gas in comparison with the ideal non-interacting Fermi gases. For the resonantly interacting Fermi gas at $T = 0$, $E/E_0 = \sqrt{\xi}$. Here ξ is the Bertsch parameter, for which Ref. [Ku12] gives the value $\xi = 0.376(4)$. For the ideal Fermi gas at $T = 0$, $E/E_0 = 1$ by definition.

We finally note that we applied both methods to various data sets to check whether they produce consistent results. In general we find satisfying agreement with each other, as the example of the data set in Fig. 3.5(a) shows. At very low temperatures, the wing-fit method shows a trend to give slightly lower values of T (up to $\sim 10\%$) as compared to the potential-energy method. This indicates small systematic uncertainties of our methods.

Chapter 4

Publication: Collective Modes in a Unitary Fermi Gas across the Superfluid Phase Transition[†]

Phys. Rev. Lett **110**, 055303 (2013)

Meng Khoon Tey, Leonid A. Sidorenkov, Edmundo R. Sánchez Guajardo,
and Rudolf Grimm

*Institut für Quantenoptik und Quanteninformation (IQOQI), Österreichische Akademie der Wissenschaften
and Institut für Experimentalphysik und Zentrum für Quantenphysik, Universität Innsbruck, 6020
Innsbruck, Austria*

Mark J. H. Ku, and Martin W. Zwierlein

*MIT-Harvard Center for Ultracold Atoms, Research Laboratory of Electronics,
and Department of Physics, Massachusetts Institute of Technology, Cambridge, Massachusetts 02139, USA*

Yan-Hua Hou,¹ Lev Pitaevskii,^{1,2} and Sandro Stringari¹

¹*Dipartimento di Fisica, Università di Trento and INO-CNR BEC Center, I-38123 Povo, Italy*

²*Kapitza Institute for Physical Problems RAS, Kosygina 2, 119334 Moscow, Russia*

[†]The author of the present thesis performed the measurements, together with M.K.T. and E.R.S.G., under the supervision of R.G. The data analysis was carried out by M.K.T. and the author. Theoretical support was provided by Y.-H.H, L.P. and S.S. The data on equation of state were provided by M.J.H.K. and M.W.Z.

We provide a joint theoretical and experimental investigation of the temperature dependence of the collective oscillations of first sound nature exhibited by a highly elongated harmonically trapped Fermi gas at unitarity, including the region below the critical temperature for superfluidity. Differently from the lowest axial breathing mode, the hydrodynamic frequencies of the higher nodal excitations show a temperature dependence, which is calculated starting from Landau two-fluid theory and using the available experimental knowledge of the equation of state. The experimental results agree with high accuracy with the predictions of theory and provide the first evidence for the temperature dependence of the collective frequencies near the superfluid phase transition.

Collective oscillations provide powerful tools to understand the physical behavior of quantum many-body systems from different points of view and to test fundamental theories. On the one hand, collective modes can be used to explore different dynamical regimes of the system, such as superfluid, collisional, or collisionless regimes, for both Bose and Fermi statistics [Pit03, Ing08, Gio08, Blo08]. On the other hand, the mode frequencies allow to probe the equation of state (EOS) of the system, including its temperature dependence. Major benefits result from the high accuracies attainable in the measurements of collective frequencies, which often enable refined investigations of subtle interaction effects.

The many-body physics of unitary Fermi gases, i.e. two-component Fermi gases with infinite scattering length, has attracted tremendous interest over the last decade [Ing08, Gio08, Blo08]. The unitary Fermi gas is characterized by strong interaction effects in the EOS [Kin05b, Hor10, Nas10, Ku12] and reveals a unique universal thermodynamic behavior [Ho04]. Furthermore, at finite temperature, the strong interactions favor the collisional hydrodynamic regime, differently from the common situation in weakly interacting Bose gases. The low-frequency modes of a harmonically trapped Fermi gas have been the subject of intensive experimental [Kin04a, Bar04a, Alt07b] and theoretical (see [Gio08] and references therein) efforts. The temperature dependence has been studied in Refs. [Kin05a, Wri07, Rie08]. Remarkably, at unitarity all modes observed so far turned out to be insensitive to the different nature of a superfluid and a classical gas, with their frequencies remaining independent of temperature throughout the hydrodynamic regime. Previous experiments have demonstrated the crossover from hydrodynamic to collisionless behavior, which typically occurs for temperatures approaching the Fermi temperature, without giving any further information on the regime of lower temperatures where the gas is deeply hydrodynamic and the superfluid phase transition occurs.

In this Letter, we report a joint effort of theory and experiment on higher-nodal collective modes in the unitary Fermi gas. We present a 1D hydrodynamic approach to describe axial modes in a trapped ‘cigar-shaped’ cloud. Our experimental results confirm the predicted intrinsic sensitivity of higher-nodal modes to the EOS in the low-temperature regime, above and even well below the superfluid phase transition.

The macroscopic dynamic behavior of a superfluid is governed by the Landau two-fluid hydrodynamic equations [Kha65] holding in the deep collisional regime $\omega\tau \ll 1$ where τ is a typical collisional time and ω is the frequency of the relevant sound mode in the trap. Landau’s equations consist of the equation of continuity for the total density, the equation for the

velocity of the superfluid component, the equation for the entropy density and the equation for the current density. The physical ingredients entering these equations are the equation of state and the superfluid density. At zero temperature they reduce to the irrotational hydrodynamic equations of superfluids, above the critical point to the usual hydrodynamic equations of normal fluids. Below T_c these equations describe the propagation of first and second sound, the former being basically a density wave, with the normal and superfluid components moving in phase, the latter being a temperature or entropy wave. For weakly compressible fluids the coupling between first and second sound is small [Kha65]. This is the case of superfluid helium and also of the unitary Fermi gas [Tay09]. Since in the present work we investigate the collective oscillations of density (first sound), we simplify the search for the solutions of Landau's equation by requiring that the velocity fields of the normal and superfluid components are equal. Under this approximation the equations of motion involve only the EOS, the superfluid density playing a role only in the propagation of second sound.

In the presence of a trapping potential, the solution of Landau's equations is highly non-trivial, due to the inhomogeneity of the density profile, and has been so far calculated only for the simplest case of isotropic trapping [He07, Tay09]. Since the experimental excitation and observation of these modes are more easily accessible with very elongated traps, in the following we focus on such configurations. In [Ber10] it was shown that under suitable conditions of radial trapping one can derive simplified 1D hydrodynamic equations starting from the more general 3D Landau's equations. The basic point for such a derivation is the assumption that both the velocity field v_z along the long axis and the temperature fluctuations during the propagation of sound do not depend on the radial coordinates. This 1D like hydrodynamic formulation is justified under the condition that the viscosity and the thermal conductivity are sufficiently large to ensure, respectively, the absence of radial gradients in the velocity v_z and the temperature. The condition for the viscosity can be recast in the form $\eta \gg \rho_{n1}\omega$ where ρ_{n1} is the normal 1D mass density, obtained by radial integration of the 3D normal density. An analogous condition holds for the thermal conductivity. These conditions are better satisfied in the presence of tight radial confinement and for the lowest frequency oscillations. One can estimate the values of shear viscosity η using the experimental data of [Cao11b]. For the actual conditions of our experiments both sides of the inequality are of the same order of magnitude and consequently the full applicability of the 1D hydrodynamic formulation can be justified only *a posteriori*. Violation of the 1D condition would result in a damping of the collective oscillations so that, to the extent that the observed damping is small, we expect that the assumption of velocity field and temperature being independent of the radial coordinate is a reasonable ansatz for our variational approach.

Under the above assumptions and focusing on the unitary Fermi gas, the equation for the velocity field, characterizing the density oscillations of the gas in a highly elongated harmonic trap, takes the form (see [Hou13b] for a complete and systematic derivation):

$$m(\omega^2 - \omega_z^2)v_z - \frac{7}{5}m\omega_z^2 z \partial_z v_z + \frac{7}{5} \frac{P_1}{n_1} \partial_z^2 v_z = 0 \quad (4.1)$$

where we have considered oscillations in time proportional to $e^{-i\omega t}$. Here, ω_z represents the trap frequency along the axial direction z , and m is the atom's mass. Eq.(4.1) explicitly points out the crucial role played by the equation of state $P_1(n_1, T)$, where $P_1 =$

$\int P dx dy$ is the “1D pressure” (having units of force) and $n_1 = \int n dx dy$ is the atom number per unit length. In order to derive Eq.(4.1) we have explicitly used the adiabatic result $n_1 (\partial P_1 / \partial n_1)_{\bar{s}_1} = 7/5 P_1$ holding at unitarity at all temperatures, where $\bar{s}_1 = (1/n_1) \int s dx dy$ is the entropy per atom with s the entropy density and we have assumed the validity of the local density approximation along both the axial and radial directions.

At zero temperature and in the classical limit of high temperature the hydrodynamic equation (4.1) admits analytic solutions of polynomial form $v_z = a_k z^k + a_{k-2} z^{k-2} + \dots$, with integer values of k . At $T = 0$, where $P_1(n_1)/n_1 = (2/7)(\mu_0 - (1/2)m\omega_z^2 z^2)$, with μ_0 the chemical potential at the center of the trap, the frequency of the k -th mode is given by

$$\omega^2 = \frac{1}{5}(k+1)(k+5)\omega_z^2. \quad (4.2)$$

In the classical limit, where $P_1/n_1 = k_B T$, one finds the different k dependence

$$\omega^2 = \frac{1}{5}(7k+5)\omega_z^2. \quad (4.3)$$

It is worth noticing that Eqs. (4.2) and (4.3) coincide for $k = 0$ (center of mass oscillation) and $k = 1$ (lowest axial breathing mode), while they predict different values for the higher nodal solutions. One can actually prove that not only the frequency of the center of mass but, at unitarity, also the frequency of the lowest axial breathing mode is independent of temperature, corresponding to an exact scaling solution of the two fluid hydrodynamic equations [Hou13b]. It then follows that only the $k \geq 2$ modes exhibit a temperature dependence.

In order to provide a simple quantitative prediction for the temperature dependence of the mode frequencies, we have developed a variational approach to the solution of the hydrodynamic equation (4.1) with the ansatz $v_z = a_2 z^2 + a_0$ for the $k = 2$ mode. This ansatz reproduces exactly the frequency of the $k = 2$ mode in the limits of $T = 0$ and high T . For intermediate temperatures we obtain [Hou13b]

$$\omega_{k=2}^2 = \frac{129t_2 - 25}{5(9t_2 - 5)}\omega_z^2, \quad (4.4)$$

where $t_2 = M_0 M_4 / M_2^2$. We have introduced the dimensionless moments

$$M_\ell = \int_{-\infty}^{\beta\mu_0} dx (\beta\mu_0 - x)^{(\ell+1)/2} n(x) \lambda_T^3 \quad (4.5)$$

of the 3D number density $n(x)$, where x is the local chemical potential times $\beta = 1/k_B T$ and λ_T is the thermal de Broglie wavelength. The temperature dependence of the moments M_ℓ can be evaluated using the experimentally determined EOS [Ku12]. Approaching the classical regime, for $\beta\mu \lesssim -1.5$, the virial expansion of the EOS [Liu09] holds [Ku12] and allows to extend the integral to $\beta\mu \rightarrow -\infty$. At low temperatures, corresponding to $\beta\mu > 4$, the EOS is governed by phonons and is solely determined by the Bertsch parameter ξ . The error of the quantity t_2 above resulting from the error in the density EOS is less than 1%. We have checked that our variational predictions are practically indistinguishable from the

exact numerical solution of Eq. (4.1). Starting from the equation of continuity one can also calculate the shape of the density oscillations of each mode, proportional to $\partial_z(n_1 v_z)$.

Experimentally, we prepare an ultracold, resonantly interacting Fermi gas by evaporating a two-component spin mixture of fermionic ${}^6\text{Li}$ in an optical dipole trap [Joc03b]. The atomic cloud contains typically $N/2 = 1.5 \times 10^5$ atoms per spin state, and the magnetic field is set to 834 G, right on top of the well-known broad Feshbach resonance [Chi10]. For the lowest temperatures, the trapping beam (wavelength 1075 nm) has a waist of 31 μm , the trap depth is about 2 μK , and the axial and radial trap frequencies are $\omega_z = 2\pi \times 22.52(2)$ Hz and $\omega_r = 2\pi \times 473(2)$ Hz, respectively. For experiments at higher temperatures, the beam waist is increased to 38 μm , and deeper traps are used (up to 16 μK depth) with trap frequencies of up to $\omega_z = 2\pi \times 23.31(3)$ Hz and $\omega_r = 2\pi \times 1226(6)$ Hz. The corresponding Fermi temperatures $T_F = \hbar(3N\omega_r^2\omega_z)^{1/3}/k_B$ vary between about 0.8 and 1.5 μK . We point out that essentially perfect harmonic confinement along the long trap axis (z -axis) is ensured by the magnetic trapping that results from the curvature of the magnetic field used for Feshbach tuning [Joc03b]. Also anharmonicities in the radial confinement remain negligibly small. To probe the ultracold gas we record one-dimensional axial density profiles $n_1(z)$ by near in-situ absorption imaging [SG13].

The temperature T of the gas is set by controlled heating, always starting from a deeply cooled cloud ($T/T_F \approx 0.1$). In the low temperature range ($T \lesssim 0.2 T_F$), we simply introduce a variable hold time of up to 4 s in which residual trap heating slowly increases T . Higher temperatures are reached by parametric heating, modulating the trap power at about $2\omega_r$, and introducing a sufficient hold time to reach thermal equilibrium between the different degrees of freedom. We characterize the resulting temperature in a model-independent way that does not require any *a priori* knowledge of the EOS. Based on the virial theorem [Tho05] we introduce the dimensionless parameter E/E_0 , which represents the total energy $E = 3m\omega_z^2 \int_{-\infty}^{\infty} dz z^2 n_1(z)$ normalized to the energy of a noninteracting, zero-temperature Fermi gas, $E_0 = \frac{3}{4} N k_B T_F$. For a given EOS, the energy scale (E/E_0) can be converted to a temperature scale (T/T_F). Alternatively, we obtain the cloud's temperature by fitting the experimental profiles $n_1(z)$ with T -dependent theoretical profiles [Ho10, Nas10]. For both methods, we apply the EOS according to Ref. [Ku12]. We note that the temperatures obtained by both methods in general show satisfying agreement with each other. At very low temperatures the latter method shows a trend to give slightly lower values of T (up to $\sim 10\%$), which indicates small systematic uncertainties of our measurements.

We selectively excite axial modes of order k by using a resonant excitation scheme. As illustrated in Fig. 4.1(a), a repulsive 532-nm laser beam perpendicularly intersects the trapping beam, with its position and size chosen in a way to provide best mode matching. Typically, the excitation pulse contains 8 cycles of sinusoidal modulation with a half-cycle sine envelope, and the maximum potential height of the excitation beam is kept to about $0.01 k_B T_F$. The power, length and shape of the excitation pulse are optimized in order to resonantly drive the desired small-amplitude oscillation. The amplitude of the corresponding density modulation stays well below 3% of the central density of the cloud.

We record axial density profiles $n_1(z, t)$ of the excited cloud for various time delays t after the excitation pulse. We then perform a Fast Fourier Transform (FFT). The resulting function $\tilde{n}(z, \omega)$ reveals the collective mode spectrum with eigenfrequencies ω_k and the corre-

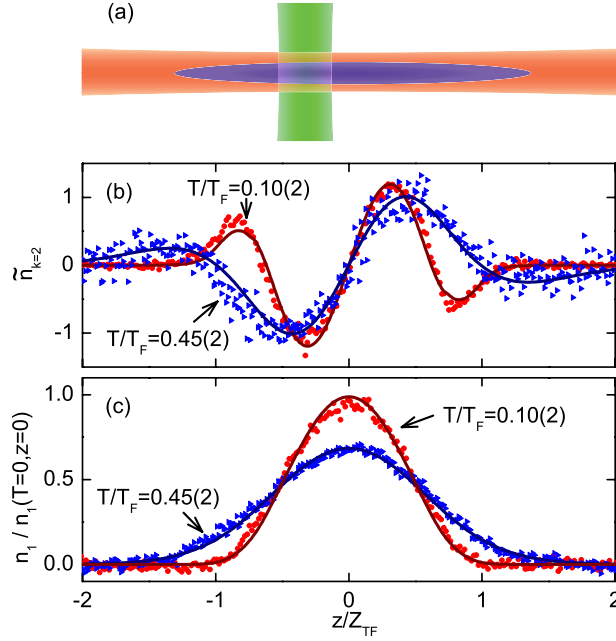


Figure 4.1: (Color online) Probing a higher-order first sound longitudinal mode at the example of $k = 2$. In (a), we illustrate the basic geometry of exciting the optically trapped cloud with a weak, power-modulated repulsive laser beam, which perpendicularly intersects the trapping beam. In (b), the experimental mode profiles (data points) are compared to theoretical curves based on the experimental EOS from [Ku12] (solid lines) for two different temperatures. The corresponding cloud profiles in (c) are analyzed to extract the temperatures (see text). The solid lines show the density profiles obtained from the EOS [Ku12] with $T/T_F = 0.10$ and 0.45 . The parameter $Z_{TF} = \xi^{1/4} \omega_z^{-1} \sqrt{2k_B T_F / m}$ represents the Thomas-Fermi radius of the zero- T interacting gas.

sponding spatial mode profiles $\tilde{n}_k(z)$. We extract the precise frequency of a particular mode k by projecting $n_1(z, t)$ onto the spatial profile $\tilde{n}_k(z)$ and analyzing the resulting oscillation in the time domain [SG13]. The high signal-to-noise ratio results in very low statistical uncertainties in the permille range.

In this way, we study the longitudinal modes with $k = 0, 1, 2$. The measured frequency ω_0 of the sloshing mode ($k = 0$) is an accurate measure of the axial trap frequency ($\omega_{k=0} = \omega_z$), and is therefore used for normalization purposes. The axial compression mode ($k = 1$) has been studied in previous work [Bar04a, Nas09]. Here, in the full temperature range explored ($0.1 \leq T/T_F \leq 0.5$) we observe its frequency very close to $\omega_{k=1} = \sqrt{12/5} \omega_z$. Deviations from this value remain below 0.3% and no significant temperature dependence is observed. This confirms that this mode is insensitive to the temperature as long as the gas stays hydrodynamic. For the higher-nodal mode with $k = 2$, we observe the expected T -dependent frequency variations. Damping increases as compared to the $k = 1$ mode, but remains sufficiently small to observe many oscillations and thus to accurately determine the mode frequency. Typical observed damping times [SG13] are 2 s at $0.5 T_c$, 0.2 s at T_c , and 0.12 s at $2 T_c$. We note that the $k = 3$ mode [SG13] shows very similar behavior, with larger

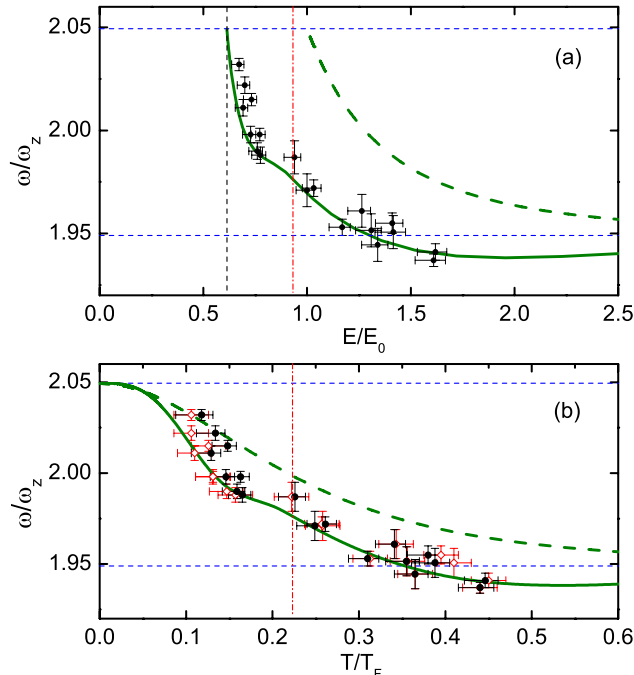


Figure 4.2: (Color online) Comparison between experimental and theoretical first sound frequencies of the $k = 2$ mode. In (a) the experimental data are plotted versus the energy parameter E/E_0 , while in (b) we use a temperature scale T/T_F . The theoretical curves (solid lines) are based on the EOS of Ref. [Ku12]. This EOS is also used to extract T/T_F from the measured profile in two different ways: The filled symbols in (b) result from a direct conversion of E/E_0 to T/T_F , while the open symbols result from fitting the cloud profiles (see text). For comparison, we also show the mode frequencies (dashed curves) that would result from the EOS of the ideal Fermi gas. The thin horizontal dashed lines mark the zero- T superfluid limit ($\omega/\omega_z = \sqrt{21/5}$) and the classical hydrodynamic limit ($\omega/\omega_z = \sqrt{19/5}$) according to Eqs. (4.2) and (4.3), respectively. In (a) the dashed vertical line indicates the $T = 0$ ground state with $E/E_0 = \sqrt{\xi} = 0.613(3)$, while the dash-dot vertical lines in (a) and (b) indicate the critical energy $E_c/E_0 = 0.934(39)$ and temperature $T_c/T_F = 0.223(15)$.

frequency variations but faster damping.

In Fig. 4.1(b) and (c), we show examples for the spatial profiles of the $k = 2$ mode for two different temperatures $T/T_F = 0.10$ and 0.45 along with the corresponding unperturbed density profiles of the cloud. The comparison of the experimental data (data points) with the theoretical results based on the experimental EOS in [Ku12] (solid lines) shows excellent agreement.

Figure 4.2 presents the comparison between the experimental and theoretical frequencies for the $k = 2$ mode. In (a) the normalized mode frequencies $\omega_{k=2}/\omega_z$ are plotted versus the energy parameter E/E_0 , while (b) displays the same data on a temperature scale T/T_F . The experimental data confirm the pronounced temperature dependence of the mode frequencies as predicted by our theory based on the EOS of Ref. [Ku12] (solid line). In comparison, the disagreement with the dependence that would result from the EOS of the ideal Fermi

gas (dashed line) highlights the important role of the EOS. At the lowest temperatures ($T/T_F \approx 0.1$) the frequency lies close to the $T = 0$ superfluid limit, but already shows a significant down-shift amounting to almost 1%. At the highest temperatures ($T/T_F \approx 0.45$) our data show a clear trend to go below the asymptotic high-temperature value, i.e. the classical hydrodynamic limit. The corresponding non-monotonic temperature dependence can be understood based on the first-order correction to the EOS resulting from the virial expansion at high temperatures.

In conclusion, our combined theoretical and experimental work on higher-nodal axial collective modes of a unitary Fermi gas reveals a pronounced temperature dependence below and near the superfluid phase transition. The observed temperature dependence is a unique feature of higher nodal modes, not present for any other collective mode studied in Fermi gases so far. Our theoretical approach is based on a 1D two-fluid hydrodynamic model describing the frequently used elongated ‘cigar-shaped’ trap geometry. The excellent agreement with the experimental results provides a stringent test for the validity of this 1D approach and highlights its potential power to accurately describe second sound modes. Moreover, our measurements provide an independent confirmation of the recently measured EOS of a unitary Fermi gas.

We would like to thank John Thomas for useful discussions and Florian Schreck for discussion and experimental support. The Innsbruck team acknowledges support from the Austrian Science Fund (FWF) within SFB FoQuS (project No. F4004-N16). The Trento team acknowledges support from the European Research Council through the project QGBE. The MIT work was supported by the NSF, AFOSR, ONR, ARO with funding from the DARPA OLE program, and the David and Lucile Packard Foundation.

Chapter 5

Publication: Second sound and the superfluid fraction in a resonantly interacting Fermi gas[†]

accepted for publication in Nature (2013)

Leonid A. Sidorenkov^{1,2}, Meng Khoon Tey^{1,2}, Rudolf Grimm^{1,2}, Yan-Hua Hou³, Lev Pitaevskii^{3,4}, Sandro Stringari³

¹*Institut für Quantenoptik und Quanteninformation (IQOQI), Österreichische Akademie der Wissenschaften, 6020 Innsbruck, Austria*

²*Institut für Experimentalphysik und Zentrum für Quantenphysik, Universität Innsbruck, 6020 Innsbruck, Austria*

³*Dipartimento di Fisica, Università di Trento and INO-CNR BEC Center, I-38123 Povo, Italy*

⁴*Kapitza Institute for Physical Problems RAS, Kosygina 2, 119334 Moscow, Russia*

[†]The author of the present thesis developed the experimental procedure, performed the measurements and analysed the data, together with M.K.T., under the supervision of R.G. Theoretical support was provided by Y.-H.H, L.P. and S.S.

Superfluidity is a macroscopic quantum phenomenon, which shows up below a critical temperature [Kap38, All38] and leads to a peculiar behavior of matter, with frictionless flow, the formation of quantized vortices, and the quenching of the moment of inertia being intriguing examples. A remarkable explanation for many phenomena exhibited by a superfluid at finite temperature can be given in terms of a two-fluid mixture [Tis38, Lan41] comprised of a normal component that behaves like a usual fluid and a superfluid component with zero viscosity and zero entropy. Important examples of superfluid systems are liquid helium and neutron stars. More recently, ultracold atomic gases have emerged as new superfluid systems with unprecedented possibilities to control interactions and external confinement. Here we report the first observation of ‘second sound’ in an ultracold Fermi gas with resonant interactions. Second sound is a striking manifestation of the two-component nature of a superfluid and corresponds to an entropy wave, where the superfluid and the non-superfluid components oscillate in opposite phase, different from ordinary sound (‘first sound’), where they oscillate in phase. The speed of second sound depends explicitly on the value of the superfluid fraction [Kha65], a quantity sensitive to the spectrum of elementary excitations [Lan47]. Our measurements allow us to extract the temperature dependence of the superfluid fraction, which in strongly interacting quantum gases has been an inaccessible quantity so far.

5.1 Main results

Second sound was first measured in liquid helium II (superfluid ^4He below 2.2 K), which represents the paradigm of quantum liquids characterized by strong interactions [Atk59]. For the description of this system and its peculiar properties Landau developed his theory of two-fluid hydrodynamics [Lan41]. In liquid helium II, second sound can be generated [Pes44] by local time-dependent heating and detected by observing the propagation of the resulting temperature wave. In this original context, second sound is characterized as a wave that propagates at constant pressure (isobaric oscillation), in contrast to first sound being a wave that propagates at constant entropy per particle (adiabatic oscillation), just like ordinary sound.

The observation of second sound in ultracold atomic quantum gases has been a long-standing goal. In weakly interacting Bose-Einstein condensed gases, second sound behaves quite differently from the case of liquid helium II. In these systems, the superfluid density coincides with the density of the Bose-Einstein condensed component and, in the experimentally relevant temperature range, second sound reduces to an oscillation of the condensate, the thermal component remaining essentially at rest. The corresponding temperature dependence of the speed of sound was measured in Ref. [Mep09a]. In two other experiments [SK98, Mep09b], the relative motion of the condensate and the thermal component was investigated and frequency shifts and damping effects were observed. In contrast to dilute Bose gases, resonantly interacting Fermi gases [Gio08, Blo08] are characterized by effects of strong interactions. In such systems, superfluidity and the universal thermodynamics

[Ho04, Kin05b, Hor10, Nas10, Ku12] have been subjects of intense research. Here the normal component behaves in a deeply hydrodynamic way in a wide range of temperatures and the spatial overlap between the normal and the superfluid components can be very large also in the presence of harmonic trapping. In this favorable situation, Landau’s two-fluid theory can be readily applied, which suggests a behavior similar to superfluid helium, including the occurrence of second sound.

Our system is an ultracold, superfluid sample of fermionic ${}^6\text{Li}$ atoms, prepared in a highly elongated harmonic trapping potential (Methods) by well-established procedures of laser and evaporative cooling [Tey13]. The sample consists of $N = 3.0 \times 10^5$ atoms in a balanced mixture of the two lowest spin states, and is about $500 \mu\text{m}$ long and $20 \mu\text{m}$ wide. It is characterized by the Fermi temperature $T_F^{\text{trap}} \approx 0.9 \mu\text{K}$ (Methods). A magnetic bias field of 834 G is applied, which tunes the interaction between the two spin components right on top of an s -wave scattering length resonance (‘unitarity limit’ of interactions). The cloud’s temperature T is determined by analyzing axial density profiles [Nas10, Tey13], using the knowledge of the equation of state (EOS) from Ref. [Ku12]. The relevant temperature range for the present experiments is between 0.11 and $0.15 T_F^{\text{trap}}$.

Our method for observing sound propagation builds on the classical scheme to detect the propagation of first sound in Bose-Einstein condensates [And97a], which was also applied to resonantly interacting Fermi gases [Jos07]. The general idea is to prepare the quantum gas in a trap that is highly elongated, to create a local perturbation, and to detect its one-dimensional propagation as a pulse along the long trap axis. In the case of first sound, both the creation and the detection of such an excitation are straightforward, while being less obvious for second sound.

For the local excitation of the cloud, we use a repulsive dipole potential created by a tightly focussed green laser beam (Methods) that perpendicularly intercepts the trapped sample in its center, as shown in Fig. 1a. To excite first sound, we suddenly turn on the repulsive beam. The local reduction of the trapping potential acts on the superfluid and normal component in the same way and creates a small hump in the axial density distribution. To excite second sound, we keep the green beam’s power constant during the whole experimental sequence with the exception of a short power-modulation burst, which contains 8 sinusoidal oscillations in 4.5 ms (Methods and Supplementary Information). The fast modulation locally drives the system out of equilibrium and the following relaxation increases entropy and temperature. The duration of the burst is chosen such that the system can establish a local thermal equilibrium on a length scale that covers the transverse cloud size, but is much shorter than the axial extension of the cloud. In all cases, we take care that the excitation remains a small perturbation of the whole system, which globally stays in a thermal equilibrium state.

For detection we record the axial density profile $n_1(z, t)$ for various time delays t after the excitation pulse, where $n_1(z, t)$ is the number density integrated over the transverse degrees of freedom. To enhance the visibility of the density perturbation, we subtract a background profile $\bar{n}_1(z)$ obtained by averaging the profiles over all measured delay times. Our signal $\delta n_1(z, t) = n_1(z, t) - \bar{n}_1(z)$ is finally normalized to the maximum observed density $n_{1, \text{max}}$.

The key point for the detection of second sound is the coupling [Ara09, Hu10] between temperature and density variations, which occurs in a systems exhibiting thermal expansion.

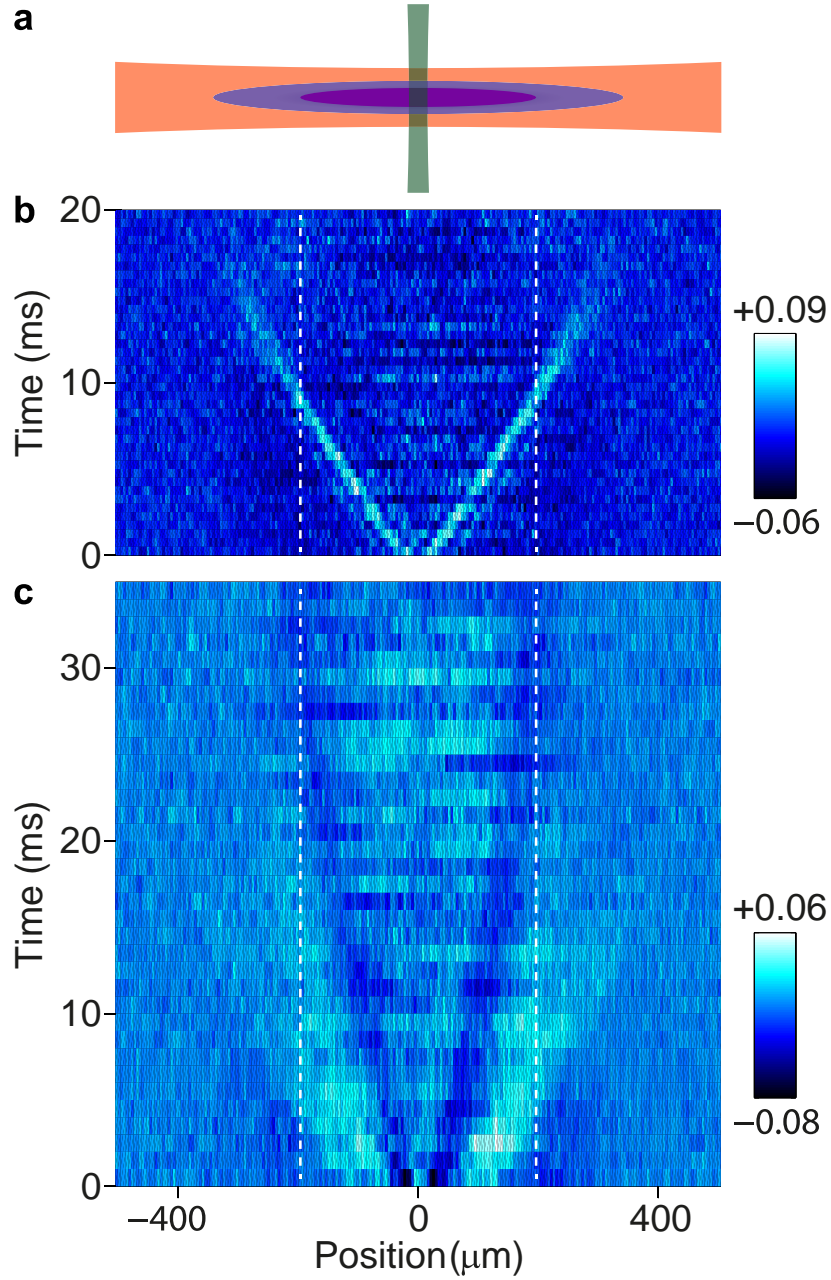


Figure 5.1: **Observing the propagation of first and second sound.** **a**, The basic geometry of exciting the optically trapped cloud with a weak, power-modulated repulsive laser beam (green), which perpendicularly intersects the trapping beam (red). The trapped cloud has a superfluid core ($|z| < 200 \mu\text{m}$), surrounded by a normal region (about 1.5 times larger). **b** and **c**, Normalized differential axial density profiles $\delta n_1(z, t)/n_{1, \max}$ taken for variable delay times after the excitation show the propagation of first sound (local density increase, bright) and second sound (local decrease, dark). The temperature of the atomic cloud is $T = 0.135(10)T_F^{\text{trap}}$. The vertical dashed lines indicate the axial region where superfluid is expected to exist according to a recent determination of the critical temperature [Ku12].

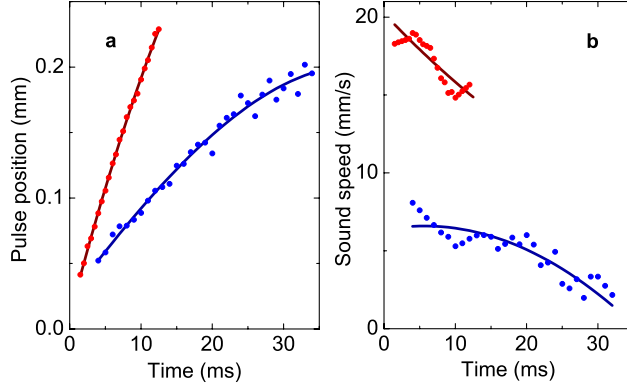


Figure 5.2: **Extracting the sound speeds.** **a**, The positions of the propagating pulses are shown as a function of time. The data points (red and blue symbols for first and second sound, respectively) result from individual fits to the pulses observed at fixed delay times, and the solid lines represent third-order polynomial fits to the time-dependent behavior. **b**, The sound speeds are obtained as derivatives of the fit curves (solid lines) and alternatively by analyzing subsets of nine adjacent profiles (data points).

The relevant isobaric thermal expansion coefficient can be obtained from the EOS and, for our experimental conditions, is found to be sufficiently large to facilitate the observation of a local temperature increase as a dip in the density profiles (Methods and Supplementary Information).

First sound clearly shows up in Fig. 1b. The initially induced hump splits into two density peaks (bright), which symmetrically propagate outward at an almost constant speed, penetrate into the region where there is no superfluid (see dashed lines for the superfluid-normal boundary), and finally fade out in the outer region of the cloud. For longer times, we observe (not shown) a weak collective breathing oscillation to be excited.

The excitation with our local heating scheme leads to a strikingly different picture, as shown in Fig. 1c. The two density dips (dark) propagate much slower than the first-sound signals. They further slow down when approaching the superfluid boundary (dashed lines) and finally disappear without penetrating into the non-superfluid region. This behavior is our ‘smoking gun’ of second sound.

To extract the two sound speeds from the differential profiles $\delta n_1(z, t)$, we determine the positions of the density dips or peaks with Gaussian fit functions. The corresponding time dependence is shown in Fig. 2a, as extracted from the profiles in Fig. 1. We now use a third-order polynomial to globally fit the time-dependent positions (solid lines in Fig. 2a). The sound speeds are then obtained as time derivatives of the fit curves and displayed as solid lines in Fig. 2b. As this procedure by design produces a smooth curve and does not provide sufficient insight into the uncertainties, we also apply a different procedure to analyze the same data. We consider smaller subsets of adjacent points and extract the local speeds by second-order polynomial fits (Supplementary Information). Corresponding results are shown in Fig. 2 by the filled symbols.

The fact that the axial harmonic confinement introduces a z -dependence of the linear

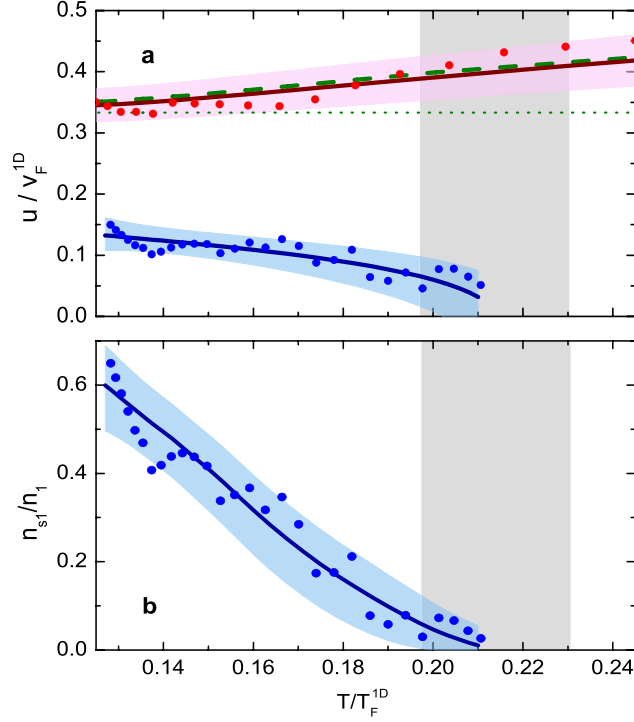


Figure 5.3: **Normalized sound speeds and the 1D superfluid fraction.** **a**, Speeds of first and second sound, normalized to the local Fermi speed and plotted as a function of the reduced temperature. The data points and the solid lines refer to the data set of Fig. 1, following different methods to analyze the raw data (see text). The shaded regions indicate the maximum range of variations from analyzing different data sets. The dashed curve is a prediction based on Eq. 5.1 and the EOS from Ref. [Ku12]. The dotted horizontal line is the corresponding zero-temperature limit for the speed of first sound. **b**, Temperature dependence of the 1D superfluid fraction n_{s1}/n_1 , with symbols, solid line, and shaded uncertainty range corresponding to panel **a**. In both panels, the grey shaded area indicates the uncertainty range of the superfluid phase transition according to Ref. [Ku12].

density n_1 allows us to determine the temperature dependence of the sound speeds, even without changing the global temperature T of the trapped sample. The key is to define a z -dependent Fermi temperature $T_F^{1D} \propto n_1^{2/5}$ (Methods) as the natural local temperature scale. The corresponding reduced temperature T/T_F^{1D} has its minimum at the trap center ($z = 0$) and increases with z . The superfluid phase-transition is crossed when the critical temperature $T_c = 0.214(16)T_F^{1D}$ is reached.

In Fig. 3, we show the temperature dependence of the two speeds of sound, normalized to the local Fermi speed $v_F^{1D} = \sqrt{2k_B T_F^{1D}/m}$, where m is the atomic mass and k_B is Boltzmann's constant. The symbols correspond to the data displayed in Fig. 2. The solid lines are derived in the same way from the corresponding fit curves. To get additional information on the confidence level of our results, we have analyzed a number of data sets taken under similar conditions as the ones in Fig. 1. The regions shaded in pink and light-blue display

the maximum range of variations considering all our different data sets (Supplementary Information).

Our interpretation of the experimental results relies on an effective one-dimensional approach that allows to solve Landau's two-fluid hydrodynamic equations for a highly elongated system [Ber10, Hou13b]. The basic assumptions are a thermal equilibrium in the radial direction and sufficient shear viscosity to establish a flow field that is independent of the radial position. Within this theoretical framework and under the local density approximation, effective 1D thermodynamic quantities can be defined by integration over the transverse degrees of freedom, such that a thermodynamic quantity q yields a 1D counterpart $q_1 \equiv 2\pi \int_0^\infty q r dr$.

We can express the normalized speeds of first and second sound as

$$\frac{u_1}{v_F^{1D}} = \sqrt{\frac{7}{10} \frac{P_1}{n_1 k_B T_F^{1D}}}, \quad (5.1)$$

and

$$\frac{u_2}{v_F^{1D}} = \sqrt{\frac{T}{2k_B T_F^{1D}} \frac{\bar{s}_1^2}{\bar{c}_{p1}} \frac{n_{s1}}{n_{n1}}}, \quad (5.2)$$

where P_1 denotes the 1D pressure (unit of a force), $\bar{s}_1 = s_1/n_1$ is the entropy per particle, and $\bar{c}_{p1} = T(\partial\bar{s}_1/\partial T)_{p1}$ is the isobaric heat capacity per particle. These thermodynamic quantities can be calculated from the EOS as functions of the reduced temperature T/T_F^{1D} , as we discuss in detail in Ref. [Hou13b]. The quantities n_{s1} and $n_{n1} = n_1 - n_{s1}$, which represent the linear number densities of the superfluid and the normal component, cannot be determined from the known EOS.

The speed of first sound provides us with an important benchmark for our experimental method and the interpretation of the measurements in the 1D theoretical framework. The experimental results (red symbols and upper solid line in Fig. 3a) are in excellent agreement with the calculation (dashed line) based on Eq. 5.1 and the EOS from Ref. [Ku12], which is a further confirmation for the validity of our theoretical approach in addition to the recent measurements of the T -dependent frequencies of higher-nodal collective modes [Tey13].

The measured speed of second sound (blue line and data points in Fig. 3a) is observed to decrease with temperature, in contrast to first sound. The general behavior fits very well to the qualitative predictions in Ref. [Ber10]. We can now extract the 1D superfluid fraction n_{s1}/n_1 , which is the unknown quantity in Eq. 5.2. The result is presented in Fig. 3b, where n_{s1}/n_1 shows a smooth increase with decreasing T below the critical temperature.

We finally reconstruct (Methods) the temperature dependence of the superfluid fraction n_s/n for the homogeneous 3D case, which has been an inaccessible quantity so far. The results, shown in Fig. 4, turn out to be rather close to the case of liquid helium II (solid line) [Das57]. In particular, the superfluid part is practically 100% below $0.6 T_c$. This behavior is quite different from the one exhibited by a weakly interacting Bose gas, whose superfluid fraction lies significantly below the data of Fig. 4 and is well approximated by the condensate fraction of the ideal Bose gas (dashed line). In strongly interacting quantum fluids, the superfluid and the condensate fractions simultaneously appear at the phase transition, but they exhibit quite different temperature dependencies below T_c . Our experimental results provide a new benchmark for advancing theoretical approaches to calculate the superfluid

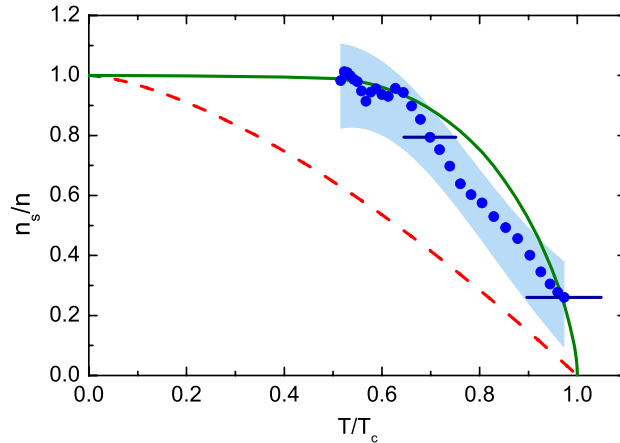


Figure 5.4: **Superfluid fraction for the homogeneous case.** The data points and the corresponding uncertainty range (shaded region) show the superfluid fraction for a uniform resonantly interacting Fermi gas versus T/T_c as reconstructed from its 1D counterpart in Fig. 3b (Methods). The two horizontal error bars indicate the systematic uncertainties resulting from the limited knowledge of the critical temperature T_c . For comparison, we show the fraction for helium II (solid line) as measured in Ref. [Das57] and the textbook expression $1 - (T/T_c)^{3/2}$ for the Bose-Einstein condensed fraction of the ideal Bose gas (dashed line).

fraction, which is a challenging problem in quantum many-body physics (Supplementary Information). With additional tuning of the interaction conditions, corresponding information may be obtained throughout the whole crossover [Gio08, Blo08, Hei06] from a molecular Bose-Einstein condensate, for which the superfluid fraction should approach the dashed line in Fig. 4, to a Bardeen-Cooper-Schrieffer-type superfluid.

From the fundamental point of view, the experimentally determined superfluid fraction represents a so far missing thermodynamic function, which contains information on the spectrum of elementary excitations and completes the description of the superfluid in terms of universal thermodynamics. In a broader perspective, the creation of second sound represents a paradigm for the ability to control the relative motion of a superfluid with respect to the normal component. This may find applications in other situations and geometries, where resonantly interacting Fermi gases are used as model systems for exploring dynamical and transport phenomena [Nas09, Som11, Sta12].

We thank E. R. Sánchez Guajardo for his contributions in the early stage of this work. The Innsbruck team acknowledges support from the Austrian Science Fund (FWF) within SFB FoQuS (project No. F4004-N16). The Trento team acknowledges support from the European Research Council through the project QGBE.

5.2 Methods

Trapping potential. In our hybrid trap³¹, the tight radial confinement with a trapping frequency $\omega_r/(2\pi) = 539(2)$ Hz is provided by an infrared laser beam (wavelength 1075 nm, power 120 mW, waist $39\mu\text{m}$). The much weaker axial confinement with a trapping frequency $\omega_z/(2\pi) = 22.46(7)$ Hz results from the curvature of the applied magnetic field. The frequency ratio $\omega_r/\omega_z \approx 24$ corresponds to the aspect ratio of the trapped cloud.

Sound excitation and detection. The green laser beam (wavelength 532 nm, power < 20 mW) used for excitation is focused to a waist in the range of $25\text{-}35\mu\text{m}$. To excite first sound, we suddenly turn it on to introduce a repulsive potential hill with a height of about 10% of the cloud's chemical potential in the trap center. For the case of second sound, the repulsive beam is permanently on during the preparation of the quantum gas with a barrier height of about 15% of the cloud's chemical potential. The excitation is then induced by a burst of 8 cycles of sinusoidal power modulation. The modulation frequency is set to 1720 Hz, but the scheme is rather robust and was found to work best in a frequency range between roughly 2 and 3.5 times the radial trapping frequency. The burst envelope is rectangular and the modulated barrier has a peak-to-peak amplitude of 30% of the cloud's chemical potential. After the burst, the power is set back to its initial constant value. On the time scale of the axial motion, the time-averaged power of the green beam is constant, which avoids direct excitation of first sound.

For the detection of the propagating second-sound signal, the corresponding density dip is essential. The 1D formulation of the EOS in Ref. [Hou13b] allows us to relate the observed depth to the relative temperature change. In the temperature range of our experiments, the corresponding thermodynamic coefficient $(\delta n_1/n_1)/(\delta T/T)$ takes values [Hou13b] between -0.4 and -0.6 , which means that the typical 3% relative depth of the density dip roughly corresponds to a local temperature increase of about 6%.

1D Fermi temperature and critical temperature. Three different definitions for Fermi temperatures are related to natural energy scales of our trapping geometry. The homogeneous case with a 3D number density n (including both spin states) is given by $k_B T_F = (3\pi^2)^{2/3} \frac{\hbar^2}{2m} n^{2/3}$. Within the local density approximation the corresponding Fermi energy for N atoms in a three-dimensional harmonic potential is given by $k_B T_F^{\text{trap}} = \hbar(3N \omega_r^2 \omega_z)^{1/3}$, commonly used to describe the global situation of a 3D trap. The Fermi energy of cylindrically confined cloud in the center of a 2D harmonic trap, which we refer to as '1D Fermi temperature', follows from $k_B T_F^{1D} = (\frac{15\pi}{8})^{2/5} (\hbar\omega_r)^{4/5} (\frac{\hbar^2 n_1^2}{2m})^{1/5}$, where the relevant density is the linear number density n_1 . For the additional axial confinement in our trap geometry, n_1 and thus T_F^{1D} become z -dependent quantities.

For specifying the critical temperature T_c in units of the relevant Fermi temperature, we also distinguish between the three different situations of a homogeneous system, a 3D harmonic trap, and a cylinder with 2D harmonic confinement. For the homogeneous system, $T_c = 0.167(13) T_F$ was measured in Ref. [Ku12]. Based on the local density approximation and the experimentally determined EOS, this result can be translated into corresponding conditions for the other two situations. While for the 3D trap, $T_c = 0.223(15) T_F^{\text{trap}}$ is relevant for the occurrence of the phase transition at the center of the trap, the condition $T_c = 0.214(16) T_F^{1D}$ applies to the 2D confined case. In our highly elongated trap geometry

with weak axial confinement, T_F^{1D} and thus T_c become z -dependent. For a fixed global temperature T , the condition $T < T_c(z)$ then determines the axial range, where a superfluid exists (see illustration in Fig. 1a and dashed lines in 1b and 1c).

Reconstruction of superfluid fraction. Within the framework of universal thermodynamics [Ho04], the number density of a uniform, resonantly interacting Fermi gas can be expressed in terms of a dimensionless universal function $f_n(x)$ by $n(x, T) = \lambda_T^{-3} f_n(x)$. Here $\lambda_T = (\frac{2\pi\hbar^2}{mk_B T})^{1/2}$ is the thermal de Broglie wavelength, and the dimensionless parameter $x = \mu/k_B T$ gives the ratio between the chemical potential μ and the thermal energy $k_B T$, with a unique correspondence existing between x and T/T_F . The function $f_n(x)$ is known from measurements of the EOS [Kin05b, Hor10, Nas10, Ku12]. The superfluid density can be expressed in an analogous way as $n_s = \lambda_T^{-3} f_{ns}(x)$, introducing a corresponding universal function $f_{ns}(x)$, which is to be extracted from our measurements. Using the local density approximation, one can show for a system with radial harmonic confinement that [Nas10] $n_1(x_0, T) = \frac{2\pi}{m\omega_r^2} \frac{k_B T}{\lambda_T^3} \int_{-\infty}^{x_0} f_n(x) dx$, where x_0 represents the value of x on the trap axis. Analogously, the 1D superfluid density is given by $n_{s1}(x_0, T) = \frac{2\pi}{m\omega_r^2} \frac{k_B T}{\lambda_T^3} \int_{-\infty}^{x_0} f_{ns}(x) dx$. One thus easily sees that the 1D superfluid fraction is given by $n_{s1}/n_1 = \int_{-\infty}^{x_0} f_{ns}(x) dx / \int_{-\infty}^{x_0} f_n(x) dx$ and only depends on x_0 . From our experimentally determined n_{s1}/n_1 , we readily obtain the superfluid fraction of a uniform gas using the relation $\frac{n_s}{n} = \frac{f_{ns}(x_0)}{f_n(x_0)} = \frac{1}{f_n(x_0)} \frac{d}{dx_0} \left[\frac{n_{s1}}{n_1} \int_{-\infty}^{x_0} f_n(x) dx \right]$.

5.3 Supplementary material

5.3.1 Excitation scheme for second sound

Figure S5.5 shows the power modulation of the repulsive 532-nm laser beam during an experimental cycle in which we excite second sound. The power of the beam is kept at a constant level P_0 during the sample preparation stage, which includes the evaporative cooling stage and the subsequent adiabatic recompression stage. To excite second sound, we sinusoidally modulate the beam power around P_0 for 8 cycles at a frequency of 1720 Hz, and fix the power again at P_0 after the modulation. The advantage of keeping the average power unchanged throughout the excitation scheme is that it avoids the excitation of first-sound pulses, which would contaminate the signal of second sound. We found that this local heating scheme is rather robust and it works best in a frequency range between 2 and 3.5 times the radial trapping frequency. Also, we investigated the optimum beam size for efficient local heating. A beam that is too tightly focussed does not work efficiently, whereas a beam which is too large does not fit our purpose of creating a sufficiently localized excitation. We found that the beam width that gives clearest second-sound pulses should be slightly smaller than the width of the trapping beam.

5.3.2 Determining local T/T_F^{1D}

To extract the local T/T_F^{1D} in an atom cloud, we determine the temperature T of the cloud by analyzing the cloud profile [Tey13, SG13] using the equation of state (EOS) from Ref. [Ku12]. With the accurate knowledge of the trap frequencies and the total atom number, we then reconstruct the local 1D density profile $n_1(z)$ using again the EOS. Because the 1D Fermi temperature is related

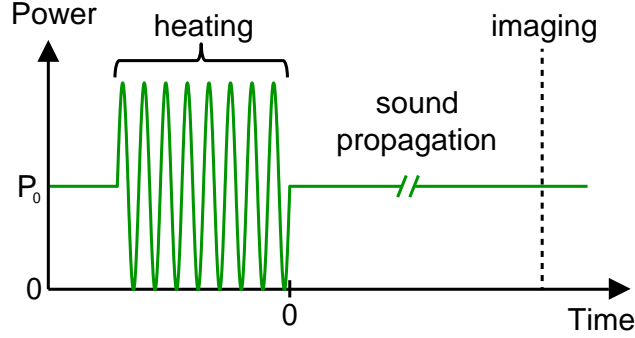


Figure 5.5: Schematic diagram showing the power modulation of the 532-nm beam as applied for the excitation of second sound.

to n_1 by $k_B T_F^{1D} = (\frac{15\pi}{8})^{2/5} (\hbar\omega_r)^{4/5} (\frac{\hbar^2 n_1^2}{2m})^{1/5}$, we can obtain T/T_F^{1D} at any location along the cloud. We use the reconstructed n_1 instead of the directly measured one as this is less sensitive to noise in the measured spatial profile. Figure S5.6 illustrates the measured 1D density profile (a) and the corresponding T/T_F^{1D} (b) for a sample having a temperature of $T = 0.135(10) T_F^{\text{trap}}$.

In a second-sound experiment, the green beam is kept on during the whole experimental cycle. This causes a small ‘dip’ in the 1D density profile of the cloud at equilibrium and could introduce an error in the temperature determination [SG13]. Therefore, in practice, we always obtain the temperature T from samples prepared without the green beam, assuming negligible influence of the green beam on the sample preparation. We checked that indeed the atom numbers in the samples prepared with or without the green beam are the same within statistical uncertainties.

5.3.3 Coupling between the density variation and the temperature variation in second sound

The two-fluid Landau hydrodynamic equations provide the following equations for the sound velocities

$$u^4 - u^2 \left[\frac{1}{m} \left(\frac{\partial P_1}{\partial n_1} \right)_{\bar{s}_1} + \frac{1}{m} \frac{n_{s1} T \bar{s}_1^2}{n_{n1} \bar{c}_{v1}} \right] + \frac{1}{m^2} \frac{n_{s1} T \bar{s}_1^2}{n_{n1} \bar{c}_{v1}} \left(\frac{\partial P_1}{\partial n_1} \right)_T = 0, \quad (5.3)$$

where we have considered the 1D configuration discussed in the main text, characterized by tight radial confinement. In the above equation $\bar{s}_1 = s_1/n_1$ is the entropy per particle. The quantities P_1 , s_1 , n_1 , n_{n1} and n_{s1} , corresponding to the 1D pressure, entropy, density, normal-fluid density and superfluid density, respectively, are calculated by carrying out the radial integral of the bulk quantities using the local density approximation (LDA). Here, $\bar{c}_{v1} = T(\frac{\partial \bar{s}_1}{\partial T})_{n_1}$ is the specific heat per particle calculated at constant 1D density. Our 1D formulation using LDA should not be confused with the strict 1D regime where all the particles occupy the lowest single particle state of the radial harmonic potential. Equation (5.3) gives rise to two solutions, hereafter called first (u_1) and second (u_2) sound velocities. Superfluid Fermi gases are weakly compressible and the term containing the inverse adiabatic compressibility dominates the coefficient of the u^2 term in Eq. (5.3). Furthermore the condition

$$\frac{u_2^2 \bar{c}_{p1} - \bar{c}_{v1}}{u_1^2 \bar{c}_{v1}} \ll 1 \quad (5.4)$$

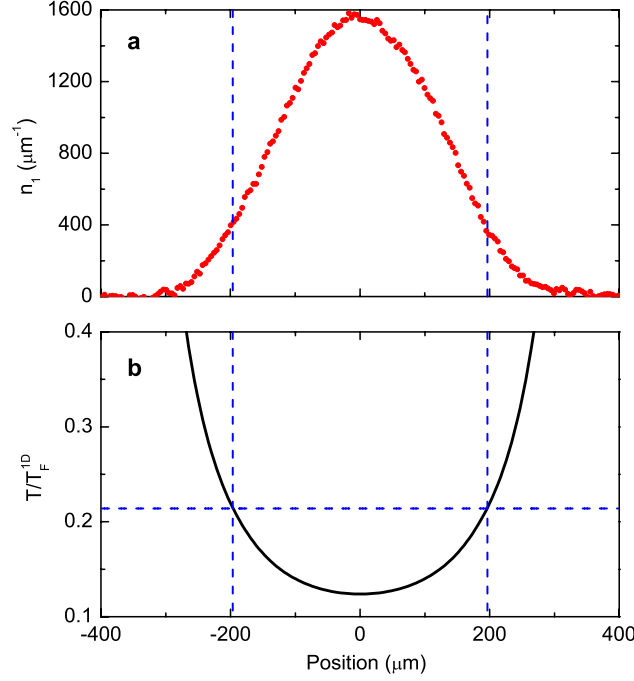


Figure 5.6: Position dependence of the measured linear number density n_1 and the corresponding T/T_F^{1D} along the highly elongated atomic cloud. **a**, 1D density profile n_1 averaged over eight samples prepared in an identical way. **b**, The corresponding local T/T_F^{1D} . The horizontal dashed line represents the critical temperature $T_c = 0.214(16)T_F^{1D}$ for a cylindrically trapped gas with a harmonic radial confinement. The vertical dashed lines in both **a** and **b** indicate the boundaries within which a superfluid exists. The temperature of the sample is $T = 0.135(10)T_F^{\text{trap}}$.

is always well satisfied. Under these conditions, the two solutions of Landau's hydrodynamic equations take the simplified forms

$$u_1^2 = \frac{1}{m} \left(\frac{\partial P_1}{\partial n_1} \right)_{\bar{s}_1}, \quad (5.5)$$

and

$$u_2^2 = \frac{1}{m} \frac{n_{s1} T \bar{s}_1^2}{n_{n1} \bar{c}_{p1}}, \quad (5.6)$$

where the derivative at constant \bar{s}_1 corresponds to an adiabatic transformation. At unitarity Eqs. (5.5) and (5.6) reduce to Eqs. (1) and (2) in the main text after being normalized with the 1D Fermi speed v_F^{1D} . Under the same condition (5.4) the first sound solution corresponds to an adiabatic wave, propagating at constant entropy per particle, while the second sound solution to an isobaric wave, propagating at constant pressure [Hou13b].

Because of the isobaric nature of the second sound mode the corresponding density variations are related to the temperature variations by the equation

$$\frac{\delta n_1/n_1}{\delta T/T} = \frac{T}{n_1} \left(\frac{\partial n_1}{\partial T} \right)_{P_1} = -T\alpha_1, \quad (5.7)$$

where α_1 is the 1D thermal expansion coefficient. At unitarity α_1 is directly related to the specific heats \bar{c}_{p_1} and \bar{c}_{v_1} by the simple relation $T\alpha_1 = (5/2)(\bar{c}_{p_1} - \bar{c}_{v_1})/\bar{c}_{v_1}$ showing that, even for moderately large values of α_1 , the condition (5.4) is well satisfied since $u_2^2 \ll u_1^2$. We find that in the temperature interval related to our experiment the value of $T\alpha_1$ is sufficiently large (between 0.4 and 0.6) to ensure the visibility of the density signal associated with second sound.

5.3.4 Measurement uncertainties

The analysis and interpretation of our data is subject to various statistical and systematic uncertainties, which we here discuss in more detail. For a second-sound data set, as the one in Fig. 1c in the main text, we typically take a total number of 210 spatial profiles, recorded for 35 different delay times with 6 individual images for each delay time. Some shots (up to 3 per delay time) are rejected when the quality of the image is insufficient, e.g. because of interference fringes or unusually large fluctuations in the atom number, and an average is taken over the remaining reliable profiles. With an experimental cycle time of about 15 s, the total data acquisition time for a set like the one in Fig. 1c is about 1 hour, which makes the experiment very sensitive to instabilities and external perturbations. To avoid slow drifts in the experiment causing any systematic behavior, we take all 210 profiles in a fully random order. In addition, 6 profiles are recorded without the sound excitation for determining the global temperature T .

Analyzing an individual set of measurements

The main source of uncertainties in our measured sound speeds and the derived superfluid fraction stems from the determination of the positions of the propagating pulses. The signal-to-noise ratio, i.e. the pulse amplitude versus background noise in the recorded density, is in general quite low, as we apply only small perturbations to ensure linear behavior. The signal-to-noise ratio is roughly 5 for the first-sound signal (after averaging) as presented in Fig. 1b in the main text. For the second-sound pulses (Fig. 1c) the signal-to-noise ratio is about 4 near the center of the cloud and drops quickly to about 1 near the superfluid boundary. This explains the larger fluctuations in the position of the second-sound pulse away from the cloud center as shown in Fig. 2a in the main text. We carefully analyze the quality of the fit for each position data point and reject some of the points where the fit result is not reliable.

While determining the sound speeds we face the problem that even small noise in the position data results in substantial noise when the time derivative is taken. We therefore adopt two different methods, based on global and local fits to the position-versus-time data. Our first method is based on a global fit to the whole set of position data points. Here we use a third-order polynomial, which we generally find to fit the data very well. The second-sound data set displayed in Fig. 2a has in total 31 position data points (after the rejection of 4 unreliable points). Finally we take the derivative of the fit curve to determine the sound speed as a function of delay time. Our second method is based on locally fitting a set of 9 adjacent points with a parabola. We define the local sound speed as the slope of this fit at the central (5th) point. The corresponding results are represented by the filled circles in Fig. 2b. This approach cannot give the local speeds at the first 4 points and the last 4 points in the full data set. We thus extract the local speeds of the first 4 data points simply from the derivative of the fit to the first 9 data points at the 1st, 2nd, 3rd, and 4th positions. The same procedure is applied to the last 4 data points.

While the first method relies on the assumption of a global fit function and thus provides a smooth curve, the second one is a compromise between extracting local information, independent of a specific fit function, and the noise reduction from a fit to several points. In the first method,

all statistical errors of individual points jointly influence the whole curve, while in the second case statistical fluctuations become visible. We carried out a corresponding data analysis for different number of data points per subset and found 9 points to be a good choice. The comparison of the results obtained with both methods shows that the global fit function represents the whole data set very well. The comparison also gives information on statistical uncertainties in the sound speed data.

We note that some other data sets that we recorded were more strongly affected by fluctuations in the experiment, such that we had to reject up to half of the position data points. In such cases we have reduced the number of fit parameters, by fixing the starting position of the propagating pulse or using a second-order polynomial instead of a third-order one. Even in these cases we found the global fit method to provide reasonable results, consistent with the results obtained from other data sets with less noise problems.

Comparing different sets of measurements

We have recorded and analyzed a total number of 7 data sets for both the first- and the second-sound signals and checked for effects of the global temperature and of the power of the trapping light. We could not identify any significant systematic trend, and to express the maximum range of statistical uncertainties we define a confidence range of our measurements in such a way that it includes the results from all individual sets of measurements as analyzed by the global fit method. In this way we obtained the shaded regions in Figs. 3 and 4.

Experimenting with various temperatures instead of focusing on a single temperature allows us to check the reliability of our method. If our method is correct and is free of systematic errors that depend on the global temperature, the local results extracted from samples of different temperatures should agree with each other. In fact, we have measured the second-sound propagation signal for temperatures ranging from $0.11T_F^{\text{trap}}$ up to the critical temperature T_c of about $0.23T_F^{\text{trap}}$. It is clear from these measurements that the cloud region where second sound propagates shrinks as the temperature increases, and no second-sound signal can be observed above T_c . However, as the temperature increases the second sound signal also becomes much noisier and cannot be reliably used to extract the local quantities of interest. We therefore focussed our main experimental efforts to the region between 0.11 to $0.15T_F^{\text{trap}}$, and in particular the to ‘optimum’ temperature $0.135T_F^{\text{trap}}$ as used for our main sets of data.

We also varied the laser power of the optical trap within a factor of two above and a factor of three below the standard value. This affects the aspect ratio and also residual effects of the anharmonicity of the radial trapping potential. The data analysis did not show any significant trend, which gives us further confidence that we have chosen an optimum parameter set for our experiments.

Fig. S5.7 corresponds to Fig. 3a in the main text, with the additional lines (thin solid lines) showing the results from the global fit analysis of all our data sets. The thicker solid lines in the figure represent the results from our most reliable data set, which lie close to the average of all other data sets. The shaded areas approximately cover the maximum range of variations of all our data sets and thus correspond to a confidence range for our results.

The same procedure to determine a confidence range for the experimental results is also applied to the superfluid fraction in Fig. 3b and Fig. 4 in the main text. The shaded areas cover the maximum range of variations as derived by the global fit method from all different data sets. The full circles in Fig. 4 in the main text correspond to the results from the most reliable set, which are well centered in the shaded confidence range.

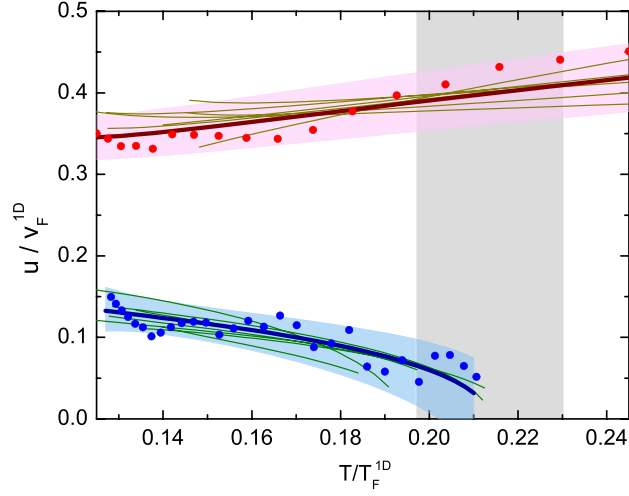


Figure 5.7: Normalized speeds for the first and second sound obtained from different data sets. The thick solid lines and full circles are identical to those shown in Fig. 3a in the main text. The thick solid lines represent the global-fit results of the most reliable first- and second-sound data sets whose values also lie close to the ‘average’ of other data sets. The thinner solid lines represent the global-fit results from all other data sets. The shaded areas approximately cover the maximum range of variations of all fits.

Systematic uncertainties

Various possible sources of systematic errors are present. We can determine the number of atoms within a calibration error of 20%, which leads to an uncertainty in the 1D Fermi temperatures of less than 8% and in the Fermi speeds of less than 4%. The uncertainty arising from the calibration of the imaging scale is less than 2% and thus negligibly small. The uncertainty in the determination of the global temperature is about 10% near the superfluid phase transition and about 15% for the lowest temperatures investigated, see Ref. [Tey13]. Individual data sets as the ones presented in Fig. 1b and 1c are analyzed under the assumption of a constant temperature. Therefore any kind of uncertainty in the determination of this temperature appears as a systematic effect in the whole set.

The interpretation of our results relies on knowledge of the equation of state (EOS); here we use the most recent measurements [Ku12] published by the MIT group. The EOS is used for determining the global temperatures from the spatial profiles, and provides the necessary thermodynamic functions to derive the superfluid fraction. The noise in the EOS data is so small that statistical uncertainties in our analysis remain well below other noise sources. Small systematic uncertainties may be present, which are very difficult to be quantified. Since the MIT data were carefully benchmarked with certain limiting cases, like the ideal non-interacting Fermi gas, and a detailed discussion in comparison with previous experimental results and theoretical approaches was provided, we are very confident that systematic uncertainties in the EOS are so small that they do not affect our data in a significant way.

A further source of an uncertainty may result from limitations to the validity of the 1D hydrodynamic approach in our elongated trap. However, our previous investigation of the temperature dependence of higher-nodal first-sound collective modes in Ref. [Tey13] shows excellent agreement

of the observed and calculated mode frequencies on the level of a few 10^{-3} . Moreover, in the present experiments we get essentially perfect agreement between observed and calculated first-sound velocities. We have no reason to believe that second sound is more sensitive to a breakdown of the 1D hydrodynamic approach to solve Landau's two-fluid equations than first sound. Also the data sets that we took with smaller aspect ratios do not reveal any significant trend. Therefore we are confident that our 1D hydrodynamic approach is an excellent approximation to the real experimental situation and does not provide significant systematic uncertainties.

We finally note that we have also checked in how far the use of Eq. (5.6), rather than using the exact solution of Eq. (5.3), affects the determination of the superfluid fraction from the measured second-sound speed. Deviations stay below one percent and are thus negligible as compared to the other uncertainties.

5.3.5 Available theoretical models for the superfluid fraction n_s/n

Several authors have already provided theoretical predictions for the temperature dependence of the superfluid fraction of the uniform Fermi gas at unitarity. A comprehensive discussion is contained in the publication [Tay08] by Taylor et al. However, it is not natural to compare these predictions with the experimental findings reported in our present work. The available calculations in fact predict values of the critical temperature which are in general significantly higher than the experimental value of $0.167(13) T_F$ (Ref. [Ku12]). Therefore, the comparison in the temperature range relevant to our experiment ($0.09 < T/T_F < 0.16$), where the fraction n_s/n significantly deviates from unity, is not particularly useful. Theoretical predictions in the lower temperature region, corresponding to $T/T_F < 0.09$ and accounting for the effects of fermionic excitations in addition to the leading phonon contribution, have been also reported [And03, Sal10], but we have no data for comparison in this temperature range. On the other hand, the most reliable quantum many-body calculations providing accurate values for the critical temperature of the superfluid transition [Bur06, Hau07, Gou10] have not yet provided predictions for the temperature dependence of the superfluid fraction.

Bibliography

- [Ada94] C. S. Adams, M. Sigel, and J. Mlynek, *Atom optics*, Phys. Rep. **240**, 143 (1994).
- [All38] J. F. Allen and A. D. Misener, *Flow Phenomena in Liquid Helium II*, Nature **142**, 643 (1938).
- [Alt07a] A. Altmeyer, *Collective oscillations of an ultracold quantum gas in the BEC-BCS crossover regime*, Ph.D. thesis, University of Innsbruck (2007).
- [Alt07b] A. Altmeyer, S. Riedl, C. Kohstall, M. J. Wright, R. Geursen, M. Bartenstein, C. Chin, J. Hecker Denschlag, and R. Grimm, *Precision Measurements of Collective Oscillations in the BEC-BCS Crossover*, Phys. Rev. Lett. **98**, 040401 (2007).
- [Alt07c] A. Altmeyer, S. Riedl, M. J. Wright, C. Kohstall, J. Hecker Denschlag, and R. Grimm, *Dynamics of a strongly interacting Fermi gas: The radial quadrupole mode*, Phys. Rev. A **76**, 033610 (2007).
- [And95] M. H. Anderson, J. R. Ensher, M. R. Matthews, C. E. Wieman, and E. A. Cornell, *Observation of Bose-Einstein condensation in dilute atomic vapor*, Science **269**, 198 (1995).
- [And97a] M. R. Andrews, D. M. Kurn, H.-J. Miesner, D. S. Durfee, C. G. Townsend, S. Inouye, and W. Ketterle, *Propagation of Sound in a Bose-Einstein Condensate*, Phys. Rev. Lett. **79**, 553 (1997).
- [And97b] M. R. Andrews, C. G. Townsend, H.-J. Miesner, D. S. Durfee, D. M. Kurn, and W. Ketterle, *Observation of interference between two Bose condensates*, Science **275**, 637 (1997).
- [And03] N. Andrenacci, P. Pieri, and G. C. Strinati, *Evolution from BCS superconductivity to Bose-Einstein condensation: Current correlation function in the broken-symmetry phase*, Phys. Rev. B **68**, 144507 (2003).
- [Ara09] E. Arahata and T. Nikuni, *Propagation of second sound in a superfluid Fermi gas in the unitary limit*, Phys. Rev. A **80**, 043613 (2009).
- [Arn99] M. Arndt, O. Nairz, J. Vos-Andreae, C. Keller, G. van der Zouw, and A. Zeilinger, *Wave-particle duality of C-60 molecules*, Nature **401**, 680 (1999).
- [Atk59] K. R. Atkins, *Liquid helium*, Cambridge University Press, Cambridge (1959).
- [Ban00] Y. B. Band, M. Trippenbach, J. P. Burke, and P. S. Julienne, *Elastic Scattering Loss of Atoms from Colliding Bose-Einstein Condensate Wave Packets*, Phys. Rev. Lett. **84**, 5462 (2000).

- [Ban01] Y. B. Band, J. P. Burke, A. Simoni, and P. S. Julienne, *Suppression of elastic scattering loss for slowly colliding Bose-Einstein condensates*, Phys. Rev. A **64**, 023607 (2001).
- [Bar04a] M. Bartenstein, A. Altmeyer, S. Riedl, S. Jochim, C. Chin, J. Hecker Denschlag, and R. Grimm, *Collective Excitations of a Degenerate Gas at the BEC-BCS Crossover*, Phys. Rev. Lett. **92**, 203201 (2004).
- [Bar04b] M. Bartenstein, A. Altmeyer, S. Riedl, S. Jochim, C. Chin, J. Hecker Denschlag, and R. Grimm, *Crossover from a Molecular Bose-Einstein Condensate to a Degenerate Fermi Gas*, Phys. Rev. Lett. **92**, 120401 (2004).
- [Bar05a] M. Bartenstein, *From Molecules to Cooper Pairs: Experiments in the BEC-BCS Crossover*, Ph.D. thesis, Innsbruck University (2005).
- [Bar05b] M. Bartenstein, A. Altmeyer, S. Riedl, R. Geursen, S. Jochim, C. Chin, J. Hecker Denschlag, R. Grimm, A. Simoni, E. Tiesinga, C. J. Williams, and P. S. Julienne, *Precise determination of ^6Li cold collision parameters by radio-frequency spectroscopy on weakly bound molecules*, Phys. Rev. Lett. **94**, 103201 (2005).
- [Bar13] C. E. Bardyn, M. A. Baranov, C. V. Kraus, E. Rico, A. Imamoglu, P. Zoller, and S. Diehl, *Topology by dissipation*, arXiv:1302.5135 (2013).
- [Bed88] J. G. Bednorz and K. A. Müller, *Perovskite-Type Oxides - the New Approach to High- T_c Superconductivity. Nobel Lecture*, Angewandte Chemie International Edition **27**, 735 (1988).
- [Ber10] G. Bertaina, L. Pitaevskii, and S. Stringari, *First and Second Sound in Cylindrically Trapped Gases*, Phys. Rev. Lett. **105**, 150402 (2010).
- [Blo08] I. Bloch, J. Dalibard, and W. Zwerger, *Many-body physics with ultracold gases*, Rev. Mod. Phys. **80**, 885 (2008).
- [Blo12] I. Bloch, J. Dalibard, and S. Nascimbene, *Quantum simulations with ultracold quantum gases*, Nature Phys. **8**, 267 (2012).
- [Bon04] K. Bongs and K. Sengstock, *Physics with coherent matter waves*, Rep. Prog. Phys. **67**, 907 (2004).
- [Bra95] C. C. Bradley, C. A. Sackett, J. J. Tollett, and R. G. Hulet, *Evidence of Bose-Einstein condensation in an atomic gas with attractive interactions*, Phys. Rev. Lett. **75**, 1687 (1995).
- [Bro23] L. de Broglie, *Waves and quanta*, Nature **112**, 540 (1923).
- [Bug04] C. Buggle, J. Léonard, W. von Klitzing, and J. T. M. Walraven, *Interferometric Determination of the s and d-Wave Scattering Amplitudes in ^{87}Rb* , Phys. Rev. Lett. **93**, 173202 (2004).
- [Bul05] A. Bulgac, *Specific Heat of a Fermionic Atomic Cloud in the Unitary Regime*, Phys. Rev. Lett. **95**, 140403 (2005).
- [Bur06] E. Burovski, N. Prokof'ev, B. Svistunov, and M. Troyer, *Critical Temperature and Thermodynamics of Attractive Fermions at Unitarity*, Phys. Rev. Lett. **96**, 160402 (2006).

- [Cao11a] C. Cao, E. Elliott, J. Joseph, J. Petricka, T. Schäfer, and J. E. Thomas, *Universal Quantum Viscosity in a Unitary Fermi Gas*, *Science* **331**, 58 (2011).
- [Cao11b] C. Cao, E. Elliott, H. Wu, and J. E. Thomas, *Searching for perfect fluids: quantum viscosity in a universal Fermi gas*, *New J. Phys.* **13**, 075007 (2011).
- [Cap06] P. Capuzzi, P. Vignolo, F. Federici, and M. P. Tosi, *Sound propagation in elongated superfluid fermionic clouds*, *Phys. Rev. A* **73**, 021603 (2006).
- [Car02] E. W. Carlson, V. J. Emery, S. A. Kivelson, and D. Orgad, *Concepts in High Temperature Superconductivity*, arXiv:cond-mat/0206217 (2002).
- [Cas97] Y. Castin and J. Dalibard, *Relative phase of two Bose-Einstein condensates*, *Phys. Rev. A* **55**, 4330 (1997).
- [Ced07] L. S. Cederbaum, A. I. Streltsov, Y. B. Band, and O. E. Alon, *Interferences in the Density of Two Bose-Einstein Condensates Consisting of Identical or Different Atoms*, *Phys. Rev. Lett.* **98**, 110405 (2007).
- [Che05] Q. Chen, J. Stajic, S. Tan, and K. Levin, *BCS-BEC Crossover: From High Temperature Superconductors to Ultracold Superfluids*, *Phys. Rep.* **412**, 1 (2005).
- [Che09] Q. Chen and K. Levin, *Momentum Resolved Radio Frequency Spectroscopy in Trapped Fermi Gases*, *Phys. Rev. Lett.* **102**, 190402 (2009).
- [Che10] F. Chevy and C. Mora, *Ultra-cold polarized Fermi gases*, *Rep. Prog. Phys.* **73**, 112401 (2010).
- [Chi00] A. P. Chikkatur, A. Görlitz, D. M. Stamper-Kurn, S. Inouye, S. Gupta, and W. Ketterle, *Suppression and Enhancement of Impurity Scattering in a Bose-Einstein Condensate*, *Phys. Rev. Lett.* **85**, 483 (2000).
- [Chi04] C. Chin, M. Bartenstein, A. Altmeyer, S. Riedl, S. Jochim, J. Hecker Denschlag, and R. Grimm, *Observation of the Pairing Gap in a Strongly Interacting Fermi Gas*, *Science* **305**, 1128 (2004).
- [Chi10] C. Chin, R. Grimm, P. S. Julienne, and E. Tiesinga, *Feshbach resonances in ultracold gases*, *Rev. Mod. Phys.* **82**, 1225 (2010).
- [Cho12] L. Chomaz, L. Corman, T. Yefsah, R. Desbuquois, and J. Dalibard, *Absorption imaging of a quasi-two-dimensional gas: a multiple scattering analysis*, *New J. Phys.* **14**, 055001 (2012).
- [Chu98] S. Chu, *Nobel Lecture: The manipulation of neutral particles*, *Rev. Mod. Phys.* **70**, 685 (1998).
- [Com06] R. Combescot, S. Giorgini, and S. Stringari, *Molecular signatures in the structure factor of an interacting Fermi gas*, *EPL (Europhysics Letters)* **75**, 695 (2006).
- [Cou98] P. Courteille, R. S. Freeland, D. J. Heinzen, F. A. van Abeelen, and B. J. Verhaar, *Observation of a Feshbach Resonance in Cold Atom Scattering*, *Phys. Rev. Lett.* **81**, 69 (1998).

- [Cro09] A. D. Cronin, J. Schmiedmayer, and D. E. Pritchard, *Optics and interferometry with atoms and molecules*, Rev. Mod. Phys. **81**, 1051 (2009).
- [CT98] C. N. Cohen-Tannoudji, *Nobel Lecture: Manipulating atoms with photons*, Rev. Mod. Phys. **70**, 707 (1998).
- [Cub03] J. Cubizolles, T. Bourdel, S. J. J. M. F. Kokkelmans, G. V. Shlyapnikov, and C. Salomon, *Production of Long-Lived Ultracold Li_2 Molecules from a Fermi Gas*, Phys. Rev. Lett. **91**, 240401 (2003).
- [Dal99] F. Dalfovo, S. Giorgini, L. P. Pitaevskii, and S. Stringari, *Theory of Bose-Einstein condensation in trapped gases*, Rev. Mod. Phys. **71**, 463 (1999).
- [Das57] J. G. Dash and R. D. Taylor, *Hydrodynamics of Oscillating Disks in Viscous Fluids: Density and Viscosity of Normal Fluid in Pure He^4 from $1.2^\circ K$ to the Lambda Point*, Phys. Rev. **105**, 7 (1957).
- [Dav27] C. J. Davisson and L. H. Germer, *The scattering of electrons by a single crystal of nickel*, Nature **119**, 558560 (1927).
- [Dav95] K. B. Davis, M. O. Mewes, M. R. Andrews, N. J. van Druten, D. S. Durfee, D. M. Kurn, and W. Ketterle, *Bose-Einstein condensation in a gas of sodium atoms*, Phys. Rev. Lett. **75**, 3969 (1995).
- [DeM99] B. DeMarco and D. S. Jin, *Onset of Fermi Degeneracy in a Trapped Atomic Gas*, Science **285**, 1703 (1999).
- [DeS10] B. J. DeSalvo, M. Yan, P. G. Mickelson, Y. N. Martinez de Escobar, and T. C. Killian, *Degenerate Fermi Gas of ^{87}Sr* , Phys. Rev. Lett. **105**, 030402 (2010).
- [DG66] P. De Gennes, *Superconductivity Of Metals And Alloys*, W.A. Benjamin, Inc., New York - Amsterdam (1966).
- [Don01] E. A. Donley, N. R. Clausen, S. L. Cornish, J. L. Roberts, E. A. Cornell, and C. E. Wieman, *Dynamics of Collapsing and Exploding Bose-Einstein Condensates*, Nature **412**, 295 (2001).
- [DS05] L. De Sarlo, L. Fallani, J. E. Lye, M. Modugno, R. Saers, C. Fort, and M. Inguscio, *Unstable regimes for a Bose-Einstein condensate in an optical lattice*, Phys. Rev. A **72**, 013603 (2005).
- [Est30] I. Estermann and O. Stern, *Beugung von Molekularstrahlen*, Z. Phys. **61**, 95 (1930).
- [Fan61] U. Fano, *Effects of configuration interaction on intensities and phase shifts*, Phys. Rev. **124**, 1866 (1961).
- [Fer08] F. Ferlaino, S. Knoop, M. Mark, M. Berninger, H. Schöbel, H.-C. Nägerl, and R. Grimm, *Collisions between tunable halo dimers: Exploring an elementary four-body process with identical bosons*, Phys. Rev. Lett. **101**, no. 2, 023201 (2008).
- [Fer11] F. Ferlaino, A. Zenesini, M. Berninger, B. Huang, H.-C. Nägerl, and R. Grimm, *Efimov Resonances in Ultracold Quantum Gases*, Few-Body Systems **51**, 113 (2011).

- [Fes58] H. Feshbach, *United theory of nuclear reactions*, Ann. Phys. **5**, 357 (1958).
- [Fes62] H. Feshbach, *United theory of nuclear reactions II*, Ann. Phys. **19**, 287 (1962).
- [Fuk07a] T. Fukuhara, Y. Takasu, M. Kumakura, and Y. Takahashi, *Degenerate Fermi Gases of Ytterbium*, Phys. Rev. Lett. **98**, 030401 (2007).
- [Fuk07b] T. Fukuhara, Y. Takasu, S. Sugawa, and Y. Takahashi, *Quantum Degenerate Fermi Gases of Ytterbium Atoms*, J. Low Temp. Phys. **148**, 441 (2007).
- [Fuk07c] N. Fukushima, Y. Ohashi, E. Taylor, and A. Griffin, *Superfluid density and condensate fraction in the BCS-BEC crossover regime at finite temperatures*, Phys. Rev. A **75**, 033609 (2007).
- [Gae10] J. P. Gaebler, J. T. Stewart, T. E. Drake, D. S. Jin, A. Perali, P. Pieri, and G. C. Strinati, *Observation of pseudogap behaviour in a strongly interacting Fermi gas*, Nature Phys. **6**, 569 (2010).
- [Gal13] V. Galitski and I. B. Spielman, *Spin-orbit coupling in quantum gases*, Nature **494**, 49 (2013).
- [Gar00] C. W. Gardiner, J. Ye, H. C. Nagerl, and H. J. Kimble, *Evaluation of heating effects on atoms trapped in an optical trap*, Phys. Rev. A **61**, 045801 (2000).
- [Geh98] M. E. Gehm, K. M. O'Hara, T. A. Savard, and J. E. Thomas, *Dynamics of noise-induced heating in atom traps*, Phys. Rev. A **58**, 3914 (1998).
- [Ger11] S. Gerlich, S. Eibenberger, M. Tomandl, S. Nimmrichter, K. Hornberger, P. J. Fagan, J. Tüxen, M. Mayor, and M. Arndt, *Quantum interference of large organic molecules*, Nat. Commun. **2**, 263 (2011).
- [Gio08] S. Giorgini, L. P. Pitaevskii, and S. Stringari, *Theory of ultracold atomic Fermi gases*, Rev. Mod. Phys. **80**, 1215 (2008).
- [Gly00] H. R. Glyde, R. T. Azuah, and W. G. Stirling, *Condensate, momentum distribution, and final-state effects in liquid ^4He* , Phys. Rev. B **62**, 14337 (2000).
- [Gou10] O. Goulko and M. Wingate, *Thermodynamics of balanced and slightly spin-imbalanced Fermi gases at unitarity*, Phys. Rev. A **82**, 053621 (2010).
- [Gra02] S. R. Granade, M. E. Gehm, K. M. O'Hara, and J. E. Thomas, *All-Optical Production of a Degenerate Fermi Gas*, Phys. Rev. Lett. **88**, 120405 (2002).
- [Gre03] M. Greiner, C. A. Regal, and D. S. Jin, *Emergence of a Molecular Bose-Einstein Condensate from a Fermi Gas*, Nature **426**, 537 (2003).
- [Gre05] M. Greiner, C. A. Regal, and D. S. Jin, *Probing the Excitation Spectrum of a Fermi Gas in the BCS-BEC Crossover Regime*, Phys. Rev. Lett. **94**, 070403 (2005).
- [Gri88] R. Grimm and J. Mlynek, *Observation of Light-Pressure-Induced Dispersion in Yb Vapor*, Phys. Rev. Lett. **61**, 2308 (1988).

- [Gri97] A. Griffin and E. Zaremba, *First and second sound in a uniform Bose gas*, Phys. Rev. A **56**, 4839 (1997).
- [Gri00] R. Grimm, M. Weidemüller, and Y. B. Ovchinnikov, *Optical dipole traps for neutral atoms*, Adv. At. Mol. Opt. Phys. **42**, 95 (2000).
- [Gup03] S. Gupta, Z. Hadzibabic, M. W. Zwierlein, C. A. Stan, K. Dieckmann, C. H. Schunck, E. G. M. van Kempen, B. J. Verhaar, and W. Ketterle, *Radio-Frequency Spectroscopy of Ultracold Fermions*, Science **300**, 1723 (2003).
- [Had02] Z. Hadzibabic, C. A. Stan, K. Dieckmann, S. Gupta, M. W. Zwierlein, A. Görlitz, and W. Ketterle, *Two-Species Mixture of Quantum Degenerate Bose and Fermi Gases*, Phys. Rev. Lett. **88**, 160401 (2002).
- [Had06] Z. Hadzibabic, P. Krger, M. Cheneau, B. Battelier, and J. Dalibard, *Berezinskii-Kosterlitz-Thouless crossover in a trapped atomic gas*, Nature **441**, 1118 (2006).
- [Hau07] R. Haussmann, W. Rantner, S. Cerrito, and W. Zwerger, *Thermodynamics of the BCS-BEC crossover*, Phys. Rev. A **75**, 023610 (2007).
- [Hau08] R. Haussmann and W. Zwerger, *Thermodynamics of a trapped unitary Fermi gas*, Phys. Rev. A **78**, 063602 (2008).
- [He07] Y. He, Q. Chen, C.-C. Chien, and K. Levin, *First- and second-sound-like modes at finite temperature in trapped Fermi gases from BCS to BEC*, Phys. Rev. A **76**, 051602 (2007).
- [Hei04] H. Heiselberg, *Collective Modes of Trapped Gases at the BEC-BCS Crossover*, Phys. Rev. Lett. **93**, 040402 (2004).
- [Hei06] H. Heiselberg, *Sound modes at the BCS-BEC crossover*, Phys. Rev. A **73**, 013607 (2006).
- [Hem81] P. R. Hemmer, F. Y. Wu, and S. Ezekiel, *Influence of atomic recoil on power broadened lineshapes in 2-level atoms*, Opt. Commun. **38**, 105 (1981).
- [Hen03] G. Hendel, *Atom - Atom Wechselwirkung in einem ultrakalten, fermionischen Gas*, Diploma thesis, University of Innsbruck (2003).
- [Ho04] T.-L. Ho, *Universal Thermodynamics of Degenerate Quantum Gases in the Unitarity Limit*, Phys. Rev. Lett. **92**, 090402 (2004).
- [Ho10] T.-L. Ho and Q. Zhou, *Obtaining the phase diagram and thermodynamic quantities of bulk systems from the densities of trapped gases*, Nature Phys. **6**, 0131 (2010).
- [Hof07] S. Hofferberth, I. Lesanovsky, B. Fischer, T. Schumm, and J. Schmiedmayer, *Non-equilibrium coherence dynamics in one-dimensional Bose gases*, Nature **449**, 324 (2007).
- [Hor10] M. Horikoshi, S. Nakajima, M. Ueda, and T. Mukaiyama, *Measurement of universal thermodynamic functions for a unitary Fermi gas*, Science **327**, 442 (2010).
- [Hou13a] Y.-H. Hou, L. Pitaevskii, and S. Stringari, *Scaling solutions of the two-fluid hydrodynamic equations in a harmonically trapped gas at unitarity*, Phys. Rev. A **87**, 033620 (2013).

- [Hou13b] Y.-H. Hou, L. P. Pitaevskii, and S. Stringari, *First and second sound in a highly elongated Fermi gas at unitarity*, arXiv:1301.4419 (2013).
- [Hu07] H. Hu, P. D. Drummond, and X.-J. Liu, *Universal thermodynamics of strongly interacting Fermi gases*, Nature Phys. **3**, 469 (2007).
- [Hu10] H. Hu, E. Taylor, X.-J. Liu, S. Stringari, and A. Griffin, *Second sound and the density response function in uniform superfluid atomic gases*, New J. Phys. **12**, 043040 (2010).
- [Ing08] M. Inguscio, W. Ketterle, and C. Salomon (Eds.), *Ultra-cold Fermi Gases*, IOS Press, Amsterdam (2008), Proceedings of the International School of Physics “Enrico Fermi”, Course CLXIV, Varenna, 20-30 June 2006.
- [Ino98] S. Inouye, M. R. Andrews, J. Stenger, H.-J. Miesner, D. M. Stamper-Kurn, and W. Ketterle, *Observation of Feshbach resonances in a Bose-Einstein condensate*, Nature **392**, 151 (1998).
- [Ino01] S. Inouye, S. Gupta, T. Rosenband, A. P. Chikkatur, A. Görlitz, T. L. Gustavson, A. E. Leanhardt, D. E. Pritchard, and W. Ketterle, *Observation of Vortex Phase Singularities in Bose-Einstein Condensates*, Phys. Rev. Lett. **87**, 080402 (2001).
- [Joc03a] S. Jochim, M. Bartenstein, A. Altmeyer, G. Hendl, C. Chin, J. Hecker Denschlag, and R. Grimm, *Pure Gas of Optically Trapped Molecules Created from Fermionic Atoms*, Phys. Rev. Lett **91**, 240402 (2003).
- [Joc03b] S. Jochim, M. Bartenstein, A. Altmeyer, G. Hendl, S. Riedl, C. Chin, J. Hecker Denschlag, and R. Grimm, *Bose-Einstein Condensation of Molecules*, Science **302**, 2101 (2003).
- [Joc04] S. Jochim, *Bose-Einstein Condensation of Molecules*, Ph.D. thesis, Innsbruck University (2004).
- [Jos07] J. Joseph, B. Clancy, L. Luo, J. Kinast, A. Turlapov, and J. E. Thomas, *Measurement of Sound Velocity in a Fermi Gas near a Feshbach Resonance*, Phys. Rev. Lett. **98**, 170401 (2007).
- [Jos11] J. A. Joseph, J. E. Thomas, M. Kulkarni, and A. G. Abanov, *Observation of Shock Waves in a Strongly Interacting Fermi Gas*, Phys. Rev. Lett. **106**, 150401 (2011).
- [Kap38] P. Kapitza, *Viscosity of liquid helium below the λ -point*, Nature **141**, 74 (1938).
- [Kha65] I. M. Khalatnikov, *An Introduction to the Theory of Superfluidity*, Benjamin, New York (1965).
- [Kin04a] J. Kinast, S. L. Hemmer, M. E. Gehm, A. Turlapov, and J. E. Thomas, *Evidence for Superfluidity in a Resonantly Interacting Fermi Gas*, Phys. Rev. Lett. **92**, 150402 (2004).
- [Kin04b] J. Kinast, A. Turlapov, and J. E. Thomas, *Breakdown of Hydrodynamics in the Radial Breathing Mode of a Strongly Interacting Fermi Gas*, Phys. Rev. A **70**, 051401(R) (2004).
- [Kin05a] J. Kinast, A. Turlapov, and J. E. Thomas, *Damping of a Unitary Fermi Gas*, Phys. Rev. Lett. **94**, 170404 (2005).

- [Kin05b] J. Kinast, A. Turlapov, J. E. Thomas, Q. Chen, J. Stajic, and K. Levin, *Heat Capacity of a Strongly Interacting Fermi Gas*, *Science* **307**, 1296 (2005).
- [Köh06] T. Köhler, K. Goral, and P. S. Julienne, *Production of cold molecules via magnetically tunable Feshbach resonances*, *Rev. Mod. Phys.* **78**, 1131 (2006).
- [Koh07] C. Kohstall, *A New Toolbox for Experiments with Ultracold ^6Li* , Diploma thesis, University of Innsbruck (2007).
- [Ku12] M. J. H. Ku, A. T. Sommer, L. W. Cheuk, and M. W. Zwierlein, *Revealing the Superfluid Lambda Transition in the Universal Thermodynamics of a Unitary Fermi Gas*, *Science* **335**, 563 (2012).
- [Kuh11] E. D. Kuhnle, S. Hoinka, H. Hu, P. Dyke, P. Hannaford, and C. J. Vale, *Studies of the universal contact in a strongly interacting Fermi gas using Bragg spectroscopy*, *New J. Phys.* **13**, 055010 (2011).
- [Lan41] L. Landau, *The theory of superfluidity of helium II*, *J. Phys. (Moscow)* **5**, 71 (1941).
- [Lan47] L. Landau, *On the theory of superfluidity of helium II*, *J. Phys. (Moscow)* **11**, 91 (1947).
- [Lan77] L. D. Landau and E. M. Lifshitz, *Quantum Mechanics, vol. 3 (Course of theoretical physics)*, Butterworth-Heinemann, Oxford (1977).
- [Lan80a] L. D. Landau and E. M. Lifshitz, *Statistical physics part 1, vol. 5 (Course of theoretical physics)*, Pergamon Press, Oxford (1980).
- [Lan80b] L. D. Landau and E. M. Lifshitz, *Statistical physics part 2, vol. 9 (Course of theoretical physics)*, Pergamon Press, Oxford (1980).
- [Lan93] L. D. Landau and E. M. Lifshitz, *Mechanics, vol. 1 (Course of theoretical physics)*, Butterworth-Heinemann, Oxford (1993).
- [Lee57] T. D. Lee, K. Huang, and C. N. Yang, *Eigenvalues and Eigenfunctions of a Bose System of Hard Spheres and its Low-Temperature Properties*, *Phys. Rev.* **106**, 1135 (1957).
- [Leg80] A. J. Leggett, in A. Pekalski and R. Przystawa (Eds.), *Modern Trends in the Theory of Condensed Matter*, volume 115 of *Lecture Notes in Physics*, 13, Springer Verlag, Berlin (1980).
- [Leg06] A. J. Leggett, *What do we know about high T_c ?*, *Nature Phys.* **2**, 134 (2006).
- [Let77] V. Letokhov and V. Chebotaev, *Nonlinear laser spectroscopy*, Springer series in optical sciences, Springer-Verlag (1977).
- [Liu09] X.-J. Liu, H. Hu, and P. D. Drummond, *Virial expansion for a strongly correlated Fermi gas*, *Phys. Rev. Lett.* **102**, 160401 (2009).
- [Lu12] M. Lu, N. Q. Burdick, and B. L. Lev, *Quantum Degenerate Dipolar Fermi Gas*, *Phys. Rev. Lett.* **108**, 215301 (2012).
- [Luo07] L. Luo, B. Clancy, J. Joseph, J. Kinast, and J. E. Thomas, *Measurement of the Entropy and Critical Temperature of a Strongly Interacting Fermi Gas*, *Phys. Rev. Lett.* **98**, 080402 (2007).

- [Mar88] A. G. Martin, K. Helmerson, V. S. Bagnato, G. P. Lafyatis, and D. E. Pritchard, *rf Spectroscopy of Trapped Neutral Atoms*, Phys. Rev. Lett. **61**, 2431 (1988).
- [McN06] J. M. McNamara, T. Jelten, A. S. Tychkov, W. Hogervorst, and W. Vassen, *Degenerate Bose-Fermi Mixture of Metastable Atoms*, Phys. Rev. Lett. **97**, 080404 (2006).
- [Men02] C. Menotti, P. Pedri, and S. Stringari, *Expansion of an Interacting Fermi Gas*, Phys. Rev. Lett. **89**, 250402 (2002).
- [Mep09a] R. Meppelink, S. B. Koller, and P. van der Straten, *Sound propagation in a Bose-Einstein condensate at finite temperatures*, Phys. Rev. A **109**, 043605 (2009).
- [Mep09b] R. Meppelink, S. B. Koller, J. M. Vogels, H. T. C. Stoof, and P. van der Straten, *Damping of Superfluid Flow by a Thermal Cloud*, Phys. Rev. Lett. **103**, 265301 (2009).
- [Met99] H. J. Metcalf and P. van der Straten, *Laser Cooling and Trapping*, Springer, New York (1999).
- [Mil05] D. E. Miller, J. R. Anglin, J. R. Abo-Shaeer, K. Xu, J. K. Chin, and W. Ketterle, *High-contrast interference in a thermal cloud of atoms*, Phys. Rev. A **71**, 043615 (2005).
- [Mil07] D. E. Miller, J. K. Chin, C. A. Stan, Y. Liu, W. Setiawan, C. Sanner, and W. Ketterle, *Critical Velocity for Superfluid Flow across the BEC-BCS Crossover*, Phys. Rev. Lett. **99**, 070402 (2007).
- [Mos01] A. Mosk, S. Jochim, T. Elsässer, M. Weidemüller, and R. Grimm, *Resonator-Enhanced Optical Dipole Trap for Fermionic Lithium Atoms*, Optics Lett. **26**, 1837 (2001).
- [Nas09] S. Nascimbène, N. Navon, K. J. Jiang, L. Tarruell, M. Teichmann, J. McKeever, F. Chevy, and C. Salomon, *Collective Oscillations of an Imbalanced Fermi Gas: Axial Compression Modes and Polaron Effective Mass*, Phys. Rev. Lett. **103**, 170402 (2009).
- [Nas10] S. Nascimbène, N. Navon, K. J. Jiang, F. Chevy, and C. Salomon, *Exploring the thermodynamics of a universal Fermi gas*, Nature **463**, 1057 (2010).
- [Nav10] N. Navon, S. Nascimbène, F. Chevy, and C. Salomon, *The Equation of State of a Low-Temperature Fermi Gas with Tunable Interactions*, Science **328**, 729 (2010).
- [Noz85] P. Nozières and S. Schmitt-Rink, *Bose condensation in an attractive fermion gas: From weak to strong coupling superconductivity*, J. Low Temp. Phys. **59**, 195 (1985).
- [O'H02a] K. M. O'Hara, S. L. Hemmer, M. E. Gehm, S. R. Granade, and J. E. Thomas, *Observation of a Strongly Interacting Degenerate Fermi Gas*, Science **298**, 2179 (2002).
- [O'H02b] K. M. O'Hara, S. L. Hemmer, S. R. Granade, M. E. Gehm, J. E. Thomas, V. Venturi, E. Tiesinga, and C. J. Williams, *Measurement of the zero crossing in a Feshbach resonance of fermionic 6Li* , Phys. Rev. A **66**, 041401 (2002).
- [Ott08] T. B. Ottenstein, T. Lompe, M. Kohnen, A. N. Wenz, and S. Jochim, *Collisional stability of a three-component degenerate Fermi gas*, Phys. Rev. Lett. **101**, 203202 (2008).
- [Par05] G. B. Partridge, K. E. Strecker, R. I. Kamar, M. W. Jack, and R. G. Hulet, *Molecular Probe of Pairing in the BEC-BCS Crossover*, Phys. Rev. Lett. **95**, 020404 (2005).

- [Par06] G. B. Partridge, W. Li, R. I. Kamar, Y. Liao, and R. G. Hulet, *Pairing and Phase Separation in a Polarized Fermi Gas*, Science **311**, 503 (2006).
- [Per04] A. Perali, P. Pieri, L. Pisani, and G. C. Strinati, *BCS-BEC Crossover at Finite Temperature for Superfluid Trapped Fermi Atoms*, Phys. Rev. Lett. **92**, 220404 (2004).
- [Pes44] V. P. Peshkov, “*Second sound*” in *helium II*, J. Phys. (Moscow) **8**, 381 (1944).
- [Pet02] C. J. Pethick and H. Smith, *Bose-Einstein condensation in dilute gases*, Cambridge University Press, Cambridge (2002).
- [Pet04] D. S. Petrov, C. Salomon, and G. V. Shlyapnikov, *Weakly Bound Dimers of Fermionic Atoms*, Phys. Rev. Lett. **93**, 090404 (2004).
- [Pet05a] D. S. Petrov, C. Salomon, and G. V. Shlyapnikov, *Diatom molecules in ultracold Fermi gases—novel composite bosons*, J. Phys. B: At. Mol. Opt. Phys. **38**, S645 (2005).
- [Pet05b] D. S. Petrov, C. Salomon, and G. V. Shlyapnikov, *Scattering properties of weakly bound dimers of fermionic atoms*, Phys. Rev. A **71**, 012708 (2005).
- [Phi98] W. D. Phillips, *Nobel Lecture: Laser cooling and trapping of neutral atoms*, Rev. Mod. Phys. **70**, 721 (1998).
- [Pin66] D. Pines and P. Nozières, *The Theory of Quantum Liquids, vol 1*, Benjamin, New York (1966).
- [Pit03] L. Pitaevskii and S. Stringari, *Bose-Einstein condensation*, Oxford University Press, Oxford (2003).
- [Rad10] L. Radzihovsky and D. E. Sheehy, *Imbalanced Feshbach-resonant Fermi gases*, Rep. Prog. Phys. **73**, 076501 (2010).
- [Reg03a] C. A. Regal and D. S. Jin, *Measurement of Positive and Negative Scattering Lengths in a Fermi Gas of Atoms*, Phys. Rev. Lett. **90**, 230404 (2003).
- [Reg03b] C. A. Regal, C. Ticknor, J. L. Bohn, and D. S. Jin, *Creation of Ultracold Molecules from a Fermi Gas of Atoms*, Nature **424**, 47 (2003).
- [Reg04] C. A. Regal, M. Greiner, and D. S. Jin, *Observation of Resonance Condensation of Fermionic Atom Pairs*, Phys. Rev. Lett. **92**, 040403 (2004).
- [Rem12] B. S. Rem, A. T. Grier, I. Ferrier-Barbut, U. Eismann, T. Langen, N. Navon, L. Khaykovich, F. Werner, D. S. Petrov, F. Chevy, and C. Salomon, *Lifetime of the Bose Gas with Resonant Interactions*, arXiv:1212.5274 (2012).
- [Rie04] S. Riedl, *Untersuchung stark wechselwirkender fermionischer Quantengase mittels Absorptionsabbildung*, Diploma thesis, University of Innsbruck (2004).
- [Rie08] S. Riedl, E. R. Sánchez Guajardo, C. Kohstall, A. Altmeyer, M. J. Wright, J. Hecker Denschlag, R. Grimm, G. M. Bruun, and H. Smith, *Collective oscillations of a Fermi gas in the unitarity limit: Temperature effects and the role of pair correlations*, Phys. Rev. A **78**, 053609 (2008).

- [Rie09] S. Riedl, E. R. Sánchez Guajardo, C. Kohstall, J. Hecker Denschlag, and R. Grimm, *Lifetime of angular momentum in a rotating strongly interacting Fermi gas*, Phys. Rev. A **79**, 053628 (2009).
- [Rie11] S. Riedl, E. R. Sánchez Guajardo, C. Kohstall, J. H. Denschlag, and R. Grimm, *Superfluid quenching of the moment of inertia in a strongly interacting Fermi gas*, New J. Phys. **13**, 035003 (2011).
- [Roa02] G. Roati, F. Riboli, G. Modugno, and M. Inguscio, *Fermi-Bose Quantum Degenerate K-Rb Mixture with Attractive Interaction*, Phys. Rev. Lett. **89**, 150403 (2002).
- [Sal10] L. Salasnich, *Low-temperature thermodynamics of the unitary Fermi gas: Superfluid fraction, first sound, and second sound*, Phys. Rev. A **82**, 063619 (2010).
- [Sav97] T. A. Savard, K. M. O'Hara, and J. E. Thomas, *Laser-noise-induced heating in far-off resonance optical traps*, Phys. Rev. A **56**, R1095 (1997).
- [Sch94] W. Schöllkopf and J. P. Toennies, *Nondestructive Mass Selection of Small van der Waals Clusters*, Science **266**, 1345 (1994).
- [Sch01] F. Schreck, L. Khaykovich, K. L. Corwin, G. Ferrari, T. Bourdel, J. Cubizolles, and C. Salomon, *Quasipure Bose-Einstein Condensate Immersed in a Fermi Sea*, Phys. Rev. Lett. **87**, 080403 (2001).
- [Sch05] C. H. Schunck, M. W. Zwierlein, C. A. Stan, S. M. F. Raupach, W. Ketterle, A. Simoni, E. Tiesinga, C. J. Williams, and P. S. Julienne, *Feshbach Resonances in Fermionic ^6Li* , Phys. Rev. A **71**, 045601 (2005).
- [Sch07] C. H. Schunck, M. W. Zwierlein, A. Schirotzek, and W. Ketterle, *Superfluid Expansion of a Rotating Fermi Gas*, Phys. Rev. Lett. **98**, 050404 (2007).
- [Sch08] C. H. Schunck, Y.-i. Shin, A. Schirotzek, and W. Ketterle, *Determination of the fermion pair size in a resonantly interacting superfluid*, Nature **454**, 739 (2008).
- [Sch09] T. Schäfer and D. Teaney, *Nearly perfect fluidity: from cold atomic gases to hot quark gluon plasmas*, Rep. Prog. Phys. **72**, 126001 (2009).
- [Ser11] F. Serwane, G. Zürn, T. Lompe, T. B. Ottenstein, A. N. Wenz, and S. Jochim, *Deterministic Preparation of a Tunable Few-Fermion System*, Science **332**, 336 (2011).
- [SG11] E. R. Sánchez Guajardo, *Finite temperature dynamics of a degenerate Fermi gas with unitarity limited interactions*, Ph.D. thesis, University of Innsbruck (2011).
- [SG13] E. R. Sanchez Guajardo, M. K. Tey, L. A. Sidorenkov, and R. Grimm, *Higher-nodal collective modes in a resonantly interacting Fermi gas*, arXiv:1304.5118 (2013).
- [Shi04] Y. Shin, M. Saba, T. A. Pasquini, W. Ketterle, D. E. Pritchard, and A. E. Leanhardt, *Atom Interferometry with Bose-Einstein Condensates in a Double-Well Potential*, Phys. Rev. Lett. **92**, 050405 (2004).
- [Shi07] Y. Shin, C. H. Schunck, A. Schirotzek, and W. Ketterle, *Tomographic rf Spectroscopy of a Trapped Fermi Gas at Unitarity*, Phys. Rev. Lett. **99**, 090403 (2007).

- [Sid13] L. A. Sidorenkov, M. K. Tey, R. Grimm, Y.-H. Hou, L. Pitaevskii, and S. Stringari, *Second sound and the superfluid fraction in a Fermi gas with resonant interactions*, Nature **xxx**, xx (2013).
- [Sil05] C. Silber, S. Gunther, C. Marzok, B. Deh, P. W. Courteille, and C. Zimmermann, *Quantum-Degenerate Mixture of Fermionic Lithium and Bosonic Rubidium Gases*, Phys. Rev. Lett. **95**, 170408 (2005).
- [Sim00] J. E. Simsarian, J. Denschlag, M. Edwards, C. W. Clark, L. Deng, E. W. Hagley, K. Helmerson, S. L. Rolston, and W. D. Phillips, *Imaging the Phase of an Evolving Bose-Einstein Condensate Wave Function*, Phys. Rev. Lett. **85**, 2040 (2000).
- [SK98] D. M. Stamper-Kurn, H.-J. Miesner, S. Inouye, M. R. Andrews, and W. Ketterle, *Collisionless and Hydrodynamic Excitations of a Bose-Einstein Condensate*, Phys. Rev. Lett. **81**, 500 (1998).
- [Som11] A. Sommer, M. Ku, G. Roati, and M. W. Zwierlein, *Universal spin transport in a strongly interacting Fermi gas*, Nature **472**, 201 (2011).
- [Sta12] D. Stadler, S. Krinner, J. Meineke, J.-P. Brantut, and T. Esslinger, *Observing the drop of resistance in the flow of a superfluid Fermi gas*, Nature **491**, 736 (2012).
- [Ste08] J. T. Stewart, J. P. Gaebler, and D. S. Jin, *Using photoemission spectroscopy to probe a strongly interacting Fermi gas*, Nature **454**, 744 (2008).
- [Tan08a] S. Tan, *Energetics of a strongly correlated Fermi gas*, Annals of Physics **323**, 2952 (2008).
- [Tan08b] S. Tan, *Generalized virial theorem and pressure relation for a strongly correlated Fermi gas*, Annals of Physics **323**, 2987 (2008).
- [Tan08c] S. Tan, *Large momentum part of a strongly correlated Fermi gas*, Annals of Physics **323**, 2971 (2008).
- [Tay07] E. Taylor, H. Hu, X.-J. Liu, and A. Griffin, *Probing two-fluid hydrodynamics in a trapped Fermi superfluid at unitarity*, arXiv:0709.0698 (2007).
- [Tay08] E. Taylor, H. Hu, X.-J. Liu, and A. Griffin, *Variational theory of two-fluid hydrodynamic modes at unitarity*, Phys. Rev. A **77**, 033608 (2008).
- [Tay09] E. Taylor, H. Hu, X.-J. Liu, L. P. Pitaevskii, A. Griffin, and S. Stringari, *First and second sound in a strongly interacting Fermi gas*, Phys. Rev. A **80**, 053601 (2009).
- [Tey10] M. K. Tey, S. Stellmer, R. Grimm, and F. Schreck, *Double-degenerate Bose-Fermi mixture of strontium*, Phys. Rev. A **82**, 011608 (2010).
- [Tey13] M. K. Tey, L. A. Sidorenkov, E. R. Sánchez Guajardo, R. Grimm, M. J. H. Ku, M. W. Zwierlein, Y.-H. Hou, L. Pitaevskii, and S. Stringari, *Collective Modes in a Unitary Fermi Gas across the Superfluid Phase Transition*, Phys. Rev. Lett. **110**, 055303 (2013).
- [Tho05] J. E. Thomas, J. Kinast, and A. Turlapov, *Virial Theorem and Universality in a Unitary Fermi Gas*, Phys. Rev. Lett. **95**, 120402 (2005).
- [Tin75] M. Tinkham, *Introduction to superconductivity*, McGraw-Hill, New York (1975).

- [Tis38] L. Tisza, *Transport phenomena in helium II*, Nature **141**, 913 (1938).
- [Tru01] A. G. Truscott, K. E. Strecker, W. I. McAlexander, G. B. Partridge, and R. G. Hulet, *Observation of Fermi Pressure in a Gas of Trapped Atoms*, Science **291**, 2570 (2001).
- [Tsu10] S. Tsuchiya, R. Watanabe, and Y. Ohashi, *Pseudogap in Fermionic Density of States in the BCS-BEC Crossover of Atomic Fermi Gases*, J. Low Temp. Phys. **158**, 29 (2010).
- [Vee08] G. Veeravalli, E. Kuhnle, P. Dyke, and C. J. Vale, *Bragg Spectroscopy of a Strongly Interacting Fermi Gas*, Phys. Rev. Lett. **101**, 250403 (2008).
- [Wal08] J. Walraven, *Elements of Quantum Gases: Thermodynamic and Collisional Properties of Trapped Atomic Gases (Les Houches lectures and more, 2008)*, available online at: <http://www.phlam.univ-lille1.fr/leshouches/cours08/walraven.pdf> (2008).
- [Web03] T. Weber, J. Herbig, M. Mark, H.-C. Nägerl, and R. Grimm, *Three-body recombination at large scattering lengths in an ultracold atomic gas*, Phys. Rev. Lett. **91**, 123201 (2003).
- [Wri07] M. J. Wright, S. Riedl, A. Altmeyer, C. Kohstall, E. R. Sánchez Guajardo, J. Hecker Denschlag, and R. Grimm, *Finite-temperature collective dynamics of a Fermi gas in the BEC-BCS crossover*, Phys. Rev. Lett. **99**, 150403 (2007).
- [Xio06] H. Xiong, S. Liu, and M. Zhan, *Interaction-induced interference for two independent Bose-Einstein condensates*, New J. Phys. **8**, 245 (2006).
- [Xu03] K. Xu, T. Mukaiyama, J. R. Abo-Shaeer, J. K. Chin, D. E. Miller, and W. Ketterle, *Formation of Quantum-Degenerate Sodium Molecules*, Phys. Rev. Lett. **91**, 210402 (2003).
- [Yef13] T. Yefsah, A. T. Sommer, M. J. H. Ku, L. W. Cheuk, W. Ji, W. S. Bakr, and M. W. Zwierlein, *Heavy Solitons in a Fermionic Superfluid*, arXiv:1302.4736 (2013).
- [Zaw10] M. E. Zawadzki, P. F. Griffin, E. Riis, and A. S. Arnold, *Spatial interference from well-separated split condensates*, Phys. Rev. A **81**, 043608 (2010).
- [Zha07] W. Zhang and C. A. R. Sá de Melo, *Matter-wave interference in s -wave and p -wave Fermi condensates*, Phys. Rev. A **76**, 013627 (2007).
- [Zür13] G. Zürn, T. Lompe, A. N. Wenz, S. Jochim, P. S. Julienne, and J. M. Hutson, *Precise Characterization of ^6Li Feshbach Resonances Using Trap-Sideband-Resolved RF Spectroscopy of Weakly Bound Molecules*, Phys. Rev. Lett. **110**, 135301 (2013).
- [Zwi03] M. W. Zwierlein, C. A. Stan, C. H. Schunck, S. M. F. Raupach, S. Gupta, Z. Hadzibabic, and W. Ketterle, *Observation of Bose-Einstein Condensation of Molecules*, Phys. Rev. Lett. **91**, 250401 (2003).
- [Zwi04] M. W. Zwierlein, C. A. Stan, C. H. Schunck, S. M. F. Raupach, A. J. Kerman, and W. Ketterle, *Condensation of Pairs of Fermionic Atoms near a Feshbach Resonance*, Phys. Rev. Lett. **92**, 120403 (2004).
- [Zwi05] M. W. Zwierlein, J. R. Abo-Shaeer, A. Schirotzek, C. H. Schunck, and W. Ketterle, *Vortices and Superfluidity in a Strongly Interacting Fermi Gas*, Nature **435**, 1047 (2005).

- [Zwi06a] M. W. Zwierlein, A. Schirotzek, C. H. Schunck, and W. Ketterle, *Direct observation of the superfluid phase transition in ultracold Fermi gases*, *Nature* **442**, 54 (2006).
- [Zwi06b] M. W. Zwierlein, A. Schirotzek, C. H. Schunck, and W. Ketterle, *Fermionic Superfluidity with Imbalanced Spin Populations*, *Science* **311**, 492 (2006).

Acknowledgments

After my four years in Innsbruck I came now to a point of defending the PhD-thesis with mixed feelings: the happiness for achievement, and the slight regret which many of us feel at the end of important life period. But one thing is for sure: I am inspired, and it would be hardly possible without a unique working atmosphere, for which I express my warm thanks to the whole ‘ultracold’ group. It is wonderful to be the part of this interacting many-body system and experience the friendly and motivating mean field.

I would like to specially thank my supervisor Rudi Grimm for providing excellent opportunities for research and for his generous support. Without his prime interest in physics, his knowledge and physics intuition, we would not achieve the results presented in this thesis. Although sometimes overloaded with teaching, Rudi was still open for discussions and gave a quick feedback on the things happening in the lab. His guidance and inspiration were essential for me from both scientific and personal side. Spasibo, Rudi!

I also want to thank Johannes Hecker Denschlag, who was a co-PI on Lithium project when I joined the group, for scientific discussions and support.

Florian Schreck gave us a hand in experiment during the critical times when we mostly lacked the experience. This saved us a lot of time for future experiments. Thank you, Florian.

I would like to thank the people with whom I have worked on Lithium project: Stefan Riedl, Christoph Kohstall, Edmundo Sánchez, and Meng Khoon Tey. When I officially joined the Lithium team in April 2009 after an internship period, Stefan was already about to start writing his PhD-thesis. Therefore we did not overlap frequently in the lab, but I was still benefiting from his knowledge during the project-meeting discussions. Christoph patiently introduced me into the basics of Lithium-machine, and shared his knowledge of optics, electronics and programming. Later I have learned a lot from Edmundo during the difficult period when we had to repair or replace most of the electronic equipment in order to reach the stable operation of the experimental setup, and fight with the water leaks. I also acknowledge his excitement about the whole ‘second sound’ topic. Although at that time measurements on second sound did not seem very realistic, part of this excitement was eventually transmitted to me and later made me think more in this direction. In the summer 2010 Meng Khoon joined our lab as a postdoc. His experience and team-building skills significantly raised the productivity of our work and already in the spring 2011 we had the first results on higher-nodal collective oscillations. Meng Khoon has taught me many experimental tricks, frequently coming up with a simple and clever solutions to the problems. But maybe the most important thing I (hopefully) learned from him - is the way to compromise between the perfection and final result in doing experimental physics, as well as in life. I would wish to virtually shake his hand for this mentoring, which should not have been easy.

I would like to express my many thanks to our friends from Trento: Yan-Hua Hou, Lev Pitaevskii and Sandro Stringari for a long-term theoretical support of our experiment and their inexhaustible enthusiasm. It was a great pleasure for me to work with them and I wish them all the best for

their future research.

Also many people from the other projects were always available for discussions and readily shared their experience. Among them, I want to particularly thank Andreas Trenkwalder, Martin Berninger and Kiyotaka Aikawa.

I wish to thank my former roommate Bo (Boris) Huang, for many fruitful physics discussions, beers, hiking tours and friendship. We went together through the first Gender lectures in the Innrain University building - this cannot be forgotten.

A research in experimental physics is not possible without a good electronics. I thank Arthur Wander, Michael Hofer, Wolfgang Kratz, and Gerhard Hendl for their great support.

I also wish to acknowledge our University workshop team: Helmut Jordan, Anton Schönherr, Armin Sailer - they always have the proper tools, good hands and smart ideas for any construction.

It is a requirement for an efficient work to keep the level of disorder below some critical value. For this I want to thank our secretaries: Nicole Jorda, Elisabeth Huck, Doris Corona, and in particular Christine Götsch-Obmascher. They are fast and extremely efficient in solving administrative questions, and very helpful and friendly with personal issues.

I would like to thank those people, without whom I would not start my PhD-study in physics, and maybe not even start doing physics. My school physics teacher Yurii A. Chigrin was the one to awake my interest in fundamental knowledge, and my diploma thesis supervisor Vladimir L. Velichansky has demonstrated that approaching the fundamental physics in experiment is really fascinating. However, the most convincing argument for doing physics is always in front of me - my father, who has a physics education. His ability of holding strong onto his principles, being honest, and precisely catching the essence of things has so much in common with physics!

When doing a PhD it is important not only to finish, but also to finish in a good condition. I thank my friends back home and my flatmates here in Innsbruck for working on that by keeping me balanced between the science and the rest of life. Finally, I thank my whole family for being a source of continuous support during this time, in particular my parents and my wife Olga. Thank you for your love and trust in me.